Non-Empirical Tuning in DFT: Improvements for Modeling Charge Transport Parameters in Organic Semiconductors

A Dissertation Presented to the Academic Faculty

By

Christopher A. Sutton

In Partial Fulfillment of the Requirements for the Degree Doctor of Philosophy in the School of Chemistry and Biochemistry

Georgia Institute of Technology July 2014

Non-Empirical Tuning in DFT: Improvements for Modeling Charge Transport Parameters in Organic Semiconductors

***Approved by**:*

Professor Jean-Luc Brédas (Advisor)

Division of Physical Sciences and Engineering
King Abdullah University of Science and Technology

Professor C. David Sherrill

School of Chemistry and Biochemistry
Georgia Institute of Technology

Professor Seth Marder

School of Chemistry and Biochemistry
Georgia Institute of Technology

Professor Joseph Perry

School of Chemistry and Biochemistry
Georgia Institute of Technology

Professor Elsa Reichmanis

School of Chemical and Biomolecular Engineering
School of Chemistry and Biochemistry
Georgia Institute of Technology

Date Approved: July 31, 2014

Acknowledgements

To my advisor, Jean-Luc Brédas for the guidance and mentorship throughout the past five years. I appreciate the patience and encouragement that you showed when my research got off to a slow start and the rewarding of my efforts with opportunities to present my work at conferences.

I would also like to thank the research scientists, postdocs, and students of the Brédas group. In particular I want to thank Dr. Veaceslav Coropceanu, Dr. Rajesh Naga Tummala, Dr. Travis Kemper, soon-to-be Dr. Alexandr Fonari, Prof. Thodoris Papadopoulos, Dr. Lucas Viani, Dr. Michael Marshall, Prof. Chad Risko, Prof. Thomas Körzdörfer, and Dr. John Sears for all teaching me and helping me along the way. I have learned so much from you all, not just in hard skills, but also in how to approach problems.

I would also like to thank the professors of the University of Central Arkansas who gave me a strong base in chemistry that has helped me every step of the way in constructing this dissertation. Especially, Professor Patrick Desrochers and Micah Abrams, my undergraduate research advisors for allowing me to work in your labs and the subsequent years of support and advice. I also appreciate the invitation to return and share the results of my research with the faculty and students. To my friend, fellow UCA and GT graduate, Dr. Ariel Marshall for all of the support, guidance, and encouragement and for being a great sounding board since our time researching at UCA during the summer of 2005.

My deepest appreciation for the loving support of my family and friends both within Georgia Tech and outside of it, without whom I would certainly not have been able to work

towards my goal. To my grandmother, Lorraine, and grandfather, George, for always encouraging me to learn more. To my dad and mom, Mat and Terri, for being loving parents and for providing an environment that allowed me to be able to pursue my goals. To my brothers, Mat Jr., James, and Phillip for all of their support. To Frank and Joanne, for always creating a home for Allison and I to visit and for being a mentor to a teenage kid with an attitude. To my loving wife, Allison for helping me in everyway possible for these past five years that have been difficult at times (but not as hard as that year in the Americorps).

Table of Contents

List of Tables

List of Figures

Summary

This dissertation is focused on modeling charge-transport in π-conjugated organic materials, which can serve as the active materials in light-weight, flexible, organic photovoltaic cells, offering the potential for cheap, ubiquitous renewable energy. In particular, we used computational chemistry to gain insight into the fundamental processes of charge transport within organic semiconductors to derive an understanding of chemical and physical phenomena that can not be explained through experiment alone in order to further the performance of organic-based electronic devices.

In order to accurately model the organic materials, a combined quantum-mechanical and classical approach is needed, with the ground and excited state electronic properties of isolated organic materials determined using DFT/TD-DFT as a first step and coupled with molecular dynamics and mechanics. This allows for an understanding of the molecular order and packing within nanoscale structures as well as the impact of the intermolecular interactions. However, standard DFT methods suffer from intrinsic errors resulting from approximations to the exchange-correlation potential that can be corrected using a simple non-empirically tuning procedure. This non-empirically tuned long-range corrected density functional method is used to characterize the torsion potentials, indicative of the length of wave function delocalization, in two prototypical π-conjugated polymers, polyacetylene and polydiacetylene, as a function of

chain lengths. This approach is also used to study the charge (de)localization in organic mixed valence complexes and in crystalline acene systems.

DFT-calculated intermolecular electronic couplings (transfer integrals) and band gaps, bandwidths, and effective masses in organic semiconductors are also investigated to give insight into the impact that the choice of functional has on the value of these parameters that are important in the context of charge transport. Of particular importance in organic systems, where the intramolecular interactions are weak van deer Waals, a direct connection between intermolecular electronic coupling (required to be large for efficient charge-carrier transport) and the repulsive exchange-repulsion non-covalent energy is found.

Chapter 1 Introduction

1.1. Overview

Materials derived from organic π-conjugated molecules and polymers have generated extensive research and development efforts because they provide many unique characteristics that are ideal for use as the active layer in a variety of electronic applications such as organic light-emitting diodes (OLEDs) for large-area displays, organic field-effect transistors (OFETs), and organic photovoltaics (OPVs). The principal motivation for the major research currently devoted to organic semiconductor materials is the prospect that these devices can be manufactured at a lower cost than their inorganic counterparts through cheaper processing methods – such as roll-to-roll manufacturing involving solution processing at low temperatures – that allow for scalability. Organic materials can also be readily modified chemically to optimize performance with well-defined electronic, redox, optical, and mechanical properties. To date, OLED displays have delivered the most significant commercial impact, with applications including digital cameras, smartphones, tablets, and televisions that employ electroluminescent organic small molecules and polymers. While OLED-based display products are already established on the market, the future is bright for OPVs with the power conversion efficiency of light into electricity now at 12% by Heliatek GmbH – however, still below the efficiencies measured in the current inorganic-based devices (40%[1]).

Irrespective of application (e.g., OLED, OFET, OPV), the intrinsic efficiency of the active layer is dependent on the ability of the organic material to transport charges, whether they are holes (positive charges) or electrons (negative charges). The mobility –given in terms of the average charge-carrier drift velocity in the presence of an electric field in units of $cm^2V^{-1}s^{-1}$ – is intimately connected to both molecular and material factors such as chemical composition, molecular architecture, purity, and solid-state packing.

For organic molecules, the molecular packing in the crystal depends on both chemical structure and growth conditions. Because the intermolecular interactions in organic crystals are weak (van der Waals forces), the packing is susceptible to external factors;[2-4] this can lead to random small molecular shifts along different directions, or sometimes even to different crystalline packing motifs (polymorphism).[5-7] In fact, numerous examples exist for organic systems that exhibit two polymorphs, which differ slightly in molecular packing and electronic properties.[7,8,9] Indeed, a recent example of this aspect in material design was demonstrated by Bao and co-workers, where the addition of an external physical perturbation through so-called solution shearing resulted in the discovery of new polymorphs of 6,13-bis(triisopropylsilylethynyl) pentacene (TIPS-pentacene) – some materials displayed enhanced performance with high mobilities of 8 – 11 $cm^2 V^{-1} s^{-1}$.[10,11] This technique has a lot of promise as a breakthrough in large-area organic electronic printing because it allows for patterned and aligned single-crystalline films.

TIPs-pentacene also illustrates another significant aspect of organic electronics: Chemical modifications at the molecular level have been employed in the search for new molecules with advantageous properties such as processability,[12] but at the same time, minor modifications can

have a dramatic effect on the crystal structure.[13] For example, the functionalization of pentacene by TIPS groups (TIPS-pentacene) converts the herringbone crystalline structure of pentacene to lamellar.[14,15]

It should be noted that although single-crystal devices have substantially increased mobilities, the integration of single crystals into devices has currently limited industrial application of these materials; for high-throughput device manufacturing and scalable processing needed for the development of printed electronics, reliable solution processing of organic semiconductors at room temperature is crucial. Progress is being made to consistently and reliably grow crystals;[16,17] for example, recent work on stamped crystals used in organic-field effect transistors resulted in high mobilities.[18] Several processing techniques have been significantly improved, such as inkjet printing of single-crystalline 2,7-dioctyl[1]benzothieno[3,2-b][1]benzothiophene (C_8-BTBT) in high yield,[19] as well as several other examples of solution deposition techniques developed to align crystalline domains in polycrystalline films.[20-26]

Beyond small-molecule based devices, polymers are also employed as the active material in many organic devices. In fact, the field of organic electronics dates back to the ground-breaking work of Alan Heeger, Hideki Shirakawa, Alan MacDiarmid, and co-workers in the synthesis and electrical characterization of the first doped conductive polymer, polyacetylene,[27] which led to the Nobel Prize in Chemistry in 2000.

One of the main design motifs in polymers is to include chemical functionalizations that allow for planar systems needed for charge delocalization along the conjugated backbone and to facilitate close intermolecular contacts and nanoscale molecular order for good mobilities; therefore, a great deal of research has been devoted to the design of new materials with targeted chemical functionalizations aimed towards creating favorable non-covalent intermolecular interactions such as hydrogen bonding, sulfur−fluorine interactions, and π−π stacking.[28-31] The interaction of the two materials used in OPVs is also a crucial aspect, for example, in the bulk heterojunction devices with several different domains of varying degrees of mixing between the (typically) electron-rich polymers and electron-deficient fullerenes;[32-34] this design motif has now reached efficiencies of ~10%.[35,36]

Understanding the full spectrum of the material structure-processing-property profile and the impact on charge-carrier transport is essential to the future viability of organic electronic devices.[2-4] However, a fundamental understanding of the nature of the (de)localization of the charge carrier in organic semiconductors is still unclear (and of particular focus in this dissertation) and fundamental aspects of charge transfer mechanisms are still under debate; this is partially due to charge-carrier mobilities of organic semiconductors being dramatically different depending on how the materials were processed (*e.g.*, either by vacuum or solution deposition). Indeed, highly-purified vacuum-deposited single-crystalline pentacene and rubrene have hole mobilities typically around 10 (but as high as 40) $cm^2V^{-1}s^{-1}$[37-39] and provide the upper limit of intrinsic mobilities because of the large electronic coupling present in the material (~100 meV) due to the π-π intermolecular interactions.[37,38,40-44] The best solution-processed crystals of substituted rubrene derivatives display mobilities less than 1 $cm^2V^{-1}s^{-1}$.[45]

Computational approaches can often be employed to screen materials for specific criteria such as energy level-alignment to facilitate a charge-transfer. However, having a reliable method capable of accurately modeling the (de)localization of the charge carrier in organic semiconductors is beyond standard computational approaches. Therefore, these methods have little use in elucidating the (still unclear) fundamental aspects of charge transfer mechanisms in organic semiconductors. The focus of this dissertation is on developing a methodology capable of investigating intermolecular and intramolecular charge transfer, which requires describing the (de)localization of the charge carrier in small-molecule organic semiconductors and a reliable quantum-mechanical approach to evaluate the transfer integrals and the related electronic band structures. Therefore, it is helpful to briefly describe the main models of charge transfer in organic semiconductors.

1.2. Charge Transport Models

1.2.1. Band Model

The development of charge transfer models for organic semiconductors stems from the investigation of simple (*e.g.*, solution-based) inter- and intramolecular charge-transfer reactions or through the application of the charge-transfer models developed for solid-state inorganic systems. For solid-state organic semiconductors, a limited delocalization of the electronic wavefunction is expected because the intermolecular forces are these relatively weak van der Waals interactions (as opposed to covalently-bound systems), with the wavefunction localized to a finite number of molecules (or even a single molecule) instead of extending over the entire

volume of the organic solid (*i.e.*, band model, which is the case for many inorganic solids). Although the actual charge-transport mechanism in organic semiconductors is still under debate, a band model is usually applied only to highly-ordered organic single crystals that have measured high mobilities such as purified crystalline acenes[39] and rubrene.[42] Angle-resolved photoelectron spectroscopy has also recently revealed a band-like dispersion in the highest-occupied state of pentacene and rubrene.[46-48] One diagnostic indicator of a delocalized electronic wavefunction is an observed decrease in mobility with an increase in temperature (*i.e.*, power law dependence of $\mu(T) \propto T^{-n}$) shown in Figure 1.1. Starting from 300K, the mobility begins to increase with a decrease in temperature as a result of a reduction in the number of charges stuck in deep trap-states within in the crystal that leads to an increased mobility. However, at T < 150 K, the mobility rapidly decreases with decreasing temperature because there is no longer enough thermal energy to move a charge carrier out of shallow traps, which now dominates the mobility. The anisotropy between the two peaks labeled *b*-axis and *a*-axis correspond to the mobility along different axes in the crystal structure with differences in the electronic coupling, with the *b*-direction having a large electronic coupling of ~100 meV. These examples are clear evidence that a band-like conduction is possible for non-covalently bound solids at low temperatures.

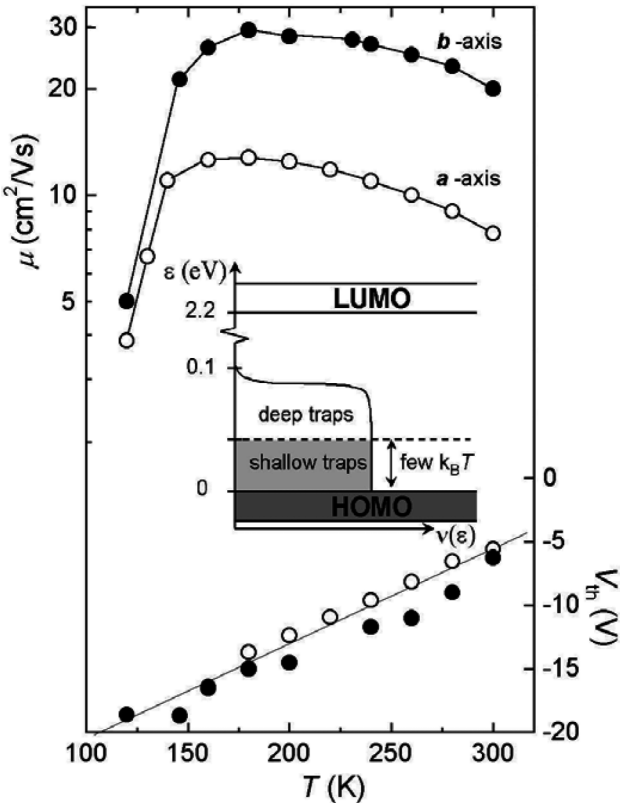

Figure 1.1. Field-effect mobility and threshold voltage with increasing temperature; measured along the *a* and *b* axes of rubrene crystal. Adapted from Ref. 42.

1.2.2. Hopping Model

With the exception of these few limited number of cases with particularly high molecular order, the mobility of a charge migrating through the organic semiconductor at room temperature is typically approximated as strongly localized charge hopping events between adjacent molecules under the influence of an applied electric field and is expected to be thermally activated (*i.e.*, the mobility increases with increasing temperature). In this so-called weak electronic-coupling limit (where the majority of organic materials are assumed to operate), the charge-transport process is generally described by Marcus electron transfer theory[49-54] for a one-electron transfer between two molecules (A and B):

$$A^+ + B \rightarrow A + B^+ \qquad \textbf{(1.1)}$$

The products and reactants can be depicted as separate charge-localized (diabatic) states approximated by harmonic functions.

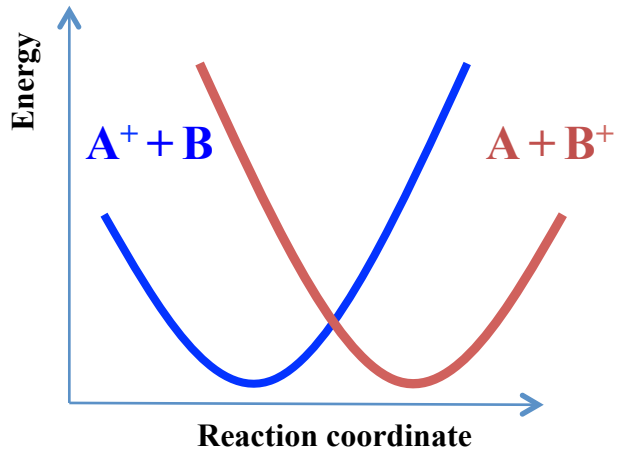

Figure 1.2. Electron transfer reaction represented by two harmonic functions to describe the charge-localized (diabatic) states.

The electron transfer process can occur with a vertical (*i.e.*, frozen nuclear coordinate) excitation from the reactants potential to the products potential in order to satisfy the Franck-Condon principle, with a subsequent relaxation to the nuclear coordinate of the products. The reaction can also proceed going through the transition state, where the diabatic states mix (avoided crossing) to form adiabatic states and the molecules involved in the reaction have the same geometry (for self-exchange reactions). In this context (where the tunneling through the barrier is neglected), the rate constant for electron or hole transfer (hopping), k_{ET}, can be defined in an Arrhenius-like manner as a series of simultaneous oxidation and reduction reactions:[52,55,56]

$$k_{ET} = \frac{4\pi^2}{h}\frac{1}{\sqrt{4\pi\lambda k_B T}}\, t^2 \exp\left[\frac{-(\lambda+\Delta G^o)}{4\lambda k_B T}\right], \qquad \textbf{(1.2)}$$

where T is temperature, k_B and h are the Boltzmann and Planck constants, respectively, ΔG^o is the Gibbs' free energy change during electron transfer, t is the electronic coupling (transfer integral) and λ is the reorganization energy. From Eq. (1.2), two requirements have to be satisfied for a fast charge transfer: a large t and small λ. Therefore, because of the importance of these parameters, we will briefly describe these terms.

1.3. Charge Transport Parameters

1.3.1. Intermolecular Coupling

The electronic coupling describes the strength of the electronic interaction amongst molecules and, to a first approximation, can be estimated quantum mechanically from the molecular (localized) representation as half the splitting between the highest occupied molecular orbital (HOMO) and HOMO-1 for a dimer configuration compared to the isolated single-molecule HOMO, as illustrated in Figure 1.3 (the exact calculation of t is discussed in more detail in Chapter 2).[57] In general, the so-called "energy splitting in dimer" method is based on the understanding that the intersection of the two parabolas in Figure 1.2 represents a transition point where the two molecules undergoing the charge transfer are equivalent (*i.e.*, the excess charge is equally distributed over both molecules).[57] Therefore, the energy difference between the first two adiabatic states calculated at that point corresponds to $2t$ (taken to be the first two occupied eigenvalues, shown in Figure 1.3). Of course, this calculation requires the symmetric (transition state) geometry of the charged dimer, which can be approximated by simply taking the geometry of the neutral dimer or mixing the neutral and charged geometries of each molecule. However, it

should be noted that this evaluation for the transfer integral fails when the two molecules are not perfectly cofacial[58] and leads to issues where the difference in site energies results in an overestimation of the computed electronic coupling. We also discuss in Chapter 6 the impact that the choice of Hamiltonian (*e.g.*, the choice of a given DFT functional) has on the magnitude of *t*.

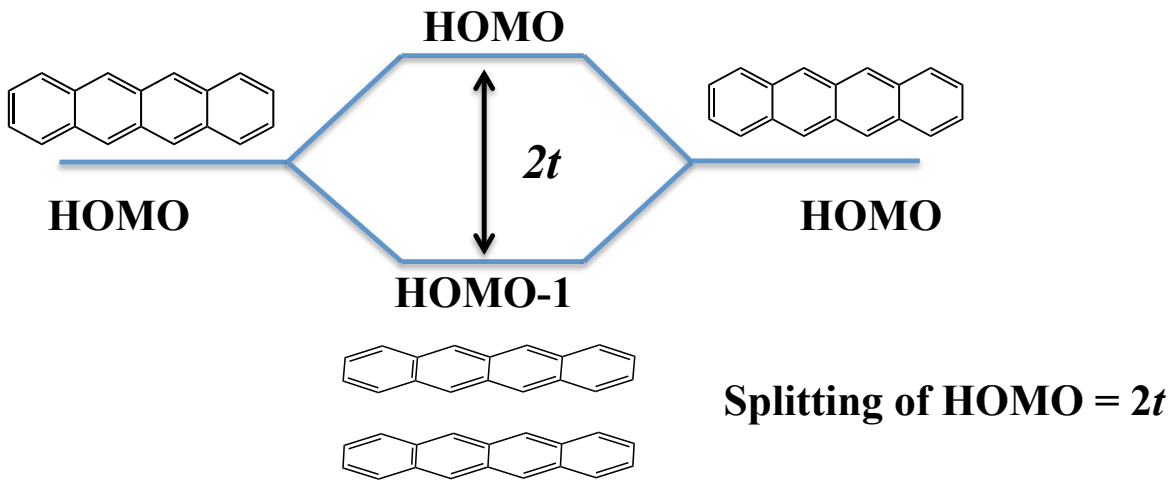

Figure 1.3. Illustration of the energy in splitting in dimer method, where half of the energy splitting in the two highest occupied orbitals of the dimer is taken to be *t*.

Because the transfer integral results from wavefunction overlap, the magnitude of the electronic coupling is sensitive to the phase and nodes for a particular molecular orbital (*e.g.*, HOMO). This additional consideration has dramatic implications for the transfer integral, see Figure 1.4. An oscillation is computed for the transfer integral for the HOMO and LUMO in a tetracene dimer. As one monomer is displaced from the perfectly cofacial situation, the *t* decreases and eventually goes to zero when the orbitals of one monomer overlaps with the node in the orbital for the other monomer.

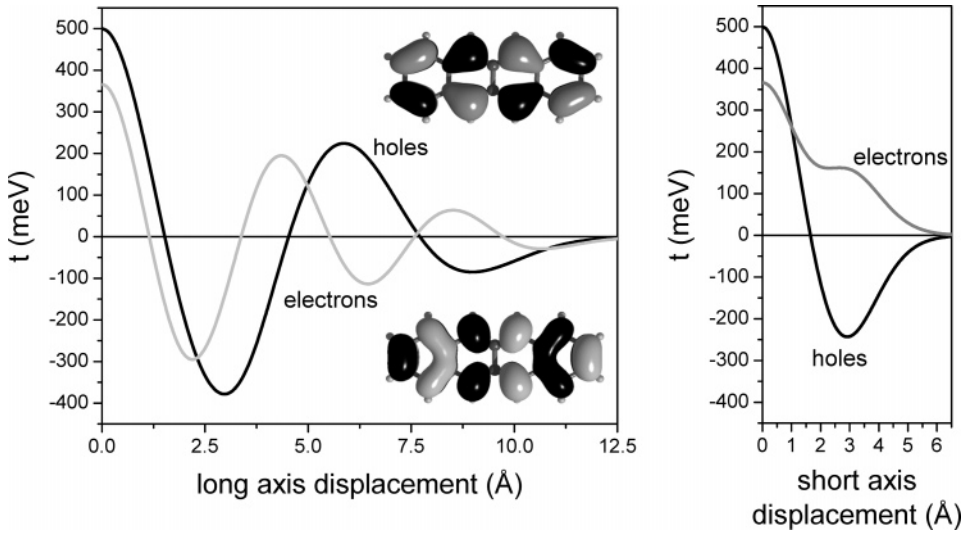

Figure 1.4. Evolution of ZINDO computed transfer integrals for a perfectly cofacial tetracene dimer displaced along the long axis. Adapted from Ref. 59.

1.3.2. Reorganization Energy

As a charge carrier moves through a bulk material, there is an associated relaxation of the molecule upon charge addition/removal and its surroundings (reorganization energy). The reorganization energy (λ) comprises both an intra-molecular (λ_i) component from the geometry change of a single molecule upon oxidation/reduction and an inter-molecular (λ_e) component from the electronic polarization of the surrounding molecules:

$$\lambda = \lambda_i + \lambda_e \qquad \textbf{(1.3)}$$

λ_i is evaluated from the theoretical evaluation or experimentally through, for example, gas-phase UPS measurements of individual molecules (see Figure 1.5), where the ionization process gives half of λ_i (*i.e.*, here, only one molecule undergoing the charge addition is considered in the self-exchange process and the charge removal process is neglected). The vibrational fine structure

present in the spectrum gives a measurement of the intramolecular vibrations coupled to the ionization process.

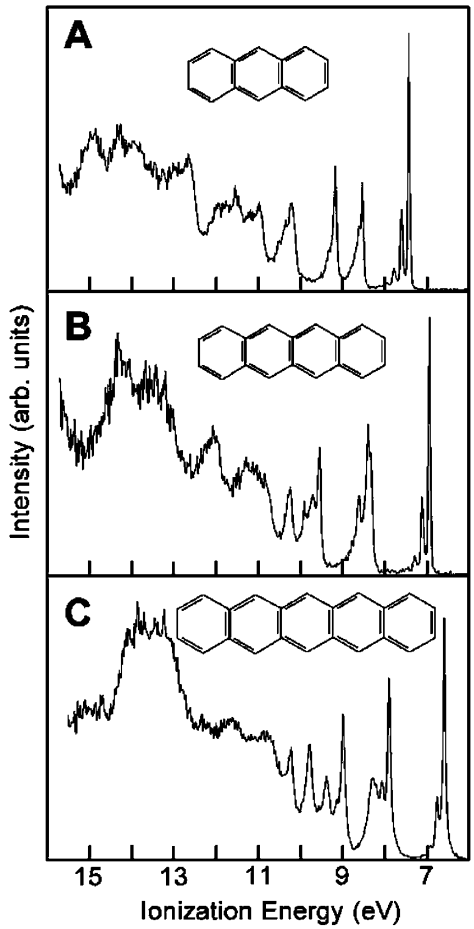

Figure 1.5. Gas-phase ultraviolet photoelectron spectra of anthracene, tetracene, and pentacene. Adapted from Ref. 60.

1.3.3. Electronic Polarization of the Environment

The inter-molecular (λ_e) contribution to the reorganization energy results from the polarization of the surrounding medium, in other words, the presence of a charge on a given molecule acts as

a perturbation to the electronic structure of the adjacent molecules, which results in an electronic polarization and a change in geometry.

The effect of polarization of a charge carrier can be seen with the difference between the energy gap of single molecule and that for the crystal (Figure 1.6). The polarization energy for a negative charge carrier can be expressed by:

$$P^{-} = EA_B - EA_G \quad \textbf{(1.4)}$$

where EA_G and EA_B are electron affinities of the single molecule in the gas-phase and crystalline bulk, respectively; the polarization energy for a positive charge carrier can be expressed as:

$$P^{+} = IP_G - IP_B \quad \textbf{(1.5)}$$

where the IP_G and IP_B are the ionization potentials of the single molecule in the gas-phase and the crystalline bulk.

Opposite trends are seen in the polarization energy for a hole and electron when going from a single molecule to the bulk that results from the stabilization of the excess charge. For an excess electron, the increase in polarization energy with increasing system size leads to an EA_B that is larger than that of the single molecule ($i.e., EA_G < EA_B$), whereas for an excess hole, the polarization energy stabilizes the excess positive charge and therefore makes it easier to ionize, thus $IP_G > IP_B$. While the polarization energy is dependent to a large degree on the molecular polarizability, the arrangement of adjacent molecules also has a large affect.[61-65] The effective polarization energy consists of charge-induced dipole interactions and charge-quadrupole interaction terms, thus resulting in P^{-} and P^{+} having different magnitudes.[61-63] For example, P^{+}

and P^- of naphthalene single crystal have been experimentally measured to be ~ 1.7 and 1.1 eV, respectively. [66]

Importantly, this understanding of polarization energy is only valid for weakly interacting molecules in organic semiconductors with small intermolecular couplings and, thus, a mostly localized charge. In Chapter 5, we model the evolution of both the charge carrier delocalization and the polarization energy as a function of system size using finite clusters of naphthalene, anthracene, tetracene, and pentacene.

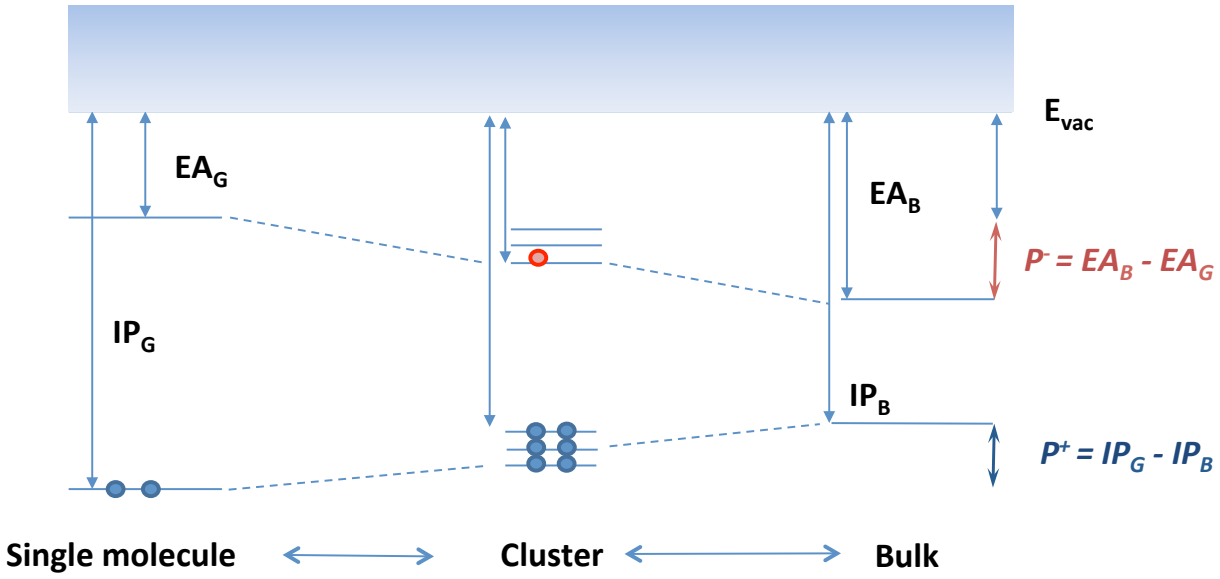

Figure 1.6. Illustration of the polarization energy present in a finite (cluster) or bulk system and the effect of this parameter on the energy levels of the system.

1.4. Intramolecular Charge Transport Systems

Thus far, the discussion of electron transfer has been framed in terms intermolecular charge transport within bulk organic semiconductors; however, it is important to note that electron transfer inter- and intramolecular reactions are found throughout biology, chemistry, and physics.[53,56,67-69] A significant fundamental understanding of electron transfer has been gained from prototypical intramolecular electron transfer systems, so-called mixed valence (MV) complexes. These compounds have two or more charge-bearing redox centers separated by bridge that mediates electron transfer process, whereby a charge can localize or delocalize depending on the degree of coupling between redox sites (t) relative to the magnitude of the Marcus-type reorganization energy (λ). Adopting the Robin-Day classification of MV compounds, these systems can be categorized using t and λ into: class I, class II, or class III.[70] For class-I MV systems, the redox centers are decoupled electronically – due to large physical separation of the centers, non-conjugated bridge, or selection rules – and leads to a localized charge and electronic properties that are similar to the isolated redox units.[70] In class-II MV systems, the redox centers are weakly coupled, with $2t < \lambda$ and therefore, the charge is localized with an associated barrier for the charge transfer process. This barrier can be overcome thermally or upon opitical absorption.[70] Conversely for class-III MV systems, the electronic coupling is larger than the reorganization energy ($2t > \lambda$) and the reaction is essentially barrierless with the charge effectively delocalizing over both centers. [70] Class-II and III MV systems display a broad intervalence charge-transfer (IVCT) or charge-resonance (CR) band in the near infrared or visible region of the absorbance specta that cannot be attributed to the separated redox centers or bridge.

We briefly introduced Marcus theory in the previous section and the importance of t and λ in determining the rate of *intermolecular* charge transfer. However, a significant breakthrough for understanding charge transport is the observation that electronic coupling can be quantified experimentally from the seminal work of Noel Hush in developing the two-state model to determine t.[71,72] In the two-state model, free energy surfaces of MV systems can be constructed from harmonic potentials for the diabatic states that represent the charged localized states involved in the charge transfer.[54,73,74] Electronic coupling of these diabatic states leads to a splitting of $2t$ at the intersection of the two diabatic surfaces, and therefore, t is most often calculated at the midpoint on the reaction coordinate (discussed above). The electronic coupling can be quantified experimentally through the generalized Mulliken-Hush approach, which allows t to be determined for MV systems from the deconvolution of absorbance spectra (*i.e.*, IVCT band shape) into Gaussian shaped peaks to get transition energies and transition moments:[74-76]

$$t = \frac{\mu_{12}\nu_{max}}{eR} \qquad \textbf{(1.6)}$$

where ν_{max} is the energy of the absorption band maximum, e is the electronic charge, and μ_{12} is the transition dipole moment; R (Å) is the electron transfer distance that is not directly accessible and is typically approximated using the redox center separation, though this approximation is known to be inaccurate.[77] In Chapter 4, we demonstrate a method capable of accurately describing MV systems spanning class-II and III and, therefore, has the potential for elucidating a better understanding of electron transfer in these systems.

1.5. Synopsis of Thesis

We begin in Chapter 2 with a brief review of the electronic structure methods that we use and then introduce the non-empirically procedure for DFT that allows for a substantial improvement over standard DFT methods. We then discuss the main results of this research. In Chapter 3, we detail the understanding of the limitations in DFT (currently one of our main tools) and improvements that can be achieved through non-empirically tuning a specific DFT method for the system of study. We detail the dependence of the range-separation parameter used in long-range corrected hybrid functionals on both the size and degree of conjugation for a given system. We also demonstrate the effect that self-interaction corrections employed through range-separated hybrid functionals can have in describing thermodynamic and electronic properties for large, organic π-conjugated systems. In this study, we chose a property that critically depends on the degree of delocalization (*i.e.*, torsion potentials) to correlate the degree of delocalization with the choice of a given method in order to understand how the self-interaction errors affects this property. These results are published in C. Sutton et al. "Accurate Description of Torsion Potentials in Conjugated Polymers using Density Functionals with Reduced Self-interaction Error" Journal of Chemical Physics, 140, 054310, 2014. In Chapter 4, we discuss how non-empirically tuning DFT can be used to rigorously model electron transfer in single-molecule systems (*i.e.*, organic mixed-valence systems), where we modeled the symmetry breaking and charge (de)localization in charge-transfer complexes compared with high-level methods. The results presented in Chapter 4 are published in C. Sutton et al. "Towards a Robust Quantum-Chemical Description of Organic Mixed-Valence Systems" Journal of Physical Chemistry C, 118, 3925, 2014. In Chapter 5, we applied this method to interpret photoelectron spectroscopy

spectra in order to elucidate the localized nature of a charge carrier in prototypical organic semiconductors; this understanding was then extended to quantify the relaxation energy in finite molecular clusters in the presence of an excess charge from a combined multi-layer quantum-mechanical/molecular-mechanical method. In Chapter 6, we determined the effect of choosing various DFT methods on the intermolecular electronic couplings and band structure calculations in organic molecules, which are published by C. Sutton et al. in "Understanding the Density Functional Dependence of DFT-Calculated Electronic Couplings in Organic Semiconductors" Journal of Physical Chemistry Letters, 4, 919, 2013 and have been submitted by A. Fonari et al. in "The Impact of Exact Exchange Energy in the Description of the Electronic Structure of Organic Charge Transfer Molecular Crystals". The connection between intermolecular electronic couplings and non-covalent interactions are also discussed in Chapter 6. Finally, conclusions and further considerations are discussed in Chapter 7.

1.6. References

1. Green, M. A.; Emery, K.; Hishikawa, Y.; Warta, W., Solar cell efficiency tables (version 37). *Progress in Photovoltaics: Research and Applications* **2011**, *19*, 84-92.
2. Karamertzanis, P. G.; Day, G. M.; Welch, G. W. A.; Kendrick, J.; Leusen, F. J. J.; Neumann, M. A.; Price, S. L., Modeling the interplay of inter- and intramolecular hydrogen bonding in conformational polymorphs. *The Journal of Chemical Physics* **2008**, *128*, 244708-17.
3. Price, S. L., Computed Crystal Energy Landscapes for Understanding and Predicting Organic Crystal Structures and Polymorphism. *Accounts of Chemical Research* **2008**, *42*, 117-126.
4. Wen, S.; Beran, G. J. O., Crystal Polymorphism in Oxalyl Dihydrazide: Is Empirical DFT-D Accurate Enough? *Journal of Chemical Theory and Computation* **2012**, *8*, 2698-2705.
5. Kang, J. H.; Filho, D. d. S.; Bredas, J. L.; Zhu, X. Y., Shallow trap states in pentacene thin films from molecular sliding. *Applied Physics Letters* **2005**, *86*, 152115-3.
6. Mattheus, C. C.; Dros, A. B.; Baas, J.; Oostergetel, G. T.; Meetsma, A.; de Boer, J. L.; Palstra, T. T. M., Identification of polymorphs of pentacene. *Synthetic Metals* **2003**, *138*, 475-481.
7. Jurchescu, O. D.; Mourey, D. A.; Subramanian, S.; Parkin, S. R.; Vogel, B. M.; Anthony, J. E.; Jackson, T. N.; Gundlach, D. J., Effects of polymorphism on charge transport in organic semiconductors. *Physical Review B* **2009**, *80*, 085201.
8. Dunitz, J. D.; Gavezzotti, A., How molecules stick together in organic crystals: weak intermolecular interactions. *Chemical Society Reviews* **2009**, *38*, 2622-2633.
9. Käfer, D.; El Helou, M.; Gemel, C.; Witte, G., Packing of Planar Organic Molecules: Interplay of van der Waals and Electrostatic Interaction. *Crystal Growth & Design* **2008**, *8*, 3053-3057.
10. Becerril, H. A.; Roberts, M. E.; Liu, Z.; Locklin, J.; Bao, Z., High-Performance Organic Thin-Film Transistors through Solution-Sheared Deposition of Small-Molecule Organic Semiconductors. *Advanced Materials* **2008**, *20*, 2588-2594.
11. Diao, Y.; Tee, B. C.-K.; Giri, G.; Xu, J.; Kim, D. H.; Becerril, H. A.; Stoltenberg, R. M.; Lee, T. H.; Xue, G.; Mannsfeld, S. C. B.; Bao, Z., Solution coating of large-area organic semiconductor thin films with aligned single-crystalline domains. *Nature Materials* **2013**, *12*, 6.
12. Anthony, J. E.; Eaton, D. L.; Parkin, S. R., A Road Map to Stable, Soluble, Easily Crystallized Pentacene Derivatives. *Organic Letters* **2001**, *4*, 15-18.
13. Curtis, M. D.; Cao, J.; Kampf, J. W., Solid-State Packing of Conjugated Oligomers: From π-Stacks to the Herringbone Structure. *Journal of the American Chemical Society* **2004**, *126*, 4318-4328.
14. Anthony, J. E., Functionalized Acenes and Heteroacenes for Organic Electronics. *Chemical Reviews* **2006**, *106*, 5028-5048.
15. Chi, X.; Li, D.; Zhang, H.; Chen, Y.; Garcia, V.; Garcia, C.; Siegrist, T., 5,6,11,12-Tetrachlorotetracene, a tetracene derivative with π-stacking structure: The synthesis, crystal structure and transistor properties. *Organic Electronics* **2008**, *9*, 234-240.
16. Liu, S.; Mannsfeld, S. C. B.; Wang, W. M.; Sun, Y.-S.; Stoltenberg, R. M.; Bao, Z., Patterning of α-Sexithiophene Single Crystals with Precisely Controlled Sizes and Shapes. *Chemistry of Materials* **2008**, *21*, 15-17.

17. Hong, J.-P.; Lee, S., Solution-Based Direct Growth of Organic Crystals on an Active Channel Region for Printable Bottom-Contact Organic Field-Effect Transistors. *Angewandte Chemie International Edition* **2009**, *48*, 3096-3098.
18. Nakayama, K.; Hirose, Y.; Soeda, J.; Yoshizumi, M.; Uemura, T.; Uno, M.; Li, W.; Kang, M. J.; Yamagishi, M.; Okada, Y.; Miyazaki, E.; Nakazawa, Y.; Nakao, A.; Takimiya, K.; Takeya, J., Patternable Solution-Crystallized Organic Transistors with High Charge Carrier Mobility. *Advanced Materials* **2011**, *23*, 1626-1629.
19. Minemawari, H.; Yamada, T.; Matsui, H.; Tsutsumi, J. y.; Haas, S.; Chiba, R.; Kumai, R.; Hasegawa, T., Inkjet printing of single-crystal films. *Nature* **2011**, *475*, 3.
20. Sele, C. W.; Kjellander, B. K. C.; Niesen, B.; Thornton, M. J.; van der Putten, J. B. P. H.; Myny, K.; Wondergem, H. J.; Moser, A.; Resel, R.; van Breemen, A. J. J. M.; van Aerle, N.; Heremans, P.; Anthony, J. E.; Gelinck, G. H., Controlled Deposition of Highly Ordered Soluble Acene Thin Films: Effect of Morphology and Crystal Orientation on Transistor Performance. *Advanced Materials* **2009**, *21*, 4926-4931.
21. Uemura, T.; Hirose, Y.; Uno, M.; Takimiya, K.; Takeya, J., Very High Mobility in Solution-Processed Organic Thin-Film Transistors of Highly Ordered [1]Benzothieno[3,2-b]benzothiophene Derivatives. *Applied Physics Express* **2009**, *2*, 3.
22. Pisula, W.; Menon, A.; Stepputat, M.; Lieberwirth, I.; Kolb, U.; Tracz, A.; Sirringhaus, H.; Pakula, T.; Müllen, K., A Zone-Casting Technique for Device Fabrication of Field-Effect Transistors Based on Discotic Hexa-peri-hexabenzocoronene. *Advanced Materials* **2005**, *17*, 684-689.
23. Rivnay, J.; Jimison, L. H.; Northrup, J. E.; Toney, M. F.; Noriega, R.; Lu, S.; Marks, T. J.; Facchetti, A.; Salleo, A., Large modulation of carrier transport by grain-boundary molecular packing and microstructure in organic thin films. *Nature Materials* **2009**, *8*, 6.
24. Chen, J.; Tee, C. K.; Shtein, M.; Martin, D. C.; Anthony, J., Controlled solution deposition and systematic study of charge-transport anisotropy in single crystal and single-crystal textured TIPS pentacene thin films. *Organic Electronics* **2009**, *10*, 696-703.
25. Li, H.; Tee, B. C. K.; Cha, J. J.; Cui, Y.; Chung, J. W.; Lee, S. Y.; Bao, Z., High-Mobility Field-Effect Transistors from Large-Area Solution-Grown Aligned C60 Single Crystals. *Journal of the American Chemical Society* **2012**, *134*, 2760-2765.
26. Li, H.; Tee, B. C. K.; Giri, G.; Chung, J. W.; Lee, S. Y.; Bao, Z., High-Performance Transistors and Complementary Inverters Based on Solution-Grown Aligned Organic Single-Crystals. *Advanced Materials* **2012**, *24*, 2588-2591.
27. Chiang, C. K.; Fincher, C. R.; Park, Y. W.; Heeger, A. J.; Shirakawa, H.; Louis, E. J.; Gau, S. C.; MacDiarmid, A. G., Electrical Conductivity in Doped Polyacetylene. *Physical Review Letters* **1977**, *39*, 1098-1101.
28. Kim, B.-G.; Jeong, E. J.; Chung, J. W.; Seo, S.; Koo, B.; Kim, J., A molecular design principle of lyotropic liquid-crystalline conjugated polymers with directed alignment capability for plastic electronics. *Nature Materials* **2013**, *12*.
29. De Cremer, L.; Verbiest, T.; Koeckelberghs, G., Influence of the Substituent on the Chiroptical Properties of Poly(thieno[3,2-b]thiophene)s. *Macromolecules* **2008**, *41*, 568-578.
30. Tsao, H. N.; Cho, D. M.; Park, I.; Hansen, M. R.; Mavrinskiy, A.; Yoon, D. Y.; Graf, R.; Pisula, W.; Spiess, H. W.; Müllen, K., Ultrahigh Mobility in Polymer Field-Effect Transistors by Design. *Journal of the American Chemical Society* **2011**, *133*, 2605-2612.
31. Kline, J. R.; McGehee, M. D.; Toney, M. F., Highly oriented crystals at the buried interface in polythiophene thin-film transistors. *Nature Materials* **2006**, *5*, 222.

32. Halls, J. J. M.; Walsh, C. A.; Greenham, N. C.; Marseglia, E. A.; Friend, R. H.; Moratti, S. C.; Holmes, A. B., Efficient photodiodes from interpenetrating polymer networks. *Nature* **1995**, *376*, 2.
33. Yu, G.; Gao, J.; Hummelen, J. C.; Wudl, F.; Heeger, A. J., Polymer Photovoltaic Cells: Enhanced Efficiencies via a Network of Internal Donor-Acceptor Heterojunctions. *Science* **1995**, *270*, 1789-1791.
34. Yu, G.; Heeger, A. J., Charge separation and photovoltaic conversion in polymer composites with internal donor/acceptor heterojunctions. *Journal of Applied Physics* **1995**, *78*, 4510-4515.
35. He, Z.; Zhong, C.; Su, S.; Xu, M.; Wu, H.; Cao, Y., Enhanced power-conversion efficiency in polymer solar cells using an inverted device structure. *Nature Photonics* **2012**, *6*, 4.
36. You, J.; Dou, L.; Yoshimura, K.; Kato, T.; Ohya, K.; Moriarty, T.; Emery, K.; Chen, C.-C.; Gao, J.; Li, G.; Yang, Y., A polymer tandem solar cell with 10.6% power conversion efficiency. *Nature Communications* **2013**, *4*.
37. Takeya, J.; Yamagishi, M.; Tominari, Y.; Hirahara, R.; Nakazawa, Y.; Nishikawa, T.; Kawase, T.; Shimoda, T.; Ogawa, S., Very high-mobility organic single-crystal transistors with in-crystal conduction channels. *Applied Physics Letters* **2007**, *90*, 102120-3.
38. Podzorov, V.; Pudalov, V. M.; Gershenson, M. E., Field-effect transistors on rubrene single crystals with parylene gate insulator. *Applied Physics Letters* **2003**, *82*, 1739-1741.
39. Karl, N., Charge carrier transport in organic semiconductors. *Synthetic Metals* **2003**, *133-134*, 649-657.
40. Jurchescu, O. D.; Baas, J.; Palstra, T. T. M., Effect of impurities on the mobility of single crystal pentacene. *Applied Physics Letters* **2004**, *84*, 3061-3063.
41. Sundar, V. C.; Zaumseil, J.; Podzorov, V.; Menard, E.; Willett, R. L.; Someya, T.; Gershenson, M. E.; Rogers, J. A., Elastomeric Transistor Stamps: Reversible Probing of Charge Transport in Organic Crystals. *Science* **2004**, *303*, 1644-1646.
42. Podzorov, V.; Menard, E.; Borissov, A.; Kiryukhin, V.; Rogers, J. A.; Gershenson, M. E., Intrinsic Charge Transport on the Surface of Organic Semiconductors. *Physical Review Letters* **2004**, *93*, 086602.
43. Podzorov, V.; Gershenson, M. E., Photoinduced Charge Transfer across the Interface between Organic Molecular Crystals and Polymers. *Physical Review Letters* **2005**, *95*, 016602.
44. Tatsuo, H.; Jun, T., Organic field-effect transistors using single crystals. *Science and Technology of Advanced Materials* **2009**, *10*, 024314.
45. Stingelin-Stutzmann, N.; Smits, E.; Wondergem, H.; Tanase, C.; Blom, P.; Smith, P.; de Leeuw, D., Organic thin-film electronics from vitreous solution-processed rubrene hypereutectics. *Nature Materials* **2005**, *4*, 7.
46. Machida, S.-i.; Nakayama, Y.; Duhm, S.; Xin, Q.; Funakoshi, A.; Ogawa, N.; Kera, S.; Ueno, N.; Ishii, H., Highest-Occupied-Molecular-Orbital Band Dispersion of Rubrene Single Crystals as Observed by Angle-Resolved Ultraviolet Photoelectron Spectroscopy. *Physical Review Letters* **2010**, *104*, 156401.
47. Koch, N.; Vollmer, A.; Salzmann, I.; Nickel, B.; Weiss, H.; Rabe, J. P., Evidence for Temperature-Dependent Electron Band Dispersion in Pentacene. *Physical Review Letters* **2006**, *96*, 156803.
48. Hatch, R. C.; Huber, D. L.; Höchst, H., Electron-Phonon Coupling in Crystalline Pentacene Films. *Physical Review Letters* **2010**, *104*, 047601.

49. Marcus, R. A., On the Theory of Oxidation-Reduction Reactions Involving Electron Transfer. I. *The Journal of Chemical Physics* **1956**, *24*, 966-978.
50. Marcus, R. A., Exchange reactions and electron transfer reactions including isotopic exchange. Theory of oxidation-reduction reactions involving electron transfer. Part 4.-A statistical-mechanical basis for treating contributions from solvent, ligands, and inert salt. *Discussions of the Faraday Society* **1960**, *29*, 21-31.
51. Marcus, R. A., On the Theory of Electron-Transfer Reactions. VI. Unified Treatment for Homogeneous and Electrode Reactions. *The Journal of Chemical Physics* **1965**, *43*, 679-701.
52. Marcus, R. A., Electron transfer reactions in chemistry. Theory and experiment. *Reviews of Modern Physics* **1993**, *65*, 599.
53. Marcus, R. A.; Sutin, N., Electron transfers in chemistry and biology. *Biochimica et Biophysica Acta (BBA) - Reviews on Bioenergetics* **1985**, *811*, 265-322.
54. Marcus, R. A.; Sutin, N., The Relation Between the Barriers for Thermal and Optical Electron Transfer Reactions in Solution. *Comments on Inorganic Chemistry* **1986**, *5*, 119-133.
55. Marcus, R. A., On the Theory of Oxidation-Reduction Reactions Involving Electron Transfer. I. *The Journal of Chemical Physics* **1956**, *24*, 966-978.
56. Barbara, P. F.; Meyer, T. J.; Ratner, M. A., Contemporary Issues in Electron Transfer Research. *The Journal of Physical Chemistry* **1996**, *100*, 13148-13168.
57. Newton, M. D., Quantum chemical probes of electron-transfer kinetics: the nature of donor-acceptor interactions. *Chemical Reviews* **1991**, *91*, 767-792.
58. Valeev, E. F.; Coropceanu, V.; da Silva Filho, D. A.; Salman, S.; Bredas, J. L., Effect of Electronic Polarization on Charge-Transport Parameters in Molecular Organic Semiconductors. *Journal of the American Chemical Society* **2006**, *128*, 9882-9886.
59. Coropceanu, V.; Cornil, J.; da Silva Filho, D. A.; Olivier, Y.; Silbey, R.; Bredas, J. L., Charge Transport in Organic Semiconductors. *Chemical Reviews* **2007**, *107*, 926-952.
60. Coropceanu, V.; Malagoli, M.; da Silva Filho, D. A.; Gruhn, N. E.; Bill, T. G.; Bredas, J. L., Hole- and Electron-Vibrational Couplings in Oligoacene Crystals: Intramolecular Contributions. *Physical Review Letters* **2002**, *89*, 275503.
61. Bounds, P. J.; Munn, R. W., Polarization energy of a localized charge in a molecular crystal.III submolecule treatment. *Chemical Physics* **1981**, *59*, 47-53.
62. Bounds, P. J.; Munn, R. W., Polarization energy of a localized charge in a molecular crystal. II. Charge-quadrupole energy. *Chemical Physics* **1981**, *59*, 41-45.
63. Eisenstein, I.; Munn, R. W., Polarization energy of a localized charge in a molecular crystal. VI. Effect of excitons. *Chemical Physics* **1983**, *79*, 189-195.
64. Norton, J. E.; Bredas, J. L., Polarization Energies in Oligoacene Semiconductor Crystals. *Journal of the American Chemical Society* **2008**, *130*, 12377-12384.
65. Ryno, S. M.; Lee, S. R.; Sears, J. S.; Risko, C.; Bredas, J. L., Electronic Polarization Effects upon Charge Injection in Oligoacene Molecular Crystals: Description via a Polarizable Force Field. *The Journal of Physical Chemistry C* **2013**, *117*, 13853-13860.
66. Sato, N.; Inokuchi, H.; Silinsh, E. A., Reevaluation of electronic polarization energies in organic molecular crystals. *Chemical Physics* **1987**, *115*, 269-277.
67. Gray, H. B.; Winkler, J. R., Electron Transfer in Proteins. *Annual Review of Biochemistry* **1996**, *65*, 537-561.
68. Huynh, M. H. V.; Meyer, T. J., Proton-Coupled Electron Transfer. *Chemical Reviews* **2007**, *107*, 5004-5064.

69. Newton, M. D.; Sutin, N., Electron Transfer Reactions in Condensed Phases. *Annual Review of Physical Chemistry* **1984**, *35*, 437-480.
70. Robin, M. B.; Day, P., Mixed Valence Chemistry- A Survey and Classification. In *Adv. Inorg. Chem. Radiochem.*, Academic Press;: 1967; Vol. 10, p 247.
71. Hush, N. S., Homogeneous and heterogeneous optical and thermal electron transfer. *Electrochimica Acta* **1968**, *13*, 1005-1023.
72. Hush, N. S., Intervalence-Transfer Absorption. Part 2. Theoretical Considerations and Spectroscopic Data. In *Progress in Inorganic Chemistry*, John Wiley & Sons, Inc.: 2007; pp 391-444.
73. Sutin, N., *Prog. Inorg. Chem.* **1983**, *30*, 441.
74. Creutz, C.; Newton, M. D.; Sutin, N., Metal—lingad and metal—metal coupling elements. *Journal of Photochemistry and Photobiology A: Chemistry* **1994**, *82*, 47-59.
75. Newton, M. D., Quantum Chemical Probes Of Electron-Transfer Kinetics - The Nature Of Donor-Acceptor Interactions. *Chemical Reviews* **1991**, *91*, 767-792.
76. Cave, R. J.; Newton, M. D., Generalization of the Mulliken-Hush treatment for the calculation of electron transfer matrix elements. *Chemical Physics Letters* **1996**, *249*, 15-19.
77. Nelsen, S. F.; Konradsson, A. E.; Weaver, M. N.; Telo, J. P., Intervalence Near-IR Spectra of Delocalized Dinitroaromatic Radical Anions. *Journal of the American Chemical Society* **2003**, *125*, 12493-12501.

Chapter 2 Computational Methodology

In this section we describe the various methods we have used for understanding the electronic structure and charge transport in organic single-molecules and solid materials.

2.1. Density Functional Theory

2.1.1. The Hohenberg-Kohn Theorems

The Hohenberg and Kohn theorems are the foundation of DFT.[1] The first theorem states that the electron density of a ground state uniquely determines the Hamiltonian and thus all properties of the system. The second theorem states the total energy density functional delivers its lowest energy for the exact ground state density (which is verified through the variational principle).

Central to all DFT approaches is the construction of a model system with the same ground state density as the real system and a functional of that density that returns the energy of the real system. The ground state density is defined as the probability density (ρ) of finding an electron at position *r* and time *t*:

$$\rho(r,t) = N \int d^3r_2 \ \dots \int d^3r_N \ |\varphi(r_1, r_2, r_3, \dots, r_N, t)|^2, \qquad \textbf{(2.1)}$$

where *N* is the total number of electrons. The one-to-one correspondence was summarized by Bright-Wilson as:[2] 1) the integral of the density gives the number of electrons; 2) the cusp of the density gives the position of the nuclei; 3) the height of the cusps gives the magnitude of the nuclear charge, which defines the density that is related to the many-body wavefunction.

2.1.2. The Kohn-Sham and Generalized Kohn-Sham Equations

In the Kohn-Sham (KS)[3] approximation to DFT, the solution of the ground-state density is obtained from the following independent-particle Schrödinger equation (*i.e.*, based on a determinant of single- particle Kohn-Sham orbitals ϕ_i):

$$\left[-\frac{1}{2}\nabla^2 + \mathrm{V}(\mathrm{r};\mathrm{R}) + \mathrm{V_H}(\mathrm{r}) + \mathrm{V_{xc}}(\mathrm{r})\right]\phi_i = \varepsilon_i\phi_i, \qquad \textbf{(2.2)}$$

where the first term is the kinetic energy operator, where ∇^2 (Laplacian operator) is a second partial derivative with respect to spatial coordinates, $\mathrm{V}(\mathrm{r};\mathrm{R})$ is the external potential,

$$\mathrm{V}(\mathrm{r};\mathrm{R}) = -\int \rho(\mathrm{r}) \sum_A \frac{\mathrm{Z}_A}{|r - \mathrm{R}_A|}\mathrm{dr} \qquad \textbf{(2.3)}$$

and $\mathrm{V_H}(\mathrm{r})$ is the Hartree potential which defines the classical electrostatic interactions among the electrons,

$$\mathrm{V_H}(\mathrm{r}) = \frac{1}{2}\int\int \frac{\rho(\mathrm{r})\rho(\mathrm{r}')}{|\mathrm{r} - \mathrm{r}'|}\mathrm{drdr}', \qquad \textbf{(2.4)}$$

where $\rho(\mathrm{r})$ is the electron density: $\rho(\mathrm{r}) = \sum_i |\phi_i(\mathrm{r})|^2$.

The development of DFT functionals involves the approximation of the exchange-correlation potential, $\upsilon_{\mathrm{xc}}(\mathrm{r})$, defined by the partial derivative of the exchange-correlation energy, $\upsilon_{\mathrm{xc}}(\mathrm{r}) = \frac{\delta \mathrm{E_{xc}^{KS}}}{\delta \mathrm{n}(\mathrm{r})}$. Thus, in DFT, the focus is on finding a suitable exchange-correlation functional that uses the electron density to describe the intricate many-body effects within a single particle formalism. There have been a great number of exchange-correlation functionals published since

the publication of the Hohenberg and Kohn theorems; therefore, we will now detail the various choices for approximate exchange-correlation functionals.

2.1.3. Functionals for Exchange and Correlation

2.1.3.1. The local density approximation

Numerous approximations have been developed for E_{xc}^{KS}. For the simplest DFT functional, the local density approximation (LDA) for exchange-correlation (*e.g.*, SVWN[1,3-5]) is a basic model in that the exchange-correlation potential depends only on the local, homogenous values of the electron density of the system $\rho(\mathrm{r})$:

$$E_{\mathrm{XC}}(\rho) = \int \rho(\mathrm{r})\varepsilon_{\mathrm{XC}}\,(\rho(\mathrm{r}))\,\mathrm{dr}. \qquad \textbf{(2.5)}$$

The exchange-correlation functional can be separated, with the exchange for LDA derived for a uniform electron gas in the 1930s by Dirac[6]:

$$E_X^{LDA}(\rho) = -\frac{3}{4}\left(\frac{3}{\pi}\right)^{1/3}\int \rho^{4/3}\ \mathrm{dr} \qquad \textbf{(2.6)}$$

And the correlation function being derived by Monte Carlo simulations of the uniform gas.[7]

2.1.3.2. The generalized gradient approximation

The generalized gradient approximation (GGA) for the exchange-correlation functional improves on LDA, not just by integrating at a point (as in LDA), but also integrating the gradient of that point $\nabla\rho(\mathrm{r})$. That is, the electron density of the system is supplemented with information from the gradient of the charge density to account for non-homogeneity:

$$E_{\mathrm{XC}}(\rho) = \int \rho(\mathrm{r})\varepsilon_{\mathrm{XC}}^{GGA}\,(\rho(\mathrm{r}), \nabla^2\rho(\mathrm{r}))\,dr. \qquad \textbf{(2.7)}$$

These functionals can be described as semilocal because they are no longer strictly local (*i.e.*, $\rho(\mathrm{r})$). Standard pure GGA functionals include PBE[8,9] and BP86.[10,11]

The meta-GGA functionals comprise another category of DFT functionals that improve on LDA and GAA methods to implement second-order derivatives such as the Laplacian of the electron density $\nabla^2\rho(\mathrm{r})$, and the electron kinetic energy density $\tau = \frac{1}{2}\sum_i|\nabla\phi_i|^2$.

2.1.3.3. Hybrid functionals

A major advance in the performance of approximate DFT functionals arose with the development of hybrid functionals that employ the adiabatic connection to smoothly connect the non-interacting KS system to the physical interacting system,[11,12] giving rise to the generalized KS (GKS) equations. This can be seen by re-writing the KS Hamiltonian, to using a sum of the KS potential stemming from the semilocal portion of the functional and a fraction of the orbital-specific Fock potential operator coming from the fractional exact exchange part to give:

$$\left[-\frac{1}{2}\nabla^2 + \mathrm{V}(\mathrm{r};\mathrm{R}) + V_{\mathrm{H}}(\mathrm{r}) + \alpha(\mathrm{r})V_X^{HF} + V_{XC}^{\alpha(\mathrm{r})}(\mathrm{r})\right]\phi_i = \varepsilon_i\phi_i \qquad \textbf{(2.8)}$$

where $V_{XC}^{\alpha(\mathrm{r})}(\mathrm{r})$ is the exchange-correlation potential, which now depends on the fraction of nonlocal exchange included in the model, $\alpha(\mathrm{r})$ and V_X^{HF} is the exact nonlocal exchange from Hartree-Fock (HF) theory computed with the GKS orbitals to give:

$$E_X^{HF} = -\frac{1}{2}\sum_{ij}\int\int \frac{\phi_j(\mathrm{r})\phi_j^*(\mathrm{r}')\phi_i^*(\mathrm{r})\phi_i(\mathrm{r}')}{|\mathrm{r}-\mathrm{r}'|}d\mathrm{r}d\mathrm{r}'. \quad \textbf{(2.9)}$$

The definition of a hybrid functional thus requires, in addition to the definition of the exchange-correlation potential, the designation of $\alpha(\mathrm{r})$. The standard global hybrid (GH) functionals include a static fraction of the coupling, *i.e.*, $\alpha(\mathrm{r}) = \alpha$.

Meta-GGA and GGA methods can include a mixture of non-local HF exchange with DFT exchange-correlation to form hybrid DFT functionals. One example for a pure meta-GGA functional is M06-L.[13] Meta-GGA and GGA methods can include a mixture of nonlocal HF exchange with DFT exchange-correlation to form hybrid DFT functionals. The hybrid-GGA functionals B3LYP[14,15] and PBE0[16] were used in this study, which contain 20% and 25% HF-exchange, respectively. Hybrid meta-GGA functionals analyzed herein were BMK,[17] and the family of functionals from Truhlar: M06,[18] M06-2X,[18] and M06-HF.[19] For M06-L, BMK, M06, M06-2X, and M06-HF there is 0%, 42%, 27%, 54% and 100% HF exchange, respectively.

Most of the developments of DFT focused on describing simple chemical observables such as the ability to have functionals that could give a reasonable description of both the geometries and dissociation energies of molecules and numerous approximate functionals of this type have been developed with great success.[20-23] Subsequently, approximate functionals focused on accurately predicting reaction barrier heights that would allow for the determination of the kinetics for chemical reactions and then several advances in incorporating van der Waals interactions within a given functional. However, these approximate exchange-correlation potentials within global hybrid functionals decay too quickly with distance, which results in a spurious self-repulsion due

to the incomplete cancellation of the long-range Coulomb self-interactions in $V_H(\mathrm{r})$.[24,25] The Coulomb self-interactions are exactly cancelled by HF exchange; thus, in principle, a GH approximation that completely incorporates the interacting system (α = 1) can overcome the spurious long-range self-repulsion; however, this leads to localization errors[26] and poor results in combination with standard (local) correlation functionals.[27]

2.1.3.4. Long-range corrected functionals

Recent developments to overcome these issues in molecular compounds include long-range corrected (LRC) functionals that introduce a partitioning of the electron-electron Coulomb operator into short-range description (*e.g.*, DFT) and long-range description (*e.g.*, HF) using, for example, the standard error function:[28-31]

$$\frac{1}{r_{12}} = \frac{1-\mathrm{erf}(\omega r_{12})}{r_{12}} + \frac{\mathrm{erf}(\omega r_{12})}{r_{12}} \qquad \textbf{(2.10)}$$

where ω is the Coulomb attenuation parameter. LRC functionals include: ωPBE, ωPBEh,[32] ωB97,[33] ωB97X,[33] ωB97X-D,[34] BOP[35], and BNL.[29,36] The LRC approaches have proven very successful for many applications of interest for organic electronics given the appropriate choice of the range-separation parameter ω that has been recently reviewed.[31,37]

The advantage of LRC DFT methods is the asymptotic decay of the exchange-correlation potential is strictly enforced and overcomes the issues of standard DFT functionals decaying too quickly, which is shown in Figure 2.1, where the LRC functional BNL falls along the 1/r plot.

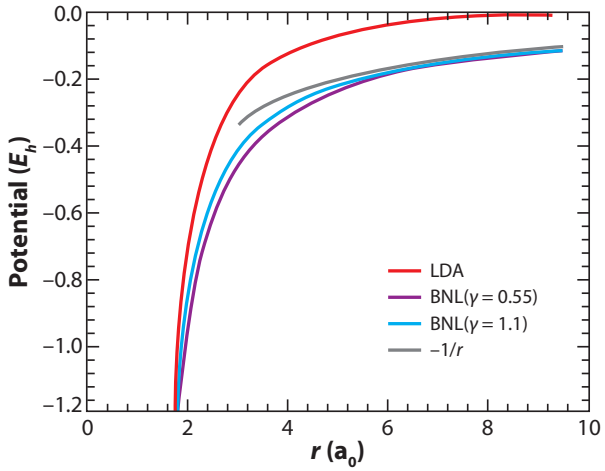

Figure 2.1. Three DFT potentials plotted explicitly including the standard local density approximation (LDA) and two long-range corrected DFT BNL potentials with a different Coulomb attenuation parameter compared with the explicitly shown −1/r Coulomb potential tail. Adapted from Ref. 31.

2.1.4. Many Electron Self interaction Error

It is helpful at this stage to consider the many-electron self-interaction error (MESIE) that has been discussed extensively in the literature on density functional approximations. Following Refs. 38,39, an approximation to the exchange-correlation functional is called free from MESIE if it obeys a property required of the exact exchange-correlation functional in the case of fractional particle numbers, which is that the total energy as a function of fractional occupation must correspond to a series of straight lines with kinks at integer occupations.[40] The rigorous derivation of the change in energy with fractional orbital occupation comes from Janak's Theorem.[41] In this context, neither HF (which is free from one-electron self-interaction errors) nor any of the commonly used density functional approximations are free from MESIE. However, the deviations from the straight-line behavior are different for HF and DFT. Standard DFT functionals yield convex curves for energy vs. fractional occupation, which is consistent with the fact that they favor delocalized over localized charges; in contrast, curves obtained from HF theory are concave, *i.e.*, consistent with HF spuriously favoring charge localization (the MESIEs in HF and DFT are frequently referred to as localization and delocalization errors, respectively).[27,26]

The manifestation of this error can be seen in Figure 2.2, adapted from Ref. 42, where Yang and co-workers, demonstrated for H_2^+ separated along the inter-atomic distance to the infinite limit could lead to two very different descriptions. For the exact solution, the ΔE went to zero as the two nuclei became separated by ~ 4 Å and plateaued at around that separation until the infinite limit. For two standard DFT approaches, LDA and B3LYP, the energy actually decreased with increased inter-atomic separation to give the electron unphysically spread out over both nuclei

even when separated by infinity. Also note that there is a difference in the energy between LDA and B3LYP, which is slightly close to the exact solution for B3LYP and primarily comes from the difference of the amount of HF exchange included in the functional: 0% HF exchange in LDA and 20% HF exchange in B3LYP. Therefore, an additional important consequence is realized: HF exchange corrects the SIE in standard DFT approaches.

When the two atoms are separated by infinity, there is essentially a half of an electron on each nucleus and therefore, with standard DFT dramatically underestimating the energy for fractional charges (*i.e.*, at the infinite limit). The energy difference at this infinite limit gives a definition for the magnitude of the self-interaction error, which is ~ 50 – 60 kcal mol^{-1} for this system. In order to understand the error in a given functional, we can use fractional charges as a way to understand the inherent errors for a given DFT functional.

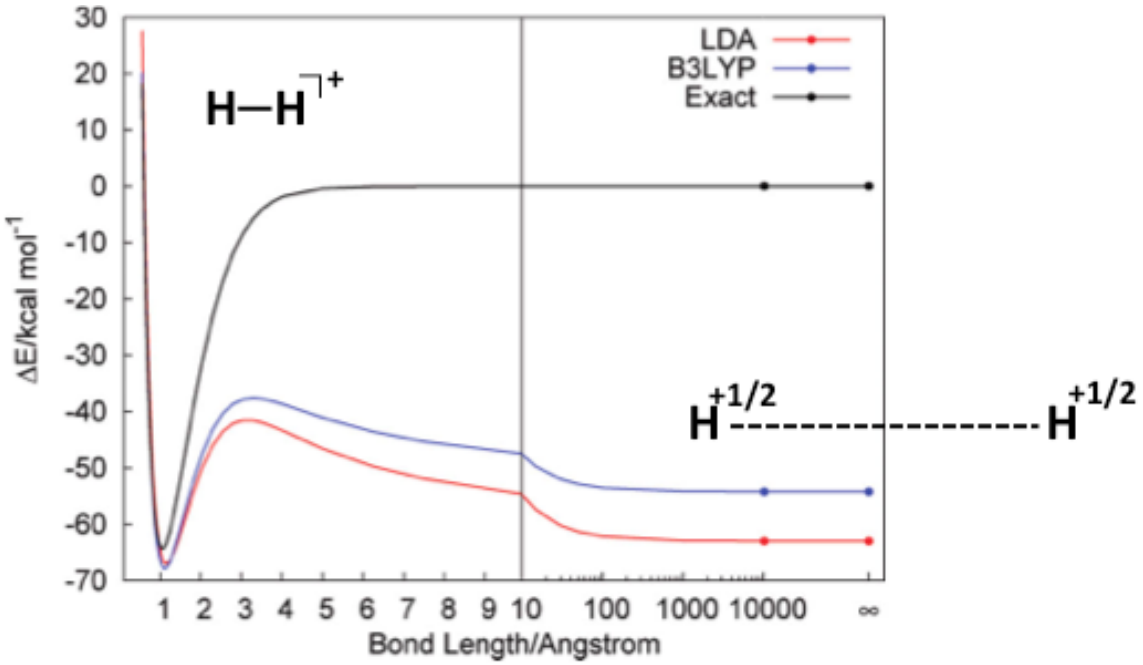

Figure 2.2. Change in energy for H_2^+ as a function of intermolecular separation computed with the Exact solution (black), and DFT methods LDA (red) and B3LYP (blue). Adapted from Ref. 42.

The localization/delocalization errors of HF and LDA can be quantified based on the total energy curve for fractional particle numbers when going from H to H^+ (Figure 2.3) (*i.e.*, upon ionization), where the fractional particle numbers are computed based on number of electrons per H atom. The linear trend with energy for fractional particle numbers is shown computed exactly from Ref. 42 on the left panel, whereas deviation from linearity of the total energy is shown as an illustration superimposed on the right panel. For standard semilocal functionals such as LDA, a convex curve is obtained, as situations with fractional particle numbers are spuriously favored over situations with integer particle numbers (*i.e.*, a delocalized density). The opposite occurs for methods such as HF where a concave curve results when integer particle numbers are spuriously favored over situations with fractional charges and results in a localization error.

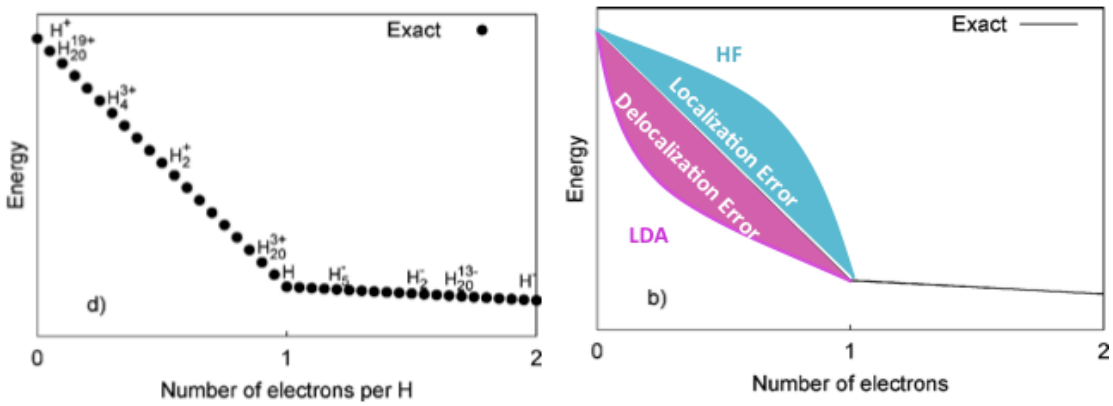

Figure 2.3. Change in energy with fractional occupation numbers computed from the exact solution (left), with a cartoon of what is expected using LDA and HF (right). Adapted from Ref. 42.

2.1.5. Nonempirically Tuning

Recently, long-range corrected (LRC) functionals have been introduced as a way to reduce the MESIE and provide a better balance between localization and delocalization effects.[43-45] The optimal, *i.e.*, MESIE minimizing, range-separation parameter ω is determined following the "IP-tuning" procedure using the DFT analogue of Koopman's theorem,[46] where the difference between the HOMO eigenvalue of the ground state and ionization potential (*i.e.*, the difference between the energy of the neutral and cation) is minimized:[31]

$$J(\omega) = -\varepsilon_{HOMO}^{\omega} - \left(E_{gs}(\omega, N) - E_{gs}(\omega, N-1)\right). \qquad \textbf{(2.11)}$$

Typically, to establish consistency between the geometries and the IP-tuned ω-values, the geometry relaxation and the IP-tuning procedure were iterated in a self-consistent way. The IP-tuning guarantees that the HOMO of the ground state (ε_{HOMO}) is equivalent to the slope of the line between $E_{gs}(N)$ and $E_{gs}(N-1)$ (*i.e.*, the IP). This tuning procedure can be extended for the electron affinity (EA) by minimizing the difference between the EA and the HOMO of the anion (EA-tuning) or a simultaneous of IP and EA-tuning.

As discussed in the previous section, the main effect of the ω parameter is to control the length scale for range separation of the 1/r operator in the Hamiltonian. Typically, this parameter is empirically fit for a set of test molecules that leads to a typical ω values between 0.2 and 0.5 $bohr^{-1}$ in standard LRC functionals. A demonstration of how the 1/r operator changes between short-range and long-range functions is seen in Figure 2.4 (Adapted from Ref. 43).

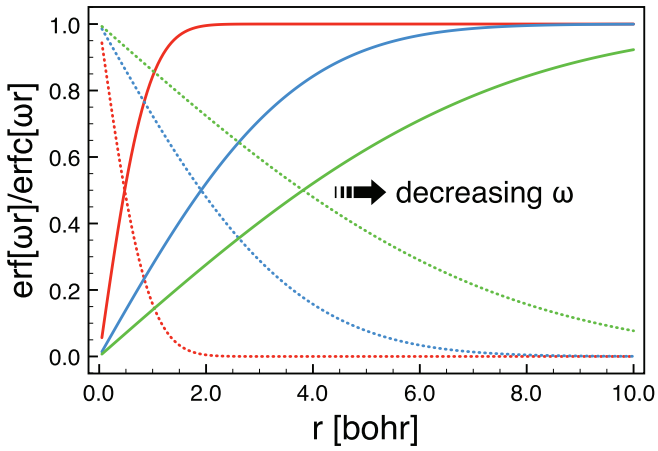

Figure 2.4. Plot of erf(ωr) (solid lines) and erfc(ωr) (dashed lines) where ω equal to 1.0 $bohr^{-1}$ (red), 0.25 $bohr^{-1}$ (blue), and 0.125 $bohr^{-1}$ (green). Adapted from Ref. 43.

A systems dependent parameter (*e.g.*, range-separation parameter) should also reflect the electron-electron correlation present in the molecular system. Indeed in previous work, we found that the tuning the ω is strongly dependent on the length-scales for electron correlation of the system, which was seen to play a major role in π-conjugated systems such as polyacetylene compared to saturated chains of the same length scale (Figure 2.5).[43] For polyacetylene, the IP-

tuned ω grew with system size n in almost an linear fashion for the lengths scales examined (n = 1 – 25); whereas, the tuned ω saturated after a few repeat units for an alkane chain.

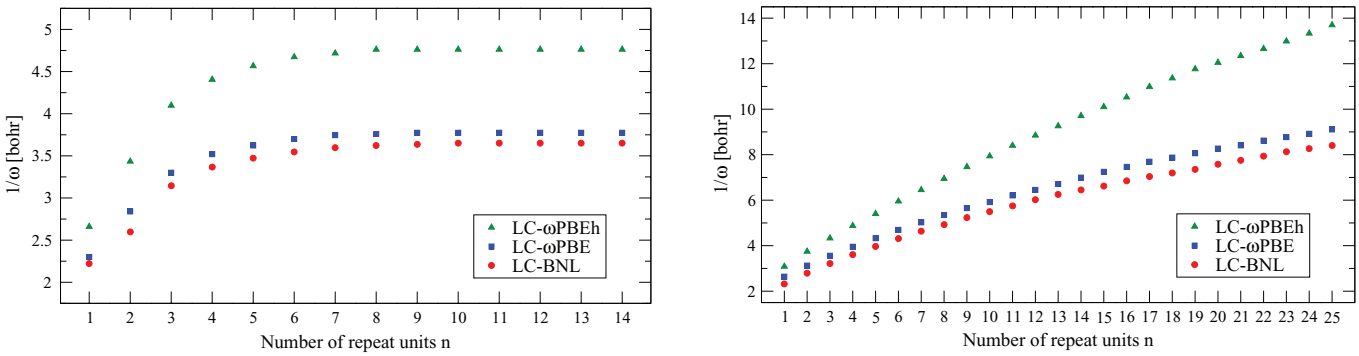

Figure 2.5. Evolution of the range separation parameter (ω) for three different tuned LRC functionals with number of repeat units for linear alkene ($C_{2n}H_{2n+2}$) and alkane ($C_{2n}H_{4n+2}$) chains. Adapted from Ref. 43.

2.2. Tight-Binding Hamiltonian

In the solid-state, the electrons are treated as a free-electron gas where the particles move freely in a high-ordered crystalline lattice. This allows for the wavefunction to be constructed in order to take advantage of the translational symmetry present in these periodic systems:

$$\psi(r) = Ae^{ikr} \qquad \textbf{(2.12)}$$

where *k* represents the electron wavevector and is related to the wavenumber for "waves" along the reciprocal lattice coming from a free electron having a velocity and momentum; the relationship between *k* and momentum comes from the de Broglie relationship $p = \lambda h$.

The wavefunction for each periodic lattice site can be generated from Bloch's Theorem to give:

$$\psi^k(r + a) = e^{ika}\psi^k(r) \qquad \textbf{(2.13)}$$

In a tight-binding Hamiltonian defined for a molecular crystal, a set of orbitals are constructed from the isolated molecules with one set of orbitals for each molecule (or site) in the elementary cell. For the set of these localized one-electron wave functions (of equal electron density at each lattice point), the translational symmetry for the set of basis functions can be employed to represent the wavefunction as a set of Bloch orbitals:

$$\psi_\alpha^k = \frac{1}{\sqrt{N}}\sum_T \phi_\alpha(r - T)e^{ikT} \qquad \textbf{(2.14)}$$

where T is an element of the direct lattice with unit vectors $\vec{a}$, $\vec{b}$, $\vec{c}$ through integers n:

$$T = n_a\vec{a} + n_b\vec{b} + n_c\vec{c} \qquad \textbf{(2.15)}$$

The matrix elements of the effective one-electron Hamiltonian give rises to on-site energies:

$$e_\alpha = \langle \psi_\alpha^k | H | \psi_\alpha^k \rangle \quad \textbf{(2.16)}$$

and off diagonal energies, which are the coupling elements between sites:

$$t_{\alpha\beta} = \langle \psi_\alpha^k | H | \psi_\beta^k \rangle \quad \textbf{(2.17)}$$

both terms can be rewritten as:

$$e_\alpha = A\left[e^{i2\pi x_a} + e^{-i2\pi x_a}\right] \quad \textbf{(2.18)}$$

$$t_{\alpha\beta} = B\left[1 + e^{i2\pi(x_a + x_b)}\right] + C\left[e^{i2\pi x_a} + e^{-i2\pi x_a}\right] \quad \textbf{(2.19)}$$

where the Hamiltonian eigenvalues are computed as:

$$E_{1/2}^k = e_\alpha \pm |t_{\alpha\beta}| \quad \textbf{(2.20)}$$

In a perfect crystal with the absences of any perturbations to the on-site energies, all e_α terms can be set to zero. Therefore, a relationship between the change in energy and the electronic coupling between sites is realized.

2.3. Band Structure

The evolution of energy with the reciprocal-space vector *k* gives the band structure (*i.e.*, band dispersion), where the bandwidth (*W*) of the material (particularly important for charge transport) is given by the change in energy at the band maximum (*e.g.*, $k = 0$) and minimum ($k = \frac{\pi}{2}$). Typically, band structures are computed along various high symmetry directions in the first Brillouin zone. The bandwidth (W) is related to the electronic coupling between sites; in the tight-binding approximation, $W = 2zt$, where z is number of nearest neighbors. For a 1-D system as an example, $z = 2$ and therefore $W = 4t$ with the band edge occurring at $\pm 2t$.

Energies obtained by diagonalizing the tight-binding Hamiltonian are used to construct the density of states (DOS), which gives information about the number of states available for particles at specific energy range.

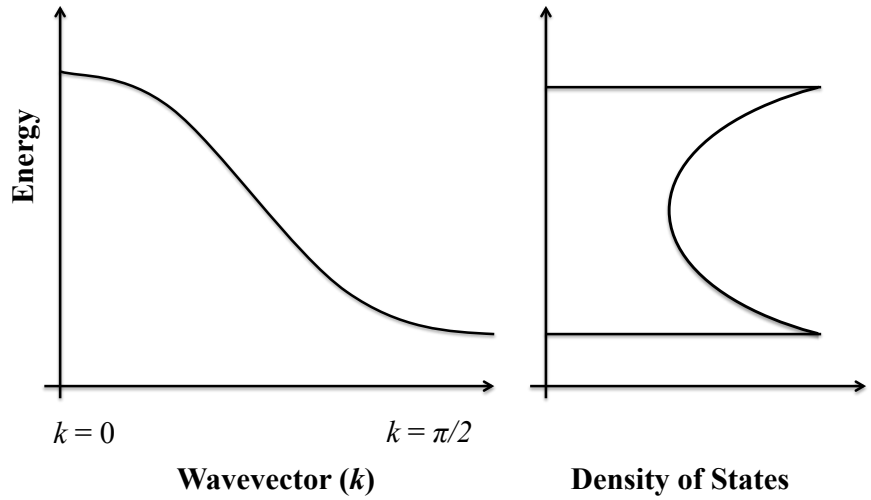

Figure 2.6. Illustration of a simple bandstructure and corresponding density of states (DOS). Adapted from Ref. 47.

2.4. Effective Mass

The band dispersion can also be related to the effective mass of a charge carrier by the given relationship:

$$\left(\frac{1}{m^*}\right)_{ij} = \frac{1}{\hbar^2}\frac{\partial^2 E_n(\vec{k})}{\partial k_i k_j}, \qquad \textbf{(2.21)}$$

where indices *i* and *j* denote reciprocal components, and $E_n(k)$ is dispersion relation for the *n*-th band and m^* is the effective mass of the carrier in the units of electron mass (m_0). The dispersion relation at the band minimum (or maximum) can be approximated to a parabola:

$$E_n(\vec{k}) = a_1 k_x^2 + a_2 k_y^2 + a_3 k_z^2 \,. \qquad \textbf{(2.22)}$$

Therefore, the components of the effective mass tensor are just the inverse of the coefficients in front of quadratic term:

$$m_{xx}^* = \frac{\hbar}{2a_1}\,;\; m_{yy}^* = \frac{\hbar}{2a_2};\; m_{zz}^* = \frac{\hbar}{2a_3}. \qquad \textbf{(2.23)}$$

However, in case of organic semiconductors, it is not always possible to fit dispersion to a quadratic polynomial. In this case, derivatives can be evaluated numerically, using the finite difference method, where the explicit form for the right-side symmetric tensor in Eq. (2.21)is:

$$\frac{\partial^2 E}{\partial k^2} = \begin{pmatrix} \frac{\partial^2 E}{\partial k_x^2} & \frac{\partial^2 E}{\partial k_y k_x} & \frac{\partial^2 E}{\partial k_z k_x} \\ \frac{\partial^2 E}{\partial k_x k_y} & \frac{\partial^2 E}{\partial k_y^2} & \frac{\partial^2 E}{\partial k_z k_y} \\ \frac{\partial^2 E}{\partial k_x k_z} & \frac{\partial^2 E}{\partial k_y k_z} & \frac{\partial^2 E}{\partial k_z^2} \end{pmatrix}, \qquad \textbf{(2.24)}$$

where second and mixed derivatives are evaluated on five-point stencil to give the effective mass components from the inverse of the eigenvalues and principal directions are eigenvectors of Eq. (2.25).

2.5. Transfer Integrals (Electronic Coupling)

For interacting molecules, M_A and M_B, the HOMO and LUMO levels of the single molecule are split by twice the intermolecular transfer integral (*i.e.*, $2t_{AB}$) in the dimer.[48-51] In the context of Koopman's theorem,[46] *i.e.*, the one-electron approximation, this can be written as:

$$t = \frac{(E_{H(L+1)} - E_{H-1(L)})}{2}, \quad \textbf{(2.25)}$$

where E is the orbital energy of the HOMO (LUMO+1) and HOMO-1 (LUMO) levels from the neutral closed shell configuration of the dimer M_A-M_B, assuming the HOMO and HOMO-1 of the dimer comes only from the HOMO orbitals of the monomers; that is, within this context dimer states can be expressed in terms of localized monomer orbital (*i.e.*, diabatic states, φ_A and φ_B) and t_{AB} can be approximated from the localized molecular orbitals for the closed shell configuration of the neutral ground state geometry of M_A (φ_A) and M_B (φ_B). [48,52]

$$t_{AB} = \langle \varphi_A | H | \varphi_B \rangle, \quad \textbf{(2.26)}$$

where the diabatic states (φ_A and φ_B) are the monomer HOMO (LUMO) orbitals for hole (electron) transport. The electronic Hamiltonian in the basis of monomer orbitals can be expressed as the matrix:

$$H = \begin{bmatrix} e_A & t_{BA} \\ t_{AB} & e_B \end{bmatrix}, \quad \textbf{(2.27)}$$

where the diagonal terms of this matrix are the site energies, expressed as:

$$e_{A/B} = \langle \varphi_{A/B} | H | \varphi_{A/B} \rangle, \quad \textbf{(2.28)}$$

and the orbital energies can be given by the secular equation:

$$\mathbf{HC} - \mathrm{E}\mathbf{SC} = 0, \qquad \textbf{(2.29)}$$

where S is the overlap matrix containing off-diagonal terms corresponding to the spatial overlap integral between the HOMO/LUMO of the two monomers.

It is worth pointing out that, while this new basis of monomer HOMOs/LUMOs is convenient for QM calculations, it can give rise to orthogonality issues, which has been discussed in detail previously.[48,49] Therefore, to generate an orthonormal basis that maintains the initial local character of the monomer orbitals, Löwdin's symmetric transformation[53] is applied to φ_{AB} so that the interaction energy for monomer HOMOs/LUMOs is:

$$\Delta E_{AB} = \sqrt{(e_A^{eff} - e_B^{eff})^2 + (2t_{AB}^{eff})^2}, \qquad \textbf{(2.30)}$$

where:

$$e_{A(B)}^{eff} = \frac{1}{2}\frac{(e_A + e_B) - 2t_{AB}S_{AB} \pm (e_A - e_B)\sqrt{1 - S_{AB}^2}}{1 - S_{AB}^2} \qquad \textbf{(2.31)}$$

$$t_{AB}^{eff} = \frac{t_{AB} - \frac{1}{2}(e_A + e_B)S_{AB}}{1 - S_{AB}^2} \qquad \textbf{(2.32)}$$

Thereby making $t_{H_{AB}}^{eff}$/ $t_{L_{AB}}^{eff}$ identical to *t* in the Marcus expression (discussed in Chapter 1).

Also, *t* invoked here is based on a two state model, which can be extended for systems where the HOMO and LUMO of the monomers are not energetically well separated from the HOMO-1 and LUMO+1, respectively.[54]

2.6. References

1. Hohenberg, P.; Kohn, W., Inhomogeneous Electron Gas. *Physical Review* **1964**, *136*, B864-B871.
2. Bright-Wilson, E., *Structural Chemistry and Molecular Biology* Freeman: San Francisco, 1968.
3. Kohn, W.; Sham, L. J., Self-Consistent Equations Including Exchange and Correlation Effects. *Physical Review* **1965**, *140*, A1133-A1138.
4. Slater, J. C., The Self-Consistent Field for Molecular and Solids, Quantum Theory of Molecular and Solids. McGraw-Hill: New York, 1974; Vol. 4.
5. Vosko, S. H.; Wilk, L.; Nusair, M., Accurate spin-dependent electron liquid correlation energies for local spin density calculations: a critical analysis. *Can. J. Phys.* **1980**, *58*, 1200-1211.
6. Dirac, P. A. M., Note on exchange phenomena in the Thomas-Fermi atom. *Proc. Cambridge Phil. Roy. Soc.* **1930**, *26*, 376-385.
7. Ceperley, D. M.; Alder, B. J., Ground State of the Electron Gas by a Stochastic Method. *Physical Review Letters* **1980**, *45*, 566-569.
8. Perdew, J. P.; Burke, K.; Ernzerhof, M., Generalized gradient approximation made simple. . *Physical Review Letters* **1996**, *77*, 3865-3868.
9. Perdew, J. P.; Burke, K.; Ernzerhof, M., Erratum: Generalized Gradient Approximation Made Simple. *Physical Review Letters* **1997**, *78*, 1396.
10. Perdew, J. P., Density-functional approximation for the correlation energy of the inhomogeneous electron gas. *Physical Review B* **1986**, *33*, 8822-24.
11. Becke, A. D., Density-functional exchange-energy approximation with correct asymptotic behavior. *Physical Review A* **1988**, *38*, 3098-3100.
12. Becke, A. D., A new mixing of Hartree--Fock and local density-functional theories. *The Journal of Chemical Physics* **1993**, *98*, 1372-1377.
13. Zhao, Y.; Truhlar, D. G., A new local density functional for main-group thermochemistry, transition metal bonding, thermochemical kinetics, and noncovalent interactions. *The Journal of Chemical Physics* **2006**, *125*, 194101.
14. Lee, C.; Yang, W.; Parr, R. G., Development of the Colle-Salvetti correlation-energy formula into a functional of the electron density. . *Physical Review B* **1988**, *37*, 785-789.
15. Becke, A. D., Density-functional thermochemistry. III. The role of exact exchange. *The Journal of Chemical Physics.* **1993**, *98*, 5648.
16. Adamo, C.; Barone, V., Toward reliable density functional methods without adjustable parameters: The PBE0 model. *The Journal of Chemical Physics* **1999**, *110*, 6158-6170.
17. Boese, A. D.; Martin, J. M. L., Development of Density Functionals for Thermochemical Kinetics. *The Journal of Chemical Physics.* **2004**, *121*, 3405-3416.
18. Zhao, Y.; Truhlar, D., The M06 suite of density functionals for main group thermochemistry, thermochemical kinetics, noncovalent interactions, excited states, and transition elements: two new functionals and systematic testing of four M06-class functionals and 12 other functionals. *Theoretical Chemistry Accounts: Theory, Computation, and Modeling (Theoretica Chimica Acta)* **2008**, *120*, 215-241.
19. Zhao, Y.; Truhlar, D. G., Comparative DFT Study of van der Waals Complexes: Rare-Gas Dimers, Alkaline-Earth Dimers, Zinc Dimer, and Zinc-Rare-Gas Dimers. *The Journal of Physical Chemistry A* **2006**, *110*, 5121-5129.

20. Zhao, Y.; Lynch, B. J.; Truhlar, D. G., Development and Assessment of a New Hybrid Density Functional Model for Thermochemical Kinetics. *The Journal of Physical Chemistry A* **2004**, *108*, 2715-2719.
21. Janesko, B. G.; Scuseria, G. E., Hartree--Fock orbitals significantly improve the reaction barrier heights predicted by semilocal density functionals. *The Journal of Chemical Physics* **2008**, *128*, 244112-4.
22. Muscat, J.; Wander, A.; Harrison, N. M., On the prediction of band gaps from hybrid functional theory. *Chemical Physics Letters* **2001**, *342*, 397-401;
23. Riley, K. E.; Op't Holt, B. T.; Merz, K. M., Critical Assessment of the Performance of Density Functional Methods for Several Atomic and Molecular Properties. *Journal of Chemical Theory and Computation* **2007**, *3*, 407-433.
24. Tozer, D. J.; Handy, N. C., Improving virtual Kohn--Sham orbitals and eigenvalues: Application to excitation energies and static polarizabilities. *The Journal of Chemical Physics* **1998**, *109*, 10180-10189.
25. Dreuw, A.; Head-Gordon, M., Failure of Time-Dependent Density Functional Theory for Long-Range Charge-Transfer Excited States: The Zincbacteriochlorin−Bacteriochlorin and Bacteriochlorophyll−Spheroidene Complexes. *Journal of the American Chemical Society* **2004**, *126*, 4007-4016.
26. Mori-Sánchez, P.; Cohen, A. J.; Yang, W., Localization and Delocalization Errors in Density Functional Theory and Implications for Band-Gap Prediction. *Physical Review Letters* **2008**, *100*, 146401.
27. Staroverov, V. N., Density-Functional Approximations for Exchange and Correlation. In *A Matter of Density*, John Wiley & Sons, Inc.: 2012; pp 125-156.
28. Yanai, T.; Tew, D. P.; Handy, N. C., A new hybrid exchange–correlation functional using the Coulomb-attenuating method (CAM-B3LYP). *Chemical Physics Letters* **2004**, *393*, 51-57;
29. Baer, R.; Neuhauser, D., Density Functional Theory with Correct Long-Range Asymptotic Behavior. *Physical Review Letters* **2005**, *94*, 043002.
30. Vydrov, O. A.; Heyd, J.; Krukau, A. V.; Scuseria, G. E., Importance of short-range versus long-range Hartree-Fock exchange for the performance of hybrid density functionals. *The Journal of Chemical Physics* **2006**, *125*, 074106-9.
31. Baer, R.; Livshits, E.; Salzner, U., Tuned Range-Separated Hybrids in Density Functional Theory. *Annual Review of Physical Chemistry* **2010**, *61*, 85-109.
32. Henderson, T. M.; Janesko, B. G.; Scuseria, G. E., Generalized gradient approximation model exchange holes for range-separated hybrids. *The Journal of Chemical Physics* **2008**, *128*, 194105-9.
33. Chai, J.-D.; Head-Gordon, M., Systematic optimization of long-range corrected hybrid density functionals. *The Journal of Chemical Physics* **2008**, *128*, 084106.
34. Chai, J. D.; Head-Gordon, M., Long-range corrected hybrid density functionals with damped atom-atom dispersion corrections. *Physical Chemistry Chemical Physics* **2008**, *10*, 6615-6620.
35. Tsuneda, T.; Kamiya, M.; Morinaga, N.; Hirao, K., A transversing connection between density functionals. *The Journal of Chemical Physics* **2001**, *114*, 6505-6513.
36. Livshits, E.; Baer, R., A well-tempered density functional theory of electrons in molecules. *Physical Chemistry Chemical Physics* **2007**, *9*, 2932-2941.

37. Kronik, L.; Stein, T.; Refaely-Abramson, S.; Baer, R., Excitation Gaps of Finite-Sized Systems from Optimally Tuned Range-Separated Hybrid Functionals. *Journal of Chemical Theory and Computation* **2012**, *8*, 1515-1531.
38. Ruzsinszky, A.; Perdew, J. P.; Csonka, G. I.; Vydrov, O. A.; Scuseria, G. E., Spurious fractional charge on dissociated atoms: Pervasive and resilient self-interaction error of common density functionals. *The Journal of Chemical Physics* **2006**, *125*, 194112-8.
39. Mori-Sánchez, P.; Cohen, A. J.; Yang, W., Many-electron self-interaction error in approximate density functionals. *The Journal of Chemical Physics* **2006**, *125*, 201102-4.
40. Perdew, J. P.; Parr, R. G.; Levy, M.; Balduz, J. L., Jr., Density-Functional Theory for Fractional Particle Number: Derivative Discontinuities of the Energy. *Physical Review Letters* **1982**, *49*, 1691-1694.
41. Janak, J. F., Proof that $\partial E/\partial ni = \varepsilon$ in density-functional theory. *Physical Review B* **1978**, *18*, 7165-7168.
42. Cohen, A. J.; Mori-Sánchez, P.; Yang, W., Challenges for Density Functional Theory. *Chemical Reviews* **2011**, *112*, 289-320.
43. Körzdörfer, T.; Sears, J. S.; Sutton, C.; Bredas, J. L., Long-range corrected hybrid functionals for pi-conjugated systems: Dependence of the range-separation parameter on conjugation length. *The Journal of Chemical Physics* **2011**, *135*, 204107-6.
44. Körzdörfer, T.; Parrish, R. M.; Sears, J. S.; Sherrill, C. D.; Bredas, J. L., On the relationship between bond-length alternation and many-electron self-interaction error. *The Journal of Chemical Physics* **2012**, *137*, 124305-8.
45. Körzdörfer, T.; Parrish, R. M.; Marom, N.; Sears, J. S.; Sherrill, C. D.; Bredas, J. L., Assessment of the performance of tuned range-separated hybrid density functionals in predicting accurate quasiparticle spectra. *Physical Review B* **2012**, *86*, 205110.
46. Koopmans, T., Über die Zuordnung von Wellenfunktionen und Eigenwerten zu den einzelnen Elektronen eines Atoms. *Physica* **1934**, *1*, 9.
47. Hoffmann, R., How Chemistry and Physics Meet in the Solid State. *Angewandte Chemie International Edition in English* **1987**, *26*, 846-878.
48. Valeev, E. F.; Coropceanu, V.; da Silva Filho, D. A.; Salman, S.; Bredas, J. L., Effect of Electronic Polarization on Charge-Transport Parameters in Molecular Organic Semiconductors. *Journal of the American Chemical Society* **2006**, *128*, 9882-9886.
49. Coropceanu, V.; Cornil, J.; da Silva Filho, D. A.; Olivier, Y.; Silbey, R.; Bredas, J. L., Charge Transport in Organic Semiconductors. *Chemical Reviews* **2007**, *107*, 926-952.
50. Senthilkumar, K.; Grozema, F. C.; Bickelhaupt, F. M.; Siebbeles, L. D. A., Charge transport in columnar stacked triphenylenes: Effects of conformational fluctuations on charge transfer integrals and site energies. *The Journal of Chemical Physics* **2003**, *119*, 9809-9817.
51. Newton, M. D., Quantum chemical probes of electron-transfer kinetics: the nature of donor-acceptor interactions. *Chemical Reviews* **1991**, *91*, 767-792.
52. Senthilkumar, K.; Grozema, F. C.; Guerra, C. F.; Bickelhaupt, F. M.; Lewis, F. D.; Berlin, Y. A.; Ratner, M. A.; Siebbeles, L. D. A., Absolute Rates of Hole Transfer in DNA. *Journal of the American Chemical Society* **2005**, *127*, 14894-14903.
53. Löwdin, P.-O., Quantum Theory of Many-Particle Systems. I. Physical Interpretations by Means of Density Matrices, Natural Spin-Orbitals, and Convergence Problems in the Method of Configurational Interaction. *Physical Review* **1955**, *97*, 1474-1489.

54. Li, H.; Bredas, J. L.; Lennartz, C., First-principles theoretical investigation of the electronic couplings in single crystals of phenanthroline-based organic semiconductors. *The Journal of Chemical Physics* **2007**, *126*, 164704.

Chapter 3 Accurate Description of Torsion Potentials in Conjugated Polymers Using Density Functionals with Reduced Self-Interaction Error.

3.1. Introduction

The electronic properties of π-conjugated systems are closely linked to their structural (geometric) properties.[1-3] One example for this close relationship is provided by the torsional flexibility of π-conjugated molecular chains, such as polyacetylene and polydiacetylene (Figure 3.1).[4-6] This flexibility can lead to a reduction in the effective conjugation length, thereby affecting important electronic properties such as band gaps,[7] ionization potentials/electron affinities,[8] and polarizabilities.[9] Also the rotational and torsional motions along the backbone play an important role in the photochromic and thermochromic properties.[10-12] Therefore, being able to predict accurate torsional barriers (as a way of quantifying the molecular flexibility) is useful for understanding many of the intrinsic properties of conjugated polymers; however, accurately describing these structural properties poses a fundamental challenge to current electronic-structure methods.

Density functional theory (DFT) is widely used for electronic-structure calculations on organic materials and many other systems of chemical interest because of its usually good compromise between computational cost and accuracy. However, inherent deficiencies in approximate Kohn–Sham exchange-correlation functionals can materialize as systematic errors in computed properties, and therefore, turn out to be problematic for describing certain electronic and structural properties. In the case of π-conjugated systems, a critical feature is the poor treatment

of electron delocalization by standard exchange-correlation functionals, which is typically related to spurious Coulombic self-repulsion, *i.e.*, the self-interaction error.[13-21] In line with what has been discussed by Yang and co-workers,[16,17,22] the delocalization error describes the physical consequence of poor density functional approximations (*i.e.*, the delocalization of the electronic structure to reduce the unphysical interactions of electrons with themselves). This effect is due to spuriously low energies for delocalized electrons, which results from the many-electron self-interaction error (MESIE);[18,2017,22,23] it is responsible for failures seen for DFT methods such as underestimation of reaction barriers,[24] band gaps of materials,[25,26] or charge-transfer excitation energies,[27-29] and overestimation of binding energies of charge-transfer complexes.[30] However, errors within various DFT methods can be due to the underlying approximations in the given functional and not just the MESIE. Here, we investigate a quantitative connection between the MESIE (computed through fractional particle curves as discussed in Refs. 16,23) and the overestimation of torsion barriers.

Previous studies have shown that even in the case of small, model conjugated systems such as 1,3-butadiene, a variety of DFT functionals lead to an overestimation of the torsional barrier.[31-37] For example, Karpfen *et al.* calculated that SVWN and B3LYP functionals overestimate the barriers for torsion along the central single bond of 1,3-butadiene by 1.5 – 2.7 kcal mol^{-1} when compared to MP2/6-31G(d).[38] Systematic self-interaction errors in the semilocal Perdew-Burke-Ernzerhof (PBE)[39,40] functional were previously seen to overestimate the computed barriers for oligodiacetyelenes.[41] Furthermore, and of particular interest to this study, it is not well understood how the functional-specific errors in the torsion barriers evolve with system size. Although a number of analyses have been performed on small molecules to date, larger systems

still need to be investigated to effectively elucidate the ability of DFT for describing π-conjugated systems at different length scales (*i.e.*, small molecule, oligomer, and polymer). We note that such a study proves to be challenging for most wave function-based methods due to their unfavorable scaling. However, in the context of torsional barriers, it was demonstrated that dual-basis density-fitting MP2 (DB-DFMP2) provides for a good trade-off between accuracy and computational cost, allowing for application to much larger oligomers compared to other, more accurate wave-function based methods.[41,42] Hence, although the DB-DFMP2 calculations do not provide a definitive benchmark for the torsion barriers, they do provide for a qualitatively and semi-quantitatively correct description at a computational cost that is still bearable for the large systems necessary for this study. As a criterion to categorize the reliability of different exchange-correlation functionals, we compare here the DFT results to DB-DFMP2 torsion barriers for a wide range of polyenes and oligodiacetylenes.

Our choice of functionals allows for the analysis of different semilocal approximations for exchange-correlation as well as the impact of the amount of HF exchange employed in the functional in the reduction of the MESIE. The magnitude of the delocalization error is then associated with the deviation of the DFT-calculated torsion barriers from the DB-DFMP2 results. We also analyze the dependency of the delocalization error on system size by evaluating the MESIE of each DFT method. We can thereby establish a quantitative relationship between the delocalization error and its influence on calculated structural properties in this case, torsion barriers.

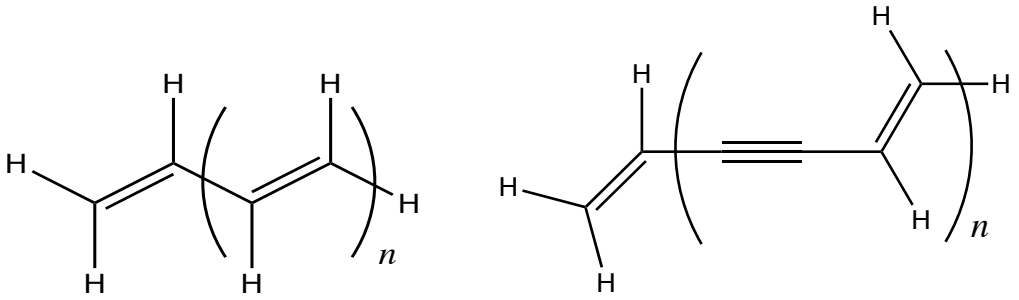

Figure 3.1. Molecular structure of the linear π-conjugated oligomers of polyacetylene and polydiacetylene considered in this study.

3.2. Methodology

All calculations were performed with the QChem 3.2/3.2.2/4.0.1/4.1 suite of computational chemistry packages.[43] For all DFT calculations, the Dunning correlation-consistent basis set aug-cc-pVDZ was used.[44] The basis set dependence of the torsion potentials for the n = 1 - 5 polyenes were also calculated using DB-DFMP2 at the cc-pVTZ level and showed a difference of at most ~ 0.1 kcal mol^{-1}; thus, in agreement with what has been previously discussed, no significant differences were found for the larger basis set.[41,42] For the (n = 1 – 14) polyenes, the potential energy surface was scanned by constraining the dihedral angle between the two center-most carbon–carbon double bonds while fully optimizing all other coordinates for each conformation. The dihedral angle (θ) was rotated stepwise in 12 increments from 0 – 180° (the cis- and trans-conformers correspond to 0 and 180°, respectively). Note that the 12 incremental changes in the dihedral angle were separated into two step sizes: six steps of 30° taken from 0 – 180° to map out the entire potential energy surface and six more steps of 5° from 90 – 120° to identify the torsion barrier. For all methods, the maximum is found to be between 95 – 105° and reported relative to the global minimum at a dihedral angle of 180°.

The potential energy surfaces in the (n = 1 – 10) oligodiacetylenes were evaluated in 30° increments from 0 – 180° around the central-most carbon-carbon triple and double bonds. The cis conformation (θ = 0°) was determined to be the global minimum; however, the trans conformation is nearly degenerate (θ = 180°) as it is destabilized by as little as 0.01 kcal mol^{-1} in some cases. For all methods used in this work, the maximum occurred at θ = 90°.

The torsion barriers for each value of n were extrapolated to the infinite polymer using the effective conjugation length model, which provides a measure for the length over which the π-electrons are delocalized:[45]

$$E(n) = E_\infty + (E_1 - E_\infty)e^{-A(n-1)}, \qquad \textbf{(3.1)}$$

where E_∞ is the torsion barrier for the infinite polymer, E_1 is the energy of the barrier for the smallest system, n is the number of monomer units as defined in Figure 3.1, and A is a fitting parameter describing the progression from n = 1 to the polymer limit. While the effective conjugation length model had originally been constructed from experimental results to quantify the saturation of the optical absorption energies with oligomer length, it was later also employed to describe the saturation point of torsional barriers with oligomer length.[41] The correlation between the computed barriers and the fitted values from Eq. (3.1) for the DB-DFMP2 results is shown in Table 3.1; the estimated effective conjugation length for each functional is provided in Table 3.2.

Table 3.1. DB-DFMP2/aug-cc-pVDZ computed torsional energy barrier for polyenes (left) and oligodiacetylenes (right) with the effective conjugation length (ECL) extrapolated fit, as a function of each repeat unit, *n*. All values in kcal mol^{-1}.

n	Computed Barrier	ECL Fit Values
1	6.39	6.31
2	7.20	7.42
3	8.38	8.25
4	8.87	8.87
5	9.44	9.34
6	9.71	9.69
7	9.96	9.95
8	10.02	10.15
9	10.29	10.30
10	10.38	10.41
11	10.47	10.49
12	10.54	10.55
13	10.65	10.60
14	10.68	10.64
15	10.70	--
16	10.67	--
17	10.69	--
18	10.70	--
19	10.71	--
∞	--	10.74

n	Computed Barrier	ECL Fit Values
1	0.63	0.58
2	0.96	1.11
3	1.50	1.41
4	1.60	1.58
5	1.72	1.68
6	1.75	1.74
7	1.77	1.78
8	1.78	1.79
9	1.79	1.81
10	1.79	1.81
11	1.79	--
∞	--	1.82

Table 3.2. Computed effective conjugation length from the saturation of the torsion barrier in number of repeat units (*n*) for polyenes and oligodiacetylenes.

Method	Effective Conjugation Length (*n*)	
	polyenes	oligodiacetylenes
DB-DFMP2	14	6
SVWN	19	11
BP86	19	10
PBE	19	10
PBE0	14	7
B3LYP	14	7
BMK	11-12	5
M06-L	19	9
M06	13	6
M06-2X	10	4-5
M06-HF	9	3
ωPBE	9	3
ωPBEh	8	4
ωB97	7	4
BNL	6	3
BOP	6-7	3

DB-DFMP2 geometry optimizations for all dihedral angles were performed with the restricted aug-cc-pVDZ (raug-cc-pVDZ) and auxiliary basis sets were used as recommended by the QChem authors.[43,46] The consideration of dual basis-set approaches combined with density fitting for the two-electron integrals has been shown to reduce the computational expense by 50% while maintaining the accuracy of the MP2 approach.[42,47-49] DB-DFMP2/aug-cc-pVDZ has provided reasonable accuracy at larger system sizes for π-conjugated systems such as oligodiacetylenes when compared to higher-level wave-function methods and basis sets (see discussion below).[41]

We have employed a set of exchange-correlation functionals representing the most commonly used classes of DFT functionals: The (semi)local functionals include the local density approximation (LDA) using the parameterization of Vosko, Wilk and Nusair (VWN),[50-53] the generalized gradient approximations (GGAs) by Perdew, Burke, and Ernzerhof (PBE)[39,40] and Becke and Perdew (BP86),[54,55] and a pure meta-GGA functional from the set of Minnesota-functionals (M06-L).[56] In an attempt to understand the influence of HF exchange on the calculated torsion barriers, we also considered a carefully chosen set of hybrid functionals. The standard hybrid-GGA functionals B3LYP[57,58] and PBE0[59] contain 20% and 25% HF-exchange, respectively. The hybrid meta-GGA functionals analyzed here were BMK[60] and the family of Minnesota-functionals: M06,[61] M06-2X,[61] and M06-HF.[62] We note that M06-L, M06, BMK, M06-2X, and M06-HF have 0%, 27%, 42%, 54%, and 100% HF exchange, respectively. Finally, we studied a set of long-range-corrected (LRC) functionals, *i.e.*, ωPBE, ωPBEh,[63] ωB97,[64] ωB97X,[64] ωB97X-D,[65] BOP,[66] and BNL.[67,68] The computed torsion barriers for each functional

at each *n* chain length of the polyenes and oligodiacetylenes are provided in Table 3.3 − Table 3.8.

Table 3.3. Computed torsional energy barrier in polyenes for various (semi)local or hybrid DFT functionals as a function of repeat unit, *n*. All values in kcal mol^{-1}.

n	SVWN	BP86	PBE	PBE0	B3LYP	BMK	M06-L	M06	M06-2X	M06-HF
1	7.97	7.67	7.69	7.17	7.32	6.96	7.86	7.03	6.54	5.65
2	9.19	8.88	8.90	8.15	8.31	7.70	9.15	7.96	7.23	6.01
3	10.99	10.63	10.67	9.52	9.70	8.76	10.97	9.22	8.17	6.55
4	11.77	11.37	11.43	10.04	10.23	9.13	11.73	9.71	8.52	6.74
5	12.71	12.25	12.32	10.66	10.91	9.58	12.63	10.26	8.90	6.93
6	13.21	12.70	12.79	10.95	11.16	9.76	13.09	10.52	9.05	7.00
7	13.74	13.21	13.30	11.26	11.49	9.96	13.58	10.77	9.20	7.04
8	14.07	13.49	13.59	11.43	11.66	10.04	13.88	10.92	9.26	7.06
9	14.40	13.82	13.92	11.60	11.84	10.14	14.18	11.06	9.32	7.07
10	14.62	14.01	14.17	11.69	11.93	10.17	14.38	11.15	9.36	7.08
11	14.85	14.25	14.39	11.79	12.05	10.22	14.56	11.21	9.39	7.08
12	15.02	14.39	14.55	11.90	12.10	10.23	14.71	11.29	9.41	7.10
13	15.22	14.68	14.72	11.97	12.19	10.26	14.86	11.35	9.44	7.12
14	15.31	14.80	14.83	11.99	12.21	10.28	14.95	11.39	9.47	7.11

Table 3.4. Computed torsional energy barriers in polyenes for various long-range corrected DFT functionals using default ω values (given in $bohr^{-1}$), as a function of repeat unit, *n*. All values in kcal mol^{-1}.

n	ωPBE (0.400)	ωPBEh (0.200)	ωB97 (0.400)	BNL (0.500)	BOP (0.400)
1	5.56	5.95	5.71	5.57	5.64
2	6.04	6.49	6.15	5.99	6.15
3	6.69	7.24	6.78	6.57	6.81
4	6.88	7.46	6.96	6.73	7.00
5	7.10	7.72	7.16	6.91	7.21
6	7.16	7.81	7.21	6.96	7.27
7	7.22	7.92	7.27	7.01	7.34
8	7.24	7.94	7.27	7.01	7.35
9	7.26	7.98	7.28	7.03	7.33
10	7.26	7.99	7.27	7.03	7.33
11	7.26	8.00	7.28	7.03	7.33
12	7.27	7.99	7.28	7.03	7.33
13	7.28	7.98	7.30	7.02	7.34
14	7.26	7.98	7.28	7.01	7.33

Table 3.5. Computed torsional energy barriers in polyenes for IP-tuned long-range corrected hybrid DFT functionals as a function of repeat unit, *n*. Torsional barriers (T.B.) in kcal mol^{-1} and ω values in $bohr^{-1}$.

n	ωPBE		ωPBEh		ωB97		BNL		BOP	
	T.B.	ω	T.B.	ω	T.B.	ω	T.B.	ω	T.B.	ω
1	5.63	0.320	5.91	0.267	5.71	0.323	5.54	0.358	5.76	0.341
2	6.28	0.281	6.64	0.231	6.28	0.283	6.09	0.311	6.38	0.297
3	7.20	0.253	7.63	0.205	7.12	0.254	6.89	0.277	7.27	0.265
4	7.64	0.231	8.10	0.185	7.51	0.232	7.29	0.252	7.70	0.241
5	8.15	0.213	8.63	0.169	7.97	0.215	7.77	0.232	8.19	0.223
6	8.47	0.199	8.96	0.156	8.23	0.200	8.06	0.216	8.50	0.207
7	8.80	0.187	9.29	0.145	8.50	0.188	8.36	0.203	8.81	0.195
8	9.05	0.177	9.52	0.136	8.68	0.179	8.61	0.191	9.06	0.184
9	9.28	0.169	9.75	0.128	8.87	0.17	8.83	0.182	9.30	0.175
10	9.49	0.161	9.94	0.121	8.93	0.163	9.01	0.174	9.48	0.167
11	9.65	0.155	10.11	0.115	9.35	0.156	9.21	0.166	9.64	0.161
12	9.82	0.149	10.26	0.110	9.38	0.150	9.38	0.160	9.79	0.155
13	10.01	0.144	10.41	0.105	9.53	0.143	9.52	0.155	9.99	0.149
14	10.12	0.140	10.53	0.101	9.59	0.139	9.60	0.151	10.09	0.145

Table 3.6. Computed torsional energy barriers in oligodiacetylenes for various (semi)local and hybrid DFT functionals as a function of repeat unit, *n*. All values in kcal mol^{-1}.

n	SVWN	BP86	PBE	PBE0	B3LYP	BMK	M06-L	M06	M06-2X	M06-HF
1	1.06	1.07	1.06	0.89	0.89	0.71	0.99	0.73	0.66	0.48
2	1.75	1.71	1.73	1.35	1.36	1.03	1.60	1.10	0.94	0.63
3	3.02	2.90	2.92	2.10	2.14	1.60	2.68	1.71	1.36	0.81
4	3.38	3.22	3.24	2.25	2.31	1.67	2.95	1.83	1.41	0.83
5	3.81	3.60	3.63	2.43	2.50	1.75	3.22	1.96	1.49	0.84
6	3.98	3.73	3.78	2.48	2.56	1.78	3.33	1.99	1.50	0.84
7	4.15	3.88	3.95	2.53	2.61	1.81	3.50	2.01	1.51	0.84
8	4.25	3.93	4.03	2.53	2.62	1.81	3.56	1.97	1.50	0.84
9	4.35	3.99	4.06	2.54	2.62	1.88	3.60	2.02	1.50	0.84
10	4.41	4.00	4.10	2.55	2.61	1.81	3.71	2.04	1.49	0.84

Table 3.7. Computed torsional energy barrier in kcal mol^{-1} in oligodiacetylene for various long-range corrected DFT functionals as a function of repeat unit, *n*, using the default ω values (in $bohr^{-1}$).

n	ωPBE (0.400)	ωPBEh (0.200)	ωB97 (0.400)	BNL (0.500)	BOP (0.400)
1	0.45	0.59	0.48	0.42	0.43
2	0.61	0.83	0.63	0.56	0.59
3	0.83	1.18	0.88	0.75	0.81
4	0.86	1.23	0.90	0.77	0.82
5	0.86	1.27	0.93	0.78	0.83
6	0.86	1.28	0.93	0.78	0.84
7	0.86	1.29	0.95	0.78	0.83
8	0.86	1.29	0.95	0.77	0.82
9	0.86	1.28	0.95	0.78	0.80
10	0.86	1.29	0.95	0.73	0.82

Table 3.8. Computed torsional energy barriers in oligodiacetylenes for IP-optimized long-range corrected hybrid DFT functionals as a function of repeat unit, *n*. Torsional barriers (T.B.) in kcal mol^{-1} and ω values in $bohr^{-1}$.

n	ωPBE		ωPBEh		ωB97		BNL		BOP	
	T.B.	ω	T.B.	ω	T.B.	ω	T.B.	ω	T.B.	ω
1	0.49	0.292	0.54	0.245	0.53	0.299	0.46	0.326	0.47	0.312
2	0.75	0.248	0.78	0.198	0.79	0.247	0.71	0.268	0.73	0.257
3	1.41	0.205	1.38	0.170	1.21	0.222	1.13	0.232	1.18	0.223
4	1.46	0.181	1.45	0.150	1.38	0.194	1.28	0.208	1.31	0.200
5	1.56	0.172	1.61	0.137	1.53	0.179	1.44	0.191	1.45	0.185
6	1.58	0.169	1.69	0.127	1.62	0.168	1.54	0.178	1.55	0.173
7	1.66	0.161	1.77	0.120	1.71	0.160	1.63	0.169	1.62	0.165
8	1.72	0.155	1.85	0.115	1.76	0.155	1.69	0.162	1.68	0.158
9	1.76	0.151	1.85	0.112	1.82	0.150	1.70	0.157	1.72	0.154
10	1.79	0.148	1.85	0.110	1.84	0.148	1.76	0.154	1.76	0.152

Following the work of Savin and Flad,[69] LRC functionals partition the electron-electron Coulomb operator into a short-range domain and a long-range domain through the use of Eq. (2.10). In a recent work, we found that the optimal range-separation parameter ω in molecular chains, determined by non-empirical tuning to match the IP (ionization potential)-theorem,[70] strongly depends on the conjugation length of the molecules under study.[71] Furthermore, earlier studies showed that the MESIE is typically reduced by several orders of magnitude compared to standard DFT methods when combining the LRC-hybrids with the IP-tuning procedure.[72-77] These results indicate that the range-separation parameter has a decisive influence on the delocalization error and, presumably, on the calculated torsion barriers. Therefore, we have not only employed the LRC-hybrids with their standard range-separation parameter values but also with the tuned ω values. We recall that the IP-tuning procedure[78] minimizes the difference between the HOMO eigenvalue of the ground state and the ionization potential (*i.e.*, the difference between the energies of the neutral and cation states), thereby leading to a significant reduction in delocalization error.[72-77] The tuning procedure was done prior to optimization for the trans ($\theta = 180°$) geometry and that ω value was then used for the optimization of the entire potential energy surface. Although a change in the tuned ω value with the torsion angle was noted in a previous study, here, we fix the ω value to its tuned value for the trans geometry. This is necessary to make a consistent comparison of the energies for the various torsion barriers. Changing ω along the torsion would change the underlying functional and, thus, eliminate the ability for a relative comparison of the energies at each torsion angle.

To understand the origin of the failures of standard DFT approaches in computing the torsion potentials of polyenes and oligodiacetylenes, it is useful that the definition of the MESIE[16,23]

relates the delocalization error with a property of the exact exchange-correlation functional: The exact total energy as a function of fractional occupation must correspond to a series of straight lines with kinks at integer occupations as demonstrated in a seminal work by Perdew and co-workers.[79] Hence, any deviation of the energy for fractional charges from the exact linear condition is due to an error in the approximation to the exchange-correlation functional, referred to as the MESIE. Semilocal DFT functionals yield a convex curve for energy vs. fractional occupation, which means that they spuriously favor delocalized over localized charges. On the other hand, HF theory shows a concave total energy curve, related to a localization error. Hence, the amount of HF exchange in a given hybrid functional is crucial for its treatment of electron delocalization.

Here, we quantify the MESIE by calculating the total energy curve for fractional particle numbers when going from the neutral molecule to the cation in the optimized neutral geometries (discussed in detail below). Fractional particle curves for the evaluation of the MESIE were performed in a local developers' version of PSI4[80] using the geometries obtained from SVWN, PBE, PBE0, and standard and IP-tuned ωPBE and ωPBEh; the cc-pVDZ basis set was used in the MESIE analysis. A comparison with jun-cc-pVDZ was also made and the calculated MESIE values only differed by ca. 0.05 kcal mol^{-1}.

3.3. Results and Discussion

3.3.1. Results for DB-DFMP2-Computed Torsion Potentials

In order to assess the quality of our benchmark data, we start with an analysis of the DB-DFMP2 results compared with experimental results obtained with Raman spectroscopy and high-level calculations performed on polyenes for the smallest *n* values. The DB-DFMP2 barrier changes by 4.25 kcal mol^{-1} from *n* = 1 to 14 (see Figure 3.2). The largest increase in the torsion barrier (0.81 kcal mol^{-1}) is seen between *n* = 3 – 4. For oligomers longer than *n* = 8, the barrier slowly converges to its final value, showing steps of *ca.* 0.1 kcal mol^{-1} and decreasing between *n* = 9 and 14. Note that only for *n* = 1 – 3 was a cis-gauche–barrier–trans motif seen in previously published results (see Ref. 81).

For the smallest polyenes (*n* = 1, *i.e.*, butadiene, see Table 3.9), the accuracy of DB-DFMP2/aug-cc-pVDZ for energies and geometries can be compared to other high-level wave-function methods used previously in the literature. Recent state-of-the-art wave-function calculations benchmarked the transition barrier to be 6.12 kcal mol^{-1} ($\theta = 101°$)[82] at the [MP2(FC)/cc-pV5Z + CCSD(T)(FC)/cc-pVTZ] level and 6.40 kcal mol^{-1} ($\theta = 101.7°$)[81] at the [CCSD(T)(FC)/CBS + CCSD(T)(CV)/cc-pwCVQZ + SR correction + CCSDT(Q)(FC)/cc-pVDZ correction] level. These results compare well with the torsional barrier identified by our constrained optimization procedure, where we fixed the dihedral angle to be $\theta = 100°$. In addition, it should be noted that our potential energy surface scan coincides well with the values benchmarked by the high-level CCSD(T) calculations and Raman spectroscopy both in terms of angle and computed relative energy; the computed energies provide for an adequate comparison within *ca.* 0.5 kcal mol^{-1} above the [CCSD(T)(FC)/CBS + CCSD(T)(CV)/cc-pwCVQZ + SR correction +

CCSDT(Q)(FC)/cc-pVDZ correction] reference for all dihedral angles (*i.e.*, consistently overestimating the energy for all torsions).

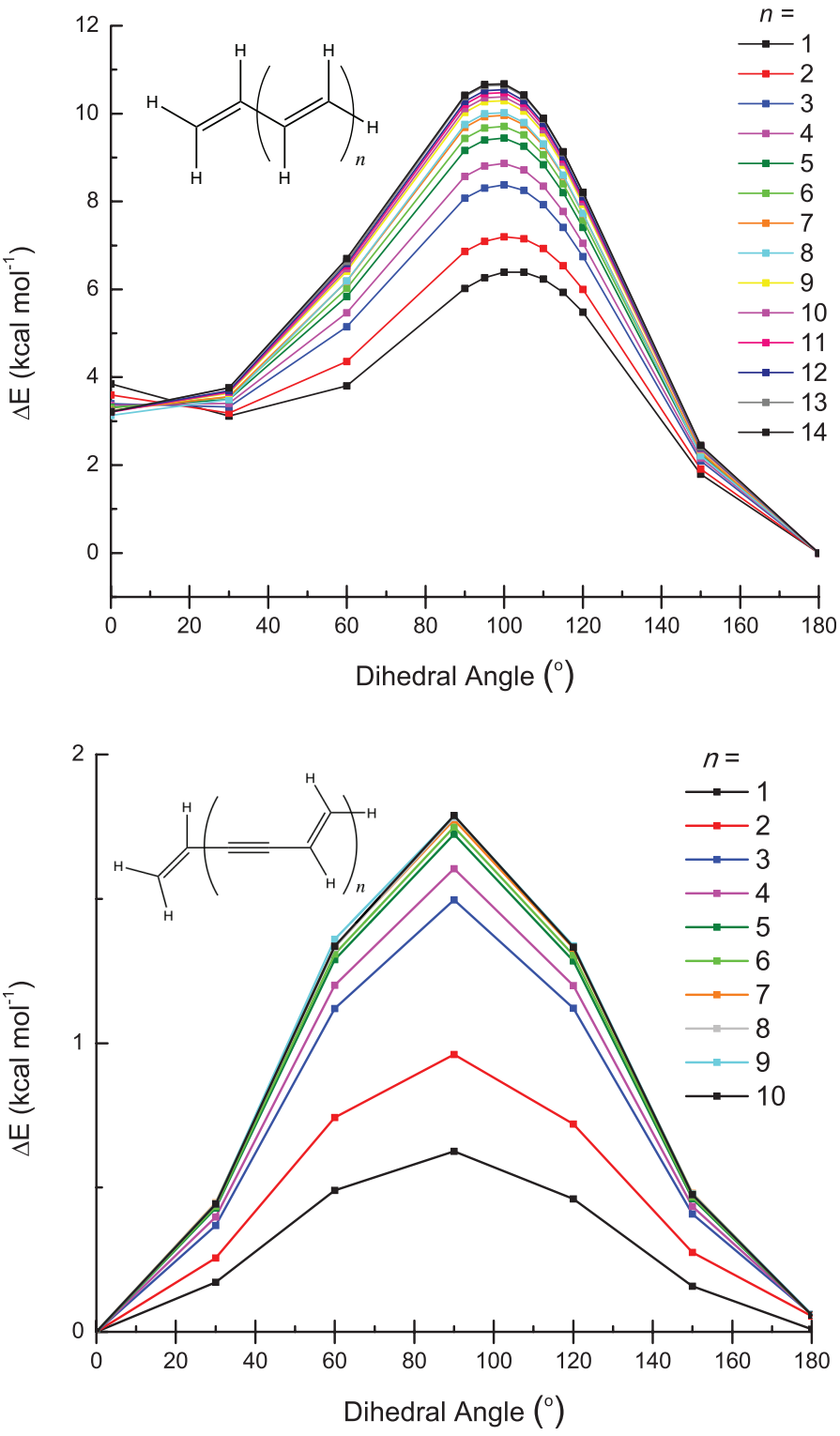

Figure 3.2. Evolution of the torsional potential in polyenes (top) and oligodiacetylenes (bottom) with the number of repeat units, *n*, at the DB-DFMP2/aug-cc-pVDZ level.

Table 3.9. Comparison of the calculated total energies for butadiene (n = 1) relative to the trans planar conformation with literature values (dihedral angles, θ, are reported in parentheses). Energies are reported in kcal mol^{-1}.

	Energies[a] (θ)	Energies[b] (θ)	Energies[c] (θ)	Energies[d] (θ)
Trans	0 (180)	0 (180)	0 (180)	0 (180)
Torsion Barrier	6.40 (101.7)	6.12 (101)	5.97 (103)	6.39 (100)
90°	6.16 (90)	5.85 (90)	5.52 (90)	6.02 (90)
Gauche	3.01 (35.5)	2.89 (35)	2.87 (38)	3.12 (30)
Cis	3.49 (0)	3.47 (0)	3.94 (0)	3.84 (0)

a) CCSD(T)(FC)/CBS + CCSD(T)(CV)/cc-pwCVQZ + SR correction + CCSDT(Q)(FC)/cc-pVDZ correction Ref. 81
b) MP2(FC)/cc-pV5Z + CCSD(T)(FC)/cc-pVTZ Ref. 82
c) Gas-phase Raman Ref. 83
d) DB-DFMP2/aug-cc-pVDZ, this work

The potential energy surfaces for oligodiacetylenes is seen to vary only between 0.5 and 1.8 kcal mol^{-1} over the entire range of n studied (Figure 3.2). The ability of DB-DFMP2/aug-cc-pVDZ to produce quantitatively correct torsion potentials for oligodiacetylenes with n = 1, 2 was discussed in detail previously.[41] It is reasonable to assume that DB-DFMP2 will produce qualitatively and at least semi-quantitatively correct torsion barriers also for longer oligodiacetylenes. With a reliable and semi-quantitative method available for computing torsion barriers for long polyenes and oligodiacetylenes, we can now start analyzing the performance of the various DFT functionals.

3.3.2. Torsion Potentials Computed with Standard DFT

The interplay between the various semilocal approximations to exchange and correlation and the amount of HF exchange employed in the various functionals used to calculate the torsional barriers for polyenes and oligodiacetylenes is illustrated in Figure 3.3 in comparison to the DB-DFMP2 barriers. The torsion barriers for the individual chain lengths are fitted using the effective conjugation length model given in Eq. (3.1) (lines) and extrapolated to the polymer limit. For polyenes, the torsional potentials for all of the functionals agree qualitatively: The most stable conformation is the trans form at 180° and the barrier occurs at approximately 100°. The relative magnitude of the barrier, however, differs by as much as 0.2 to 5 kcal mol^{-1} among the various methods. Qualitatively similar results are obtained for the oligodiacetylenes, for which the relative magnitude of the barrier differs by 0.01 – 2.6 kcal mol^{-1} among the different functionals.

It is expected that with a large self-interaction error, the effective conjugation length would be overestimated due to an over-delocalization of the electronic structure, thereby overestimating the torsional barrier. Larger oligomers were calculated to ensure that a saturation of the effective conjugation length had in fact been reached up to n = 19 for polyenes and n = 11 for oligodiacetylenes; see Table 3.1. The effective conjugation length is assigned for each of the functionals for polyenes and oligodiacetylenes (defined here as the point at which the torsion barrier changes by less than 0.1 kcal mol^{-1}). Using the DB-DFMP2 results, an effective conjugation length of n = 14 and n = 6 is obtained for polyenes and oligodiacetylenes, respectively. These results are qualitatively consistent with the computed torsional barriers: SVWN (15.5 kcal mol^{-1}) and the GGAs BP86 (14.7 kcal mol^{-1}) and PBE (14.8 kcal mol^{-1})

dramatically overestimate the torsional barrier in polyenes by a similar amount of 4.2 – 4.8 kcal mol^{-1} relative to the DB-DFMP2 (10.7 kcal mol^{-1}) result. For oligodiacetylenes, SVWN (4.55 kcal mol^{-1}), BP86 (4.13 kcal mol^{-1}), and PBE (4.23 kcal mol^{-1}) overestimate the torsional barrier by 2.7 – 2.3 kcal mol^{-1} relative to the DB-DFMP2 (1.82 kcal mol^{-1}) result. These findings are consistent with previously published results for these functionals.[33] It is worth noting that the error in the computed torsion barriers when compared to the DB-DFMP2 results increases with system size, leading to a larger *n* calculated for the effective conjugation length. As a consequence of the purely (semi)local treatment of exchange and correlation, the torsional barriers calculated from LDA and GGAs actually grow almost linearly with the number of repeat units, revealing a qualitatively wrong description of the effective conjugation length.

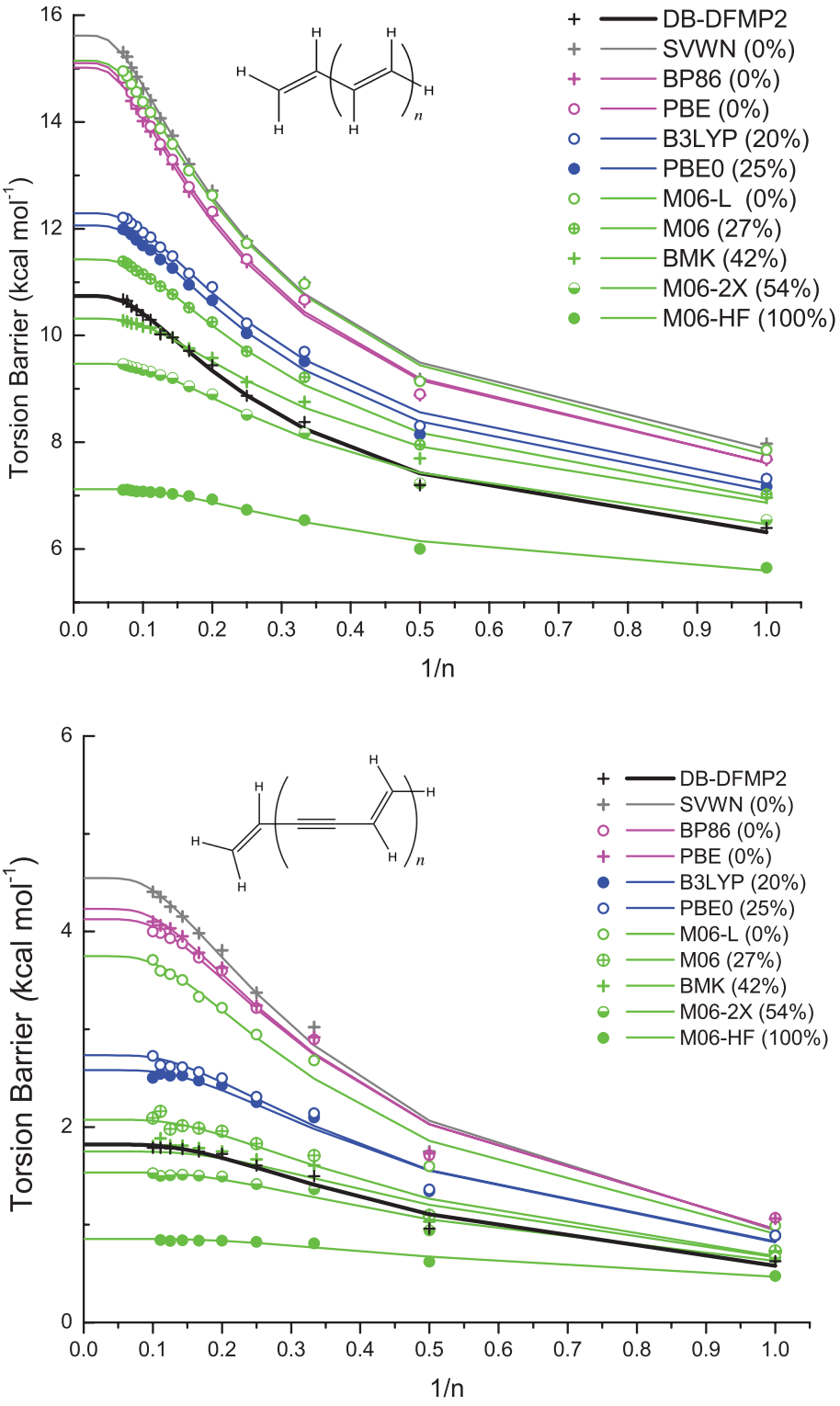

Figure 3.3. Evolution of the computed torsional energy barriers in polyenes (top) and oligodiacetylene (bottom) for a variety of DFT methods as a function of the inverse number of repeat units, *n*. The results for the torsion barriers are fitted using the effective conjugation length model of Eq. **(3.1)** and extrapolated to the polymer limit (solid lines).

In an attempt to quantitatively connect the error in the torsion potentials to the delocalization error, we calculated the MESIE for the n = 14 polyene using geometries obtained from various functionals. This is illustrated in Figure 3.4, where δ denotes the deviation in fractional number of electrons from the neutral molecule. As the non-linearity of the approximate fractional particle curves can be hard to gauge with the naked eye, the deviation from linearity of the total energy ΔE(δ) is shown in the inset of Figure 3.4. The integral $e_{MESIE} = \int_{-1}^{0} \Delta E(\delta) d\delta$ quantifies the MESIE upon ionization of the molecule. A negative [positive] e_{MESIE} indicates a delocalization [localization] error.[17] The delocalization error for both SVWN and PBE is estimated to be -4.2 kcal mol^{-1} for the n = 14 polyene and -3.5 kcal mol^{-1} for the n = 10 oligodiacetylene. It is very instructive to note that the MESIEs calculated for different torsional angles of 0°, 100°, and 180° are identical within 0.05 kcal mol^{-1}, indicating that with purely semilocal functionals the torsion does not break the conjugation.

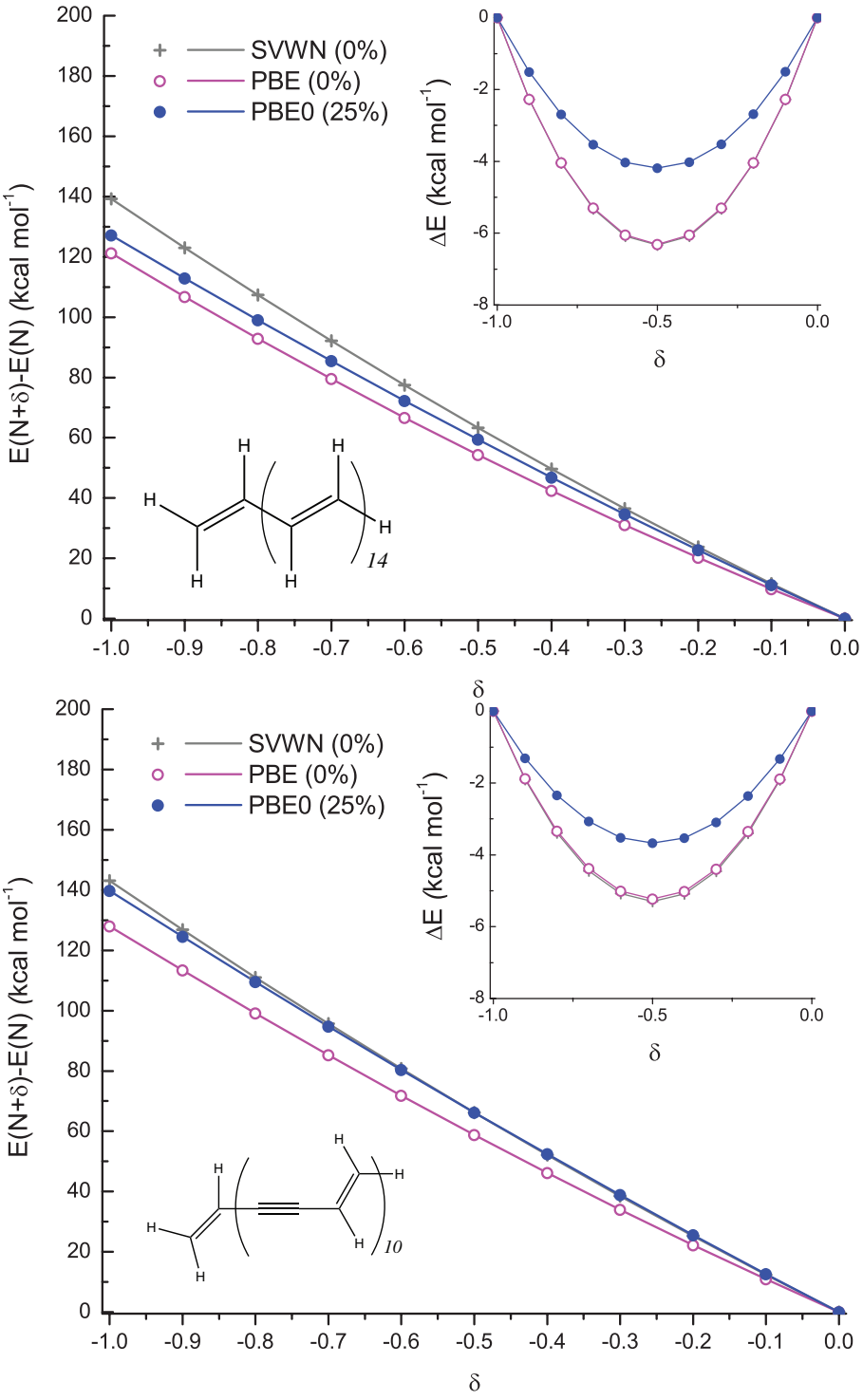

Figure 3.4. Change in relative energy for the n = 14 polyene (top) and the n = 10 oligodiacetylene (bottom) as a function of fractional occupation number when going from the neutral molecule (δ = 0) to the cation (δ = -1) for SVWN (grey), PBE (pink), and PBE0 (blue) using the respective optimized neutral geometries. The inset shows the deviation of relative energy from a straight line connecting the end points δ = 0 and δ = -1.

Hybrid functionals that incorporate a percentage of HF exchange are seen to improve both the computed effective conjugation length and MESIE. The hybrid functionals PBE0 (12.1 kcal mol^{-1}) and B3LYP (12.3 kcal mol^{-1}) overestimate the torsional barriers by +1.4 and +1.7 kcal mol^{-1} relative to the calculated DB-DFMP2, respectively; this corresponds to an error reduction by 2.5 – 3.2 kcal mol^{-1} as compared to LDA and GGAs. These results are consistent with a previous comparison of MP2/6-31G(d), B3LYP, and SVWN in computing the torsional barrier for 1,3-butadiene, which showed that SVWN and B3LYP overestimated the barrier by 2.7 and 1.6 kcal mol^{-1}, respectively.[38] Also, the oligodiacetylene results demonstrate a similar improvement with HF exchange, with the error in the calculated torsional potentials decreasing to 2.6 kcal mol^{-1} and 2.7 kcal mol^{-1} for PEB0 and B3LYP, respectively; however, these methods still give barriers that are +0.76 and +0.86 kcal mol^{-1} larger than the DB-DFMP2 barriers, respectively. Importantly, the effective conjugation length fit for the hybrid functionals matches the shape of the DB-DFMP2 trend for both polyenes and oligodiacetylenes with increasing system size, demonstrating the important role that HF exchange has in reducing the error over a range of system sizes. However, seemingly a too small fraction of HF exchange is included in these standard hybrid functionals for an accurate description of the torsion barriers in long polyenes and oligodiacetylenes. As demonstrated for the PBE0 functional in Figure 3.4, the improvement in the torsion barriers is a manifestation of the reduction in MESIE, which is computed to be -2.80 kcal mol^{-1} for the n = 14 polyene and -2.45 kcal mol^{-1} for the n = 10 oligodiacetylene.

To further understand the improved accuracy seen with the hybrid functionals over the LDA and GGA functionals, a mixture of hybrid and nonhybrid meta-GGA functionals were used to examine if the improvement in torsion barriers can be directly attributed to the amount of HF

exchange. In general, the torsion barriers decrease with increasing amount of HF exchange employed in the functional, as seen in Figure 3.3. The meta-GGA functionals were the closest to reproducing the DB-DFMP2 projected polymer-limit value for polyenes [oligodiacetylenes] with BMK, M06, and M06-2X differing by -0.42 [-0.10], +0.68 [+0.25], and -1.27 [-0.29] kcal mol^{-1}; however, disparate results were seen in the performance of these functionals based primarily on the amount of HF exchange. For polyenes, the BMK functional is found to perform best at larger oligomer lengths resulting in the most accurate value relative to DB-DFMP2 at the polymer limit; M06-2X almost exactly replicates the DB-DFMP2 values up to $n = 4$, then starts to diverge to about 1 kcal mol^{-1} at the polymer limit, indicating that the performance of a functional over a variety of oligomer lengths is directly dependent on the amount of HF exchange within a given method. This effect is also seen in the torsion barrier obtained for the non-hybrid meta-GGA functional M06-L (15.1 kcal mol^{-1}), which overestimates the barrier projected to the polymer limit by 4.4 kcal mol^{-1} relative to the DB-DFMP2 result (10.7 kcal mol^{-1}). Similarly to LDA and the GGAs, this is attributed to a large delocalization error. Conversely, the lowest barrier for polyenes was obtained at the polymer limit using the M06-HF functional (7.1 kcal mol^{-1}), i.e., 3.6 kcal mol^{-1} below the DB-DFMP2 result. This indicates a severe localization error that grows with system size and becomes increasingly apparent for longer oligomers. With the M06-HF functional employing 100% HF exchange, the strong localization error can be anticipated.

In summary of the results shown in Figure 3.3, it is apparent that the HF exchange plays a dominant role over any semilocal approximations to exchange-correlation in determining the torsional barriers in long oligomers. Of course, in the light of the close connection among torsional barriers, conjugation length, and delocalization error, this finding is by no means

surprising. Next, we study how the reduction in delocalization error by using non-empirically tuned long-range corrected hybrid functionals helps find a reliable description of the torsion barriers in molecular chains irrespective of their size and effective conjugation length.

3.3.3. Torsion Potentials Computed with IP-Tuned DFT

A variety of LRC-DFT functionals using default ω values were tested first. They all underestimate the calculated torsional barriers by 2.7 – 3.6 kcal mol^{-1} for the n = 14 polyene and 0.52 – 1.0 kcal mol^{-1} for the n = 10 oligodiacetylene (Figure 3.5). This indicates that the treatment of electron delocalization is too HF-like in long π-conjugated oligomers. That is, for LRC-DFT functionals, the standard pre-defined ω values, which have typically been determined empirically for small and medium-sized molecules, intrinsically underestimate the characteristic length of range separation in large π-conjugated systems, leading to an underestimation of electron delocalization. This finding is in line with earlier results for polyenes and other long π-conjugated systems.[71] The flattened line shapes seen in Figure 3.5 are also indicative of this trend: little change in torsional barrier is seen after n = 4. Thus, the effective conjugation length is predicted to be too short with these methods. These results can directly be related to the ω value in each functional; for ωPBEh (ω = 0.200 $bohr^{-1}$), ωPBE (ω = 0.400 $bohr^{-1}$), ωB97 (ω = 0.400 $bohr^{-1}$), BOP (ω = 0.400 $bohr^{-1}$), and BNL (ω = 0.500 $bohr^{-1}$), we find projected torsion potentials at the polymer limit of 8.02 [1.30], 7.32 [0.88], 7.31 [0.96], 7.37 [0.83], and 7.09 [0.79] kcal mol^{-1} for polyenes [oligodiacetylenes], respectively. This shows that the fixed ω value is the determining factor for the calculated torsion barrier in the polymer limit, consistently with what was shown for HF exchange in global hybrid approaches. This is especially evident for the computed torsional potentials using ωPBE, BNL, and ωB97, which all share an ω value

of 0.400 $bohr^{-1}$ and show computed differences of less than 0.1 kcal mol^{-1}. The calculated MESIEs for ωPBEh and ωPBE correspond to a localization error of +1.62 [2.33] and +3.04 [2.59] kcal mol^{-1} for the n = 14 polyene [n = 10 oligodiacetylene] (Figure 3.6); the MESIEs at different torsional angles are seen to differ by up to 0.6 kcal mol^{-1}.

As has been demonstrated and discussed in more detail in several recent publications,[72-77] the MESIE can be reduced by several orders of magnitude by tuning the range-separation parameter using the non-empirical IP-tuning procedure discussed above. To further understand the connection between the MESIE and the error in the torsion potentials, it is useful to directly compare the error in the torsion potentials with the MESIE in the used functionals. For this, the range-separation parameter was optimized for each n and then employed to calculate the torsion barrier for polyenes and oligodiacetylenes. IP-tuned ωPBEh, ωPBE, ωB97, BOP, and BNL give errors in the torsion barriers of +0.12 [+0.11], -0.14 [-0.03], -0.77 [+0.11], -0.19 [0.00], and -0.56 [+0.02] kcal mol^{-1} relative to DB-DFMP2 at the polymer limit for polyenes [oligodiacetylenes]. That is, the agreement of the torsion potentials computed with the IP-tuned LRC functionals increases substantially over the barriers computed using the standard ω values. These results demonstrate that for long π-conjugated molecular chains, the standard ω values prematurely truncate the characteristic length over which the electrons delocalize. Therefore, upon tuning the range-separation parameter, we see a growth in the computed torsion barrier similar to that of the DB-DFMP2-calculated progression. The calculated MESIE for IP-tuned ωPBE and ωPBEh also results in a substantial decrease in the localization error; MESIE values of +0.18 [+0.08] and +0.38 [+0.16] kcal mol^{-1} are calculated for IP-tuned ωPBEh and ωPBE, respectively, for the n = 14 polyene [n = 10 oligodiacetylene] (Figure 3.6). However, in contrast to what was observed

for the MESIE computed for the (semi)local functionals, the MESIEs for IP-tuned functionals at various θ values for the polyenes change the qualitative picture:[71] for example, the computed localization error of 0.38 kcal mol^{-1} computed for IP-tuned ωPBE at θ = 180° changes to -0.15 kcal mol^{-1} at θ = 100°; this is related to the dependence of the actual IP-tuned ω on the torsion angle, which was observed in our previous study on polyenes.[71]

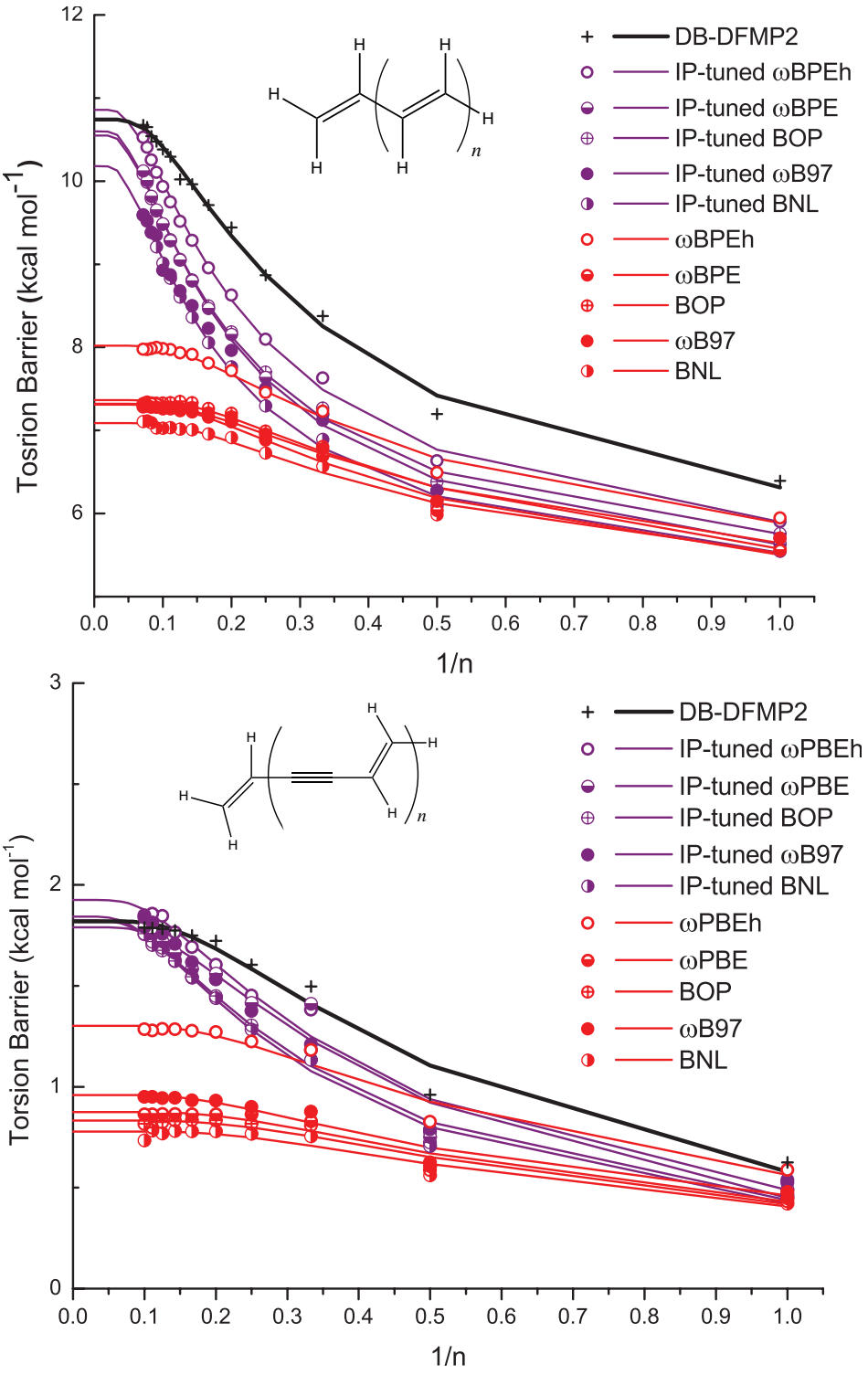

Figure 3.5. Evolution of the computed torsional barriers in polyenes (top) and oligodiacetylene (bottom) for a set of standard and IP-tuned long-range corrected hybrid functionals as a function of the inverse number of repeat units, n. The results for the torsion barriers are fitted using the effective conjugation length model of Eq. **(3.1)** and extrapolated to the polymer limit (solid lines).

However, our results also reveal an issue with the IP-tuning procedure. Figure 3.5 shows that the saturation point reached for DB-DFMP2 and most of the global hybrids (*i.e.*, where the torsion potential does no longer increase with size) is not seen in the IP-tuned LRC functionals. Instead, the IP-tuned torsion potentials continue to grow with oligomer length. This issue has also been observed in the context of earlier studies.[71,72,84] For highly conjugated systems, the characteristic length of the range separation as determined from the IP-tuning procedure grows almost linearly with system size; the IP-tuning procedure then eventually leads to an ω value that approaches zero, in which case the LRC functional goes over to a purely semilocal functional in the polymer limit.[71] This problem has been demonstrated by some of us to have important consequences for the calculation of the degree of bond-length alternation in polyenes.[72] As in the case of the torsion barriers in the present work, the IP-tuning procedure significantly improves bond-length alternation for medium-sized oligomers but is not able to predict the correct structural properties at the polymer limit. Clearly, improved tuning procedures and/or LRC functionals have to be developed to circumvent this intricate problem. It might be that a single ω length-scale parameter does not adequately provide for the division of the exchange hole, and that a density-dependent ω would be more appropriate, *e.g.*, as in the work of Scuseria and co-workers.[85] Alternatively, correlation might be the source of the problem, in which case range-separation of the correlation hole could provide superior accuracy, *e.g.*, as has been applied by Chabbal *et al*. for the accurate determination of bond-length alternation in polyenes.[86]

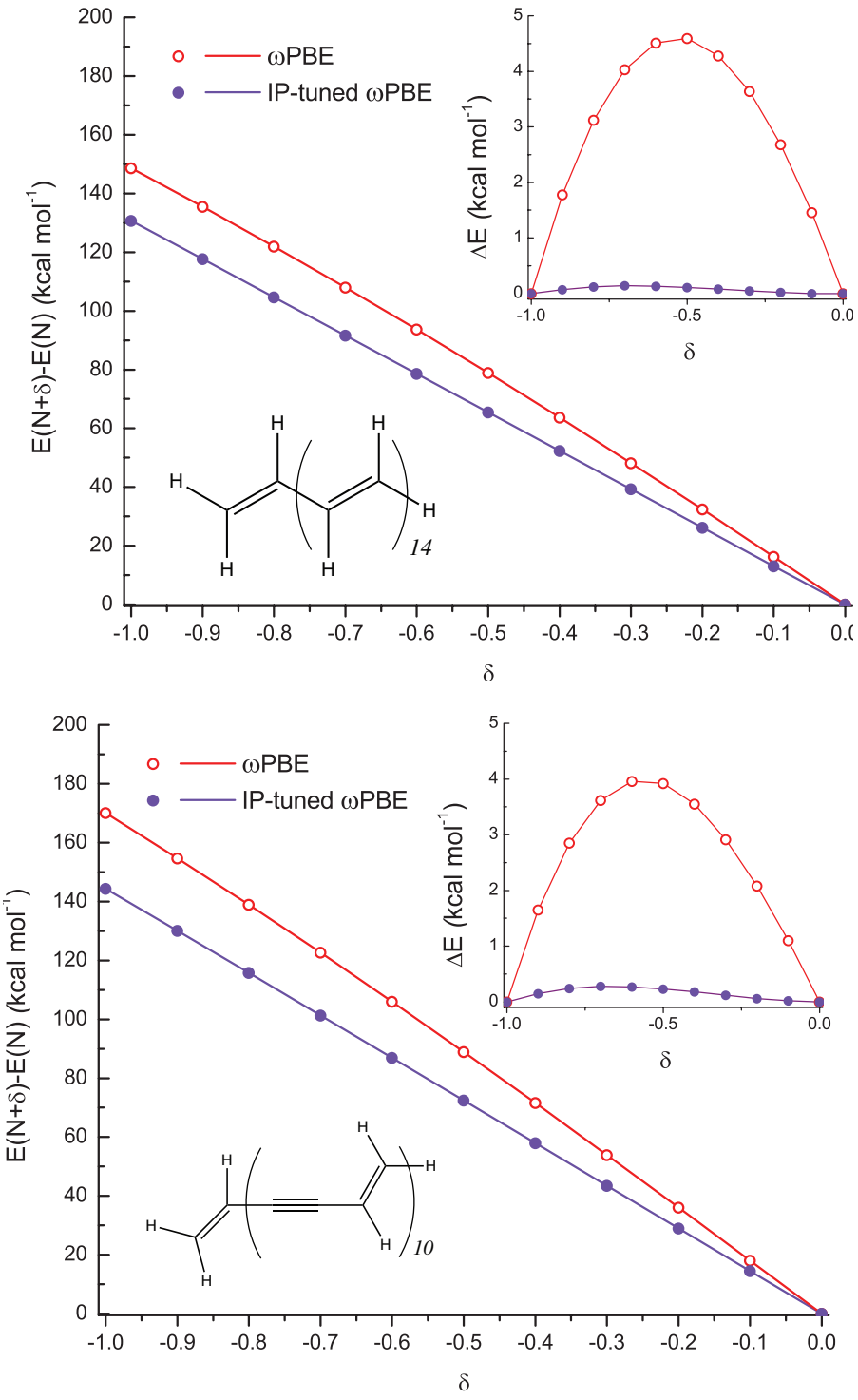

Figure 3.6. Change in relative energy as a function of fractional occupation number for the n = 14 polyene (top) and the n = 10 oligodiacetylene (bottom) when going from the neutral molecule (δ = 0) to the cation (δ = -1) for ωPBE (red) and IP-tuned ωPBE (purple), using the respective optimized neutral geometries. The inset shows the deviation of relative energy from a straight line that connects the end points δ = 0 and δ = -1.

3.4. Conclusions

Various DFT functionals were compared with high-level DB-DFMP2/aug-cc-pVDZ calculations on polyenes and oligodiacetylenes as a way to demonstrate the disparity in the treatment of π-conjugated systems using commonly used DFT functionals. To assess the performance and reliability of the DFT functionals, the torsion barriers for $n = 1 – 14$ [$n = 1 – 10$] repeat units for polyenes [oligodiacetylenes] were evaluated. When compared to DB-DFMP2/aug-cc-pVDZ results, the computed torsional barriers very strongly depends on the DFT functional used, which can be attributed primarily to the fraction of HF exchange used in the respective functionals.

It is found that the meta-GGA functionals BMK and M06 lead to the closest values to the DB-DFMP2 values. Though it may be an indication of the accuracy of these particular semilocal exchange-correlation functionals, the results we have obtained in this work clearly demonstrate the overwhelming importance of the amount of HF exchange in accurately describing the torsion barriers for these conjugated systems and point to the fact that the success of BMK and M06 can be ascribed primarily to the employed fractions of HF exchange. Through an analysis of system energy versus fractional electron number, it is shown that various standard DFT methods suffer from delocalization or localization errors, depending on the amount of HF exchange in a given method. This point was further demonstrated for the LRC functionals that give wide-ranging results depending on the pre-defined range-separation parameter (ω) value. However, through non-empirically tuning the ω value, all of the IP-optimized LRC functionals significantly improve the torsion barriers when compared to the DB-DFMP2 results. This finding can be

understood in terms of a marked reduction in MESIE as a consequence of the IP-tuning procedure.

3.5. References

1. Bredas, J. L.; Street, G. B., Polarons, bipolarons, and solitons in conducting polymers. *Accounts of Chemical Research* **1985**, *18*, 309-315.
2. Kertesz, M.; Choi, C. H.; Yang, S., Conjugated Polymers and Aromaticity. *Chemical Reviews* **2005**, *105*, 3448-3481.
3. Coropceanu, V.; Cornil, J.; da Silva Filho, D. A.; Olivier, Y.; Silbey, R.; Bredas, J. L., Charge Transport in Organic Semiconductors. *Chemical Reviews* **2007**, *107*, 926-952.
4. Ito, T.; Shirakawa, H.; Ikeda, S., Simultaneous polymerization and formation of polyacetylene film on the surface of concentrated soluble Ziegler-type catalyst solution. *Journal of Polymer Science: Polymer Chemistry Edition* **1974**, *12*, 11-20.
5. Chiang, C. K.; Druy, M. A.; Gau, S. C.; Heeger, A. J.; Louis, E. J.; MacDiarmid, A. G.; Park, Y. W.; Shirakawa, H., Synthesis of highly conducting films of derivatives of polyacetylene, (CH)x. *Journal of the American Chemical Society* **1978**, *100*, 1013-1015.
6. Park, Y. W.; Heeger, A. J.; Druy, M. A.; MacDiarmid, A. G., Electrical transport in doped polyacetylene. *The Journal of Chemical Physics* **1980**, *73*, 946-957.
7. Choi, C. H.; Kertesz, M.; Karpfen, A., The effects of electron correlation on the degree of bond alternation and electronic structure of oligomers of polyacetylene. *The Journal of Chemical Physics* **1997**, *107*, 6712-6721.
8. Salzner, U.; Lagowski, J. B.; Pickup, P. G.; Poirier, R. A., Comparison of geometries and electronic structures of polyacetylene, polyborole, polycyclopentadiene, polypyrrole, polyfuran, polysilole, polyphosphole, polythiophene, polyselenophene and polytellurophene. *Synthetic Metals* **1998**, *96*, 177-189.
9. Champagne, B.; Perpète, E. A.; Gisbergen, S. J. A. v.; Baerends, E.-J.; Snijders, J. G.; Soubra-Ghaoui, C.; Robins, K. A.; Kirtman, B., Assessment of conventional density functional schemes for computing the polarizabilities and hyperpolarizabilities of conjugated oligomers: An ab initio investigation of polyacetylene chains. *The Journal of Chemical Physics* **1998**, *109*, 10489-10498.
10. Chance, R. R., Chromism in Polydiacetylene Solutions and Crystals. *Macromolecules* **1980**, *13*, 396-398.
11. Tanaka, H.; Gomez, M. A.; Tonelli, A. E.; Thakur, M., Thermochromic phase transition of a polydiacetylene, poly(ETCD), studied by high-resolution solid-state carbon-13 NMR. *Macromolecules* **1989**, *22*, 1208-1215.
12. Schott, M., The Colors of Polydiacetylenes: a Commentary. *The Journal of Physical Chemistry B* **2006**, *110*, 15864-15868.
13. Perdew, J. P.; Zunger, A., Self-interaction correction to density-functional approximations for many-electron systems. *Physical Review B* **1981**, *23*, 5048.
14. Polo, V.; Kraka, E.; Cremer, D., Electron correlation and the self-interaction error of density functional theory. *Molecular Physics* **2002**, *100*, 1771-1790.

15. Lundberg, M.; Siegbahn, P. E. M., *Quantifying the effects of the self-interaction error in DFT: When do the delocalized states appear?*; AIP, 2005; Vol. 122, p 224103.
16. Mori-Sánchez, P.; Cohen, A. J.; Yang, W., Many-electron self-interaction error in approximate density functionals. *The Journal of Chemical Physics* **2006**, *125*, 201102-4.
17. Mori-Sánchez, P.; Cohen, A. J.; Yang, W., Localization and Delocalization Errors in Density Functional Theory and Implications for Band-Gap Prediction. *Physical Review Letters* **2008**, *100*, 146401.
18. Körzdörfer, T.; Kümmel, S.; Marom, N.; Kronik, L., When to trust photoelectron spectra from Kohn-Sham eigenvalues: The case of organic semiconductors. *Physical Review B* **2009**, *79*, 201205.
19. Körzdörfer, T.; Kümmel, S.; Marom, N.; Kronik, L., Erratum: When to trust photoelectron spectra from Kohn-Sham eigenvalues: The case of organic semiconductors. [Physical Review B 79, 201205 (2009)]. *Physical Review B* **2010**, *82*, 129903(E).
20. Cohen, A. J.; Mori-Sánchez, P.; Yang, W., Challenges for Density Functional Theory. *Chemical Reviews* **2011**, *112*, 289-320.
21. Körzdörfer, T., On the relation between orbital-localization and self-interaction errors in the density functional theory treatment of organic semiconductors. *The Journal of Chemical Physics* **2011**, *134*, 094111-9.
22. Cohen, A. J.; Mori-Sánchez, P.; Yang, W., Insights into Current Limitations of Density Functional Theory. *Science* **2008**, *321*, 792-794.
23. Ruzsinszky, A.; Perdew, J. P.; Csonka, G. I.; Vydrov, O. A.; Scuseria, G. E., Spurious fractional charge on dissociated atoms: Pervasive and resilient self-interaction error of common density functionals. *The Journal of Chemical Physics* **2006**, *125*, 194112-8.
24. Zhao, Y.; Lynch, B. J.; Truhlar, D. G., Development and Assessment of a New Hybrid Density Functional Model for Thermochemical Kinetics. *The Journal of Physical Chemistry A* **2004**, *108*, 2715-2719.
25. Stein, T.; Eisenberg, H.; Kronik, L.; Baer, R., Fundamental Gaps in Finite Systems from Eigenvalues of a Generalized Kohn-Sham Method. *Physical Review Letters* **2010**, *105*, 266802.
26. Sai, N.; Barbara, P. F.; Leung, K., Hole Localization in Molecular Crystals from Hybrid Density Functional Theory. *Physical Review Letters* **2011**, *106*, 226403.
27. Dreuw, A.; Head-Gordon, M., Failure of Time-Dependent Density Functional Theory for Long-Range Charge-Transfer Excited States: The Zincbacteriochlorin−Bacteriochlorin and Bacteriochlorophyll−Spheroidene Complexes. *Journal of the American Chemical Society* **2004**, *126*, 4007-4016.
28. Peach, M. J. G.; Helgaker, T.; Salek, P.; Keal, T. W.; Lutnaes, O. B.; Tozer, D. J.; Handy, N. C., Assessment of a Coulomb-attenuated exchange-correlation energy functional. *Physical Chemistry Chemical Physics* **2006**, *8*, 558-562.
29. Zhao, Y.; Truhlar, D. G., Density Functional for Spectroscopy: No Long-Range Self-Interaction Error, Good Performance for Rydberg and Charge-Transfer States, and Better Performance on Average than B3LYP for Ground States. *The Journal of Physical Chemistry A* **2006**, *110*, 13126-13130.
30. Sini, G.; Sears, J. S.; Bredas, J. L., Evaluating the Performance of DFT Functionals in Assessing the Interaction Energy and Ground-State Charge Transfer of Donor/Acceptor Complexes: Tetrathiafulvalene−Tetracyanoquinodimethane (TTF−TCNQ) as a Model Case. *Journal of Chemical Theory and Computation* **2011**, *7*, 602-609.

31. Choi, C. H.; Kertesz, M.; Karpfen, A., Limitations of current density functional theories for the description of partial π-bond breaking. *Chemical Physics Letters* **1997**, *276*, 266-268.
32. Sancho-García, J. C.; Pérez-Jiménez, A. J.; Pérez-Jorda, J. M.; Moscardo, F., Torsional potential of 1,3-butadiene: ab initio calculations. *Molecular Physics: An International Journal at the Interface Between Chemistry and Physics* **2001**, *99*, 47 - 51.
33. Sancho-García, J. C.; Bredas, J. L.; Cornil, J., Assessment of the reliability of the Perdew-Burke-Ernzerhof functionals in the determination of torsional potentials in π-conjugated molecules. *Chemical Physics Letters* **2003**, *377*, 63-68.
34. Sancho-García, J. C.; Cornil, J., Assessment of recently developed exchange-correlation functionals for the description of torsion potentials in π-conjugated molecules. *The Journal of Chemical Physics* **2004**, *121*, 3096-3101.
35. Sancho-García, J. C., Assessing a new nonempirical density functional: Difficulties in treating pi-conjugation effects. *The Journal of Chemical Physics* **2006**, *124*, 124112-10.
36. Fabiano, E.; Della Sala, F., Torsional potential of π-conjugated molecules using the localized Hartree-Fock Kohn-Sham exchange potential. *Chemical Physics Letters* **2006**, *418*, 496-501;
37. Sancho-García, J. C.; Pérez-Jiménez, A. J., Assessment of double-hybrid energy functionals for π-conjugated systems. *The Journal of Chemical Physics* **2009**, *131*, 084108-11.
38. Karpfen, A.; Choi, C. H.; Kertesz, M., Single-Bond Torsional Potentials in Conjugated Systems: A Comparison of ab Initio and Density Functional Results. *The Journal of Physical Chemistry A* **1997**, *101*, 7426-7433.
39. Perdew, J. P.; Burke, K.; Ernzerhof, M., Generalized gradient approximation made simple. *Physical Review Letters* **1996**, *77*, 3865-3868.
40. Perdew, J. P.; Burke, K.; Ernzerhof, M., Errata: Generalized gradient approximation made simple. *Physical Review Letters* **1997**, *78*, 1396E.
41. Sears, J. S.; Chance, R. R.; Bredas, J. L., Torsion Potential in Polydiacetylene: Accurate Computations on Oligomers Extrapolated to the Polymer Limit. *Journal of the American Chemical Society* **2010**, *132*, 13313-13319.
42. Marshall, M. S.; Sears, J. S.; Burns, L. A.; Bredas, J. L.; Sherrill, C. D., An Error and Efficiency Analysis of Approximations to Møller−Plesset Perturbation Theory. *Journal of Chemical Theory and Computation* **2010**, *6*, 3681-3687.
43. Shao, Y.; Molnar, L. F.; Jung, Y.; Kussmann, J.; Ochsenfeld, C.; Brown, S. T.; Gilbert, A. T. B.; Slipchenko, L. V.; Levchenko, S. V.; O'Neill, D. P.; DiStasio Jr, R. A.; Lochan, R. C.; Wang, T.; Beran, G. J. O.; Besley, N. A.; Herbert, J. M.; Yeh Lin, C.; Van Voorhis, T.; Hung Chien, S.; Sodt, A.; Steele, R. P.; Rassolov, V. A.; Maslen, P. E.; Korambath, P. P.; Adamson, R. D.; Austin, B.; Baker, J.; Byrd, E. F. C.; Dachsel, H.; Doerksen, R. J.; Dreuw, A.; Dunietz, B. D.; Dutoi, A. D.; Furlani, T. R.; Gwaltney, S. R.; Heyden, A.; Hirata, S.; Hsu, C.-P.; Kedziora, G.; Khalliulin, R. Z.; Klunzinger, P.; Lee, A. M.; Lee, M. S.; Liang, W.; Lotan, I.; Nair, N.; Peters, B.; Proynov, E. I.; Pieniazek, P. A.; Min Rhee, Y.; Ritchie, J.; Rosta, E.; David Sherrill, C.; Simmonett, A. C.; Subotnik, J. E.; Lee Woodcock Iii, H.; Zhang, W.; Bell, A. T.; Chakraborty, A. K.; Chipman, D. M.; Keil, F. J.; Warshel, A.; Hehre, W. J.; Schaefer Iii, H. F.; Kong, J.; Krylov, A. I.; Gill, P. M. W.; Head-Gordon, M., Advances in methods and algorithms in a modern quantum chemistry program package. *Physical Chemistry Chemical Physics* **2006**, *8*, 3172-3191.
44. R. A Kendall, T. H. D., Jr., R. J. Harrison Electron Affinities of the First-Row Atoms Revisited. Systematic Basis Sets and Wave Functions. *Journal of Chemical Physics* **1992**, *96*, 6796-6806.

45. Meier, H.; Stalmach, U.; Kolshorn, H., Effective conjugation length and UV/vis spectra of oligomers. *Acta Polymerica* **1997**, *48*, 379-384.
46. Distasio, R. A.; Steele, R. P.; Head-Gordon, M., The analytical gradient of dual-basis resolution-of-the-identity second-order Møller–Plesset perturbation theory. *Molecular Physics* **2007**, *105*, 2731-2742.
47. Ksiazek, A.; Wolinski, K., Molecular properties with dual basis set methods. *Molecular Physics* **2008**, *106*, 769-786.
48. Kendall, R. A.; Früchtl, H. A., The impact of the resolution of the identity approximate integral method on modern ab initio algorithm development. *Theoretical Chemistry Accounts: Theory, Computation, and Modeling (Theoretica Chimica Acta)* **1997**, *97*, 158-163.
49. Feyereisen, M.; Fitzgerald, G.; Komornicki, A., Use of Approximate Integrals in Ab Initio Theory - An Application in MP2 Energy Calcaulations. *Chemical Physics Letters* **1993**, *208*, 359-363.
50. Hohenberg, P.; Kohn, W., Inhomogeneous Electron Gas. *Physical Review* **1964**, *136*, B864-B871.
51. Slater, J. C., In *The Self-Consistent Field for Molecular and Solids, Quantum Theory of Molecular and Solids*, McGraw-Hill: New York, 1974; Vol. 4.
52. Vosko, S. H.; Wilk, L.; Nusair, M., Accurate Spin-Dependent Electron Liquid Correlation Energies for Local Sping-Denisty Calculations - A Critcal Analysis. *Can. J. Phys.* **1980**, *58*, 1200-1211.
53. Kohn, W.; Sham, L. J., Self-Consistent Equations Including Exchange and Correlation Effects. *Physical Review* **1965**, *140*, A1133-A1138.
54. Becke, A. D., Density-functional exchange-energy approximation with correct asymptotic behaviour. . *Physical Reviews A* **1988**, *38*, 3098-3100.
55. Perdew, J. P., Density-functional approximation for the correlation-energy of the inhomogenous electron gas. *Physical Review B* **1986**, *33*, 8822-8824.
56. Zhao, Y.; Truhlar, D. G., A new local density functional for main-group thermochemistry, transition metal bonding, thermochemical kinetics, and noncovalent interactions. *The Journal of Chemical Physics* **2006**, *125*, 194101.
57. Lee, C.; Yang, W.; Parr, R. G., Development of the Colle-Salvetti correlation-energy formula into a functional of the electron density. . *Physical Review B* **1988**, *37*, 785-789.
58. Becke, A. D., Density-functional thermochemistry. III. The role of exact exchange. . *The Journal of Chemical Physics* **1993**, *98*, 5648.
59. Adamo, C.; Barone, V., Toward reliable density functional methods without adjustable parameters: The PBE0 model. *The Journal of Chemical Physics* **1999**, *110*, 6158-6170.
60. Boese, A. D.; Martin, J. M. L., Development of Density Functionals for Thermochemical Kinetics. *The Journal of Chemical Physics* **2004**, *121*, 3405-3416.
61. Zhao, Y.; Truhlar, D., The M06 suite of density functionals for main group thermochemistry, thermochemical kinetics, noncovalent interactions, excited states, and transition elements: two new functionals and systematic testing of four M06-class functionals and 12 other functionals. *Theoretical Chemistry Accounts: Theory, Computation, and Modeling (Theoretica Chimica Acta)* **2008**, *120*, 215-241.
62. Zhao, Y.; Truhlar, D. G., Comparative DFT Study of van der Waals Complexes: Rare-Gas Dimers, Alkaline-Earth Dimers, Zinc Dimer, and Zinc-Rare-Gas Dimers. *The Journal of Physical Chemistry A* **2006**, *110*, 5121-5129.

63. Henderson, T. M.; Janesko, B. G.; Scuseria, G. E., Generalized gradient approximation model exchange holes for range-separated hybrids. *The Journal of Chemical Physics* **2008**, *128*, 194105-9.
64. Chai, J.-D.; Head-Gordon, M., Systematic optimization of long-range corrected hybrid density functionals. *The Journal of Chemical Physics* **2008**, *128*, 084106.
65. Chai, J.-D.; Head-Gordon, M., Long-range corrected hybrid density functionals with damped atom-atom dispersion corrections. *Physical Chemistry Chemical Physics* **2008**, *10*, 6615-6620.
66. Tsuneda, T.; Kamiya, M.; Morinaga, N.; Hirao, K., A transversing connection between density functionals. *The Journal of Chemical Physics* **2001**, *114*, 6505-6513.
67. Baer, R.; Neuhauser, D., Density Functional Theory with Correct Long-Range Asymptotic Behavior. *Physical Review Letters* **2005**, *94*, 043002.
68. Livshits, E.; Baer, R., A well-tempered density functional theory of electrons in molecules. *Physcial Chemistry Chemical Physics* **2007**, *9*, 2932-2941.
69. Savin, A.; Flad, H.-J., Density functionals for the Yukawa electron-electron interaction. *International Journal of Quantum Chemistry* **1995**, *56*, 327-332.
70. Janak, J. F., Proof that $\partial E/\partial ni = \varepsilon$ in density-functional theory. *Physical Review B* **1978**, *18*, 7165-7168.
71. Körzdörfer, T.; Sears, J. S.; Sutton, C.; Bredas, J. L., Long-range corrected hybrid functionals for π-conjugated systems: Dependence of the range-separation parameter on conjugation length. *The Journal of Chemical Physics* **2011**, *135*, 204107-6.
72. Körzdörfer, T.; Parrish, R. M.; Sears, J. S.; Sherrill, C. D.; Bredas, J. L., On the relationship between bond-length alternation and many-electron self-interaction error. *The Journal of Chemical Physics* **2012**, *137*, 124305-8.
73. Srebro, M.; Autschbach, J., Does a Molecule-Specific Density Functional Give an Accurate Electron Density? The Challenging Case of the CuCl Electric Field Gradient. *The Journal of Physical Chemistry Letters* **2012**, *3*, 576-581.
74. Körzdörfer, T.; Parrish, R. M.; Marom, N.; Sears, J. S.; Sherrill, C. D.; Bredas, J. L., Assessment of the performance of tuned range-separated hybrid density functionals in predicting accurate quasiparticle spectra. *Physical Review B* **2012**, *86*, 205110.
75. Stein, T.; Autschbach, J.; Govind, N.; Kronik, L.; Baer, R., Curvature and Frontier Orbital Energies in Density Functional Theory. *The Journal of Physical Chemistry Letters* **2012**, *3*, 3740-3744.
76. Salzner, U.; Baer, R., Koopmans' springs to life. *The Journal of Chemical Physics* **2009**, *131*.
77. Gledhill, J. D.; Peach, M. J. G.; Tozer, D. J., Assessment of Tuning Methods for Enforcing Approximate Energy Linearity in Range-Separated Hybrid Functionals. *Journal of Chemical Theory and Computation* **2013**, *9*, 4414-4420.
78. Stein, T.; Kronik, L.; Baer, R., Reliable Prediction of Charge Transfer Excitations in Molecular Complexes Using Time-Dependent Density Functional Theory. *Journal of the American Chemical Society* **2009**, *131*, 2818-2820.
79. Perdew, J. P.; Parr, R. G.; Levy, M.; Balduz, J. L., Jr., Density-Functional Theory for Fractional Particle Number: Derivative Discontinuities of the Energy. *Physical Review Letters* **1982**, *49*, 1691-1694.
80. Turney, J. M.; Simmonett, A. C.; Parrish, R. M.; Hohenstein, E. G.; Evangelista, F. A.; Fermann, J. T.; Mintz, B. J.; Burns, L. A.; Wilke, J. J.; Abrams, M. L.; Russ, N. J.; Leininger, M. L.; Janssen, C. L.; Seidl, E. T.; Allen, W. D.; Schaefer, H. F.; King, R. A.; Valeev, E. F.;

Sherrill, C. D.; Crawford, T. D., *Wiley Interdisciplinary Reviews: Computational Molecular Science 2* **2012**, *4*, 556-565.
81. Feller, D.; Craig, N. C., High Level ab Initio Energies and Structures for the Rotamers of 1,3-Butadiene. *The Journal of Physical Chemistry A* **2009**, *113*, 1601-1607.
82. Karpfen, A.; Parasuk, V., Accurate torsional potentials in conjugated systems: ab initio and density functional calculations on 1,3-butadiene and monohalogenated butadienes. *Molecular Physics: An International Journal at the Interface Between Chemistry and Physics* **2004**, *102*, 819 - 826.
83. Engeln, R.; Consalvo, D.; Reuss, J., Evidence for a gauche minor conformer of 1,3-butadiene. *Chemical Physics* **1992**, *160*, 427-433.
84. Salzner, U.; Aydin, A., Improved Prediction of Properties of π-Conjugated Oligomers with Range-Separated Hybrid Density Functionals. *Journal of Chemical Theory and Computation* **2011**, *7*, 2568-2583.
85. Krukau, A. V.; Scuseria, G. E.; Perdew, J. P.; Savin, A., Hybrid functionals with local range separation. *The Journal of Chemical Physics* **2008**, *129*, 124103.
86. Chabbal, S.; Jacquemin, D.; Adamo, C.; Stoll, H.; Leininger, T., Communication: Bond length alternation of conjugated oligomers: Another step on the fifth rung of Perdew's ladder of functional. *The Journal of Chemical Physics* **2010**, *133*, 151104-151109.

Chapter 4 Rigorously Modeling Charge Transport in Single-Molecule Systems

4.1. Introduction

Mixed valence (MV) systems are compounds that contain two or more redox centers in different oxidation states.[1] Here, we focus on organic MV systems that contain two redox sites; a charge can then either localize on one of the redox centers or delocalize over both. The electronic and optical properties of MV systems are defined by the competition between the electronic coupling (hereafter denoted as t) among redox centers and the vibronic coupling; in simple models, the latter is given by the Marcus reorganization energy (λ). Depending on the relative strengths of these two parameters, MV systems are commonly classified into three categories (Robin-Day classification):[1] class-I (negligible electronic coupling, $\lambda \gg 2t$), class-II (weak electronic coupling, $\lambda > 2t$), and class-III (strong electronic coupling, $\lambda \leq 2t$) systems. In class-I and class-II systems, the lowest adiabatic potential energy surface presents two equivalent minima corresponding to two broken-symmetry geometry configurations with the charge predominantly localized on one of the redox sites. On the other hand, the ground state of class-III MV systems is characterized by a symmetric potential energy surface with a single minimum and complete charge delocalization.

Experimentally, important information about organic MV systems can be derived by means of various techniques such as optical absorption, electron spin resonance, or gas-phase ultraviolet photoelectron spectroscopy.[2-14] For example, in optical absorption, the assignment of class-II and class-III systems can be made based on the shape of the low-energy charge-transfer (CT) band;

broad and symmetric bands imply a class-II classification while narrower, asymmetric bands are indicative of class-III compounds.[3,15-17] In practice, however, this classification can be hard to assign due to overlapping bands from other transitions and the vibrational details of the CT band in class-III systems that can possibly also lead to broad and almost completely symmetric bands.[10]

In general, experimental studies are hindered by complications arising from temperature effects, the time scale for charge transfer, and environmental effects (which for some systems can result simultaneously in localization and delocalization effects).[18] Therefore, for a complete understanding of the MV properties, a reliable theoretical description of the geometric and electronic structure of these systems is required, which has been the goal of many recent studies.[19-24] However, even when considering isolated molecules (to avoid the complications related to environment effects), a method capable of reliably distinguishing between class-II and class-III MV systems is still lacking in the case of large MV systems that cannot be treated with highly correlated wave-function methods.

Density functional theory (DFT) is widely used for electronic-structure calculations of organic molecules and other systems of chemical interest because of a combination of reasonable computational cost and generally sufficient accuracy. However, it is well established that standard semilocal and global hybrid exchange-correlation functionals (*e.g.*, B3LYP) do not correctly cancel the long-range self-Coulomb interactions, resulting in a spurious self-repulsion of charge densities.[25,26] As a result, the widely used semilocal and global hybrid approximations to the exchange-correlation functional can fail dramatically for the description of MV systems;

they consistently delocalize the charge symmetrically over both redox centers, even for MV systems with very small electronic couplings (in the absence of solvent).[6,7,20] The amount of HF exchange employed in global hybrid functionals (but typically only in conjunction with a solvent model) was seen earlier to reduce the degree of spurious delocalization in MV systems, which demonstrates the importance that Hartree-Fock (HF) exchange has in reducing the error inherent to semilocal DFT approaches.[20] Renz *et al.* [20] have shown that too little HF exchange is included in standard hybrid DFT functionals for applicability to MV systems and therefore the charge delocalization is consistently overestimated; about 35% of HF exchange together with solvent consideration was proposed by these authors as a reasonable tradeoff. However, this approach essentially benefits from a cancelation of errors between the functional and the solvation method. Since in this approach the amount of HF exchange explicitly considered is insensitive to the characteristics of a specific system, it becomes very difficult to estimate how this approach will perform for a range of different MV systems and solvents. On the other hand, it is well known that methods that include too much HF exchange consistently overlocalize the charge,[26,27] leading to spurious symmetry breaking even in the case of systems with large electronic couplings.[5,27,28] With HF [standard DFT] spuriously localizing [delocalizing] charge densities, both HF and standard DFT approaches can happen to yield a correct Robin-Day classification, however, possibly for the wrong reasons.

It is helpful at this stage to consider the many-electron self-interaction error (MESIE) that has been discussed extensively in the literature on density functional approximations. Following Refs. 29,30, an approximation to the exchange-correlation functional is called free from MESIE if it obeys a property required of the exact exchange-correlation functional in the case of

fractional particle numbers, which is that the total energy as a function of fractional occupation must correspond to a series of straight lines with kinks at integer occupations.[31] In this context, neither HF (which is free from one-electron self-interaction errors) nor any of the commonly used density functional approximations are free from MESIE. However, the deviations from the straight-line behavior are different for HF and DFT. Standard DFT functionals yield convex curves for energy vs. fractional occupation, which is consistent with the fact that they favor delocalized over localized charges; in contrast, curves obtained from HF theory are concave, *i.e.*, consistent with HF spuriously favoring charge localization (the MESIEs in HF and DFT are frequently referred to as localization and delocalization errors, respectively).[26,27]

Recently, long-range corrected (LRC) functionals have been introduced as a way to reduce the MESIE and provide a better balance between localization and delocalization effects.[32-34] Here our main goal is to demonstrate a methodology capable of describing reliably the intrinsic factors that determine the nature of the coupling between redox centers in MV systems. We consider an LRC functional and nonempirically optimize the range-separation parameter ω via ionization potential (IP) tuning. This approach has the distinct advantage over empirically tuning the amount of HF exchange in global hybrid functionals as suggested in previous studies[20,23,24] that no assumption needs to be made about the classification of the MV system *a priori*.

We first discuss the impact that the MESIE has in determining the extent of over-(de)localization of the excess charge in representative organic MV systems. Then, we use a nonempirically tuned long-range corrected hybrid functional to minimize the MESIE and the (de)localization error; the IP-tuning procedure is anticipated to reduce the MESIE in the highest occupied molecular orbital

(HOMO) by several orders of magnitude, thereby practically removing the spurious delocalization of the excess charge seen in common functionals.[32-34] We demonstrate that this approach leads to a reliable DFT methodology capable of correctly assessing charge (de)localization in MV systems; this is done for the three organic MV compounds illustrated in their neutral ground-state structure in Figure 4.1, which are chosen to represent class-II, class-III, and borderline class-II/III cases.

We note that there are two contributions to the reorganization energy related to the electron-transfer process: an internal (or inner) reorganization due to electron coupling with intramolecular vibration modes and external (or outer) reorganization due to the coupling with the surrounding medium (solvent). Since a clear distinction between these contributions is important in order to avoid any spurious cancellation of errors, we have chosen here to neglect the role of solvent by considering isolated molecules and to concentrate our analysis on the internal reorganization. While we note that for the borderline class-II/class-III systems studied experimentally the choice of solvent influences the reorganization energy and, hence, the Robin-Day classification, the main goal of our study is to demonstrate a method capable of accurately determining the strength of the coupling between redox centers in MV systems. Thus, our objective is to provide insight into the many *intrinsic* factors that affect the charge-transfer process in these systems, such as the electronic nature of bridging groups,[35,36] orientation of redox centers,[37-39] steric effects,[40,41] and substituent effects.[42]

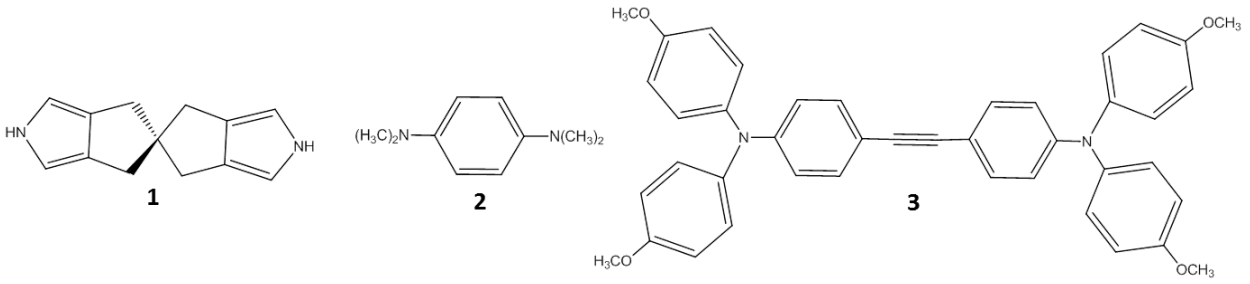

Figure 4.1. Chemical structure of the neutral ground state of the mixed-valence systems used in this study: 1) 5-methyl-5-((4-methyl-1H-pyrrol-3-yl)methyl)-2,4,5,6-tetrahydrocyclopenta[c]pyrrole; 2) N^1,N^1,N^4,N^4-tetramethylbenzene-1,4-diamine; and 3) 4,4'-(ethyne-1,2-diyl)bis(*N*,*N*-bis(4-methoxyphenyl)aniline).

4.2. Methodology

Geometry optimizations were performed using Gaussian 09 (Rev. B)[43] at the HF, B3LYP,[44-46] and long-range corrected hybrid ωB97[47] levels with the cc-pVDZ basis set.[48] Molecular geometries were optimized using spin-restricted calculations for the neutral ground states and spin-unrestricted calculations for the radical-cation states. Larger basis sets were also examined to determine the impact on the excitation and reorganization energies for $\mathbf{1}^+$ (Table 4.1); changes of only about 0.1 eV in the excitation energies and about 0.01 eV in the thermal barriers was found when using the larger basis sets aug-cc-pVDZ and cc-pVTZ compared to cc-pVDZ.

Table 4.1. Basis set dependence of IP-tuned ωB97 computed transition energies (ΔE) and electron transfer barriers for $\mathbf{1}^{+}$. All values in eV.

Basis set	ΔE broken-symmetry	ΔE symmetric	Thermal Barrier[a]
cc-pVDZ	0.79	0.45	0.077
aug-cc-pVDZ	0.91	0.58	0.081
cc-pVTZ	0.92	0.59	0.085
aug-cc-pVTZ	0.96	---	---

a) Calculated as the difference in energy between the (X = -1.0) symmetry-broken and (X = 0.0) symmetric configurations

For ωB97, the optimal value (*i.e.*, the value minimizing the MESIE) of the range-separation parameter ω was determined following the IP (ionization potential)-tuning procedure.[49,50] This is done by minimizing the difference between the highest occupied orbital eigenvalue and the computed ΔSCF ionization potential given by Eq. (2.11).

To ensure consistency between the geometries and the IP-tuned ω-values, the geometry relaxation and IP-tuning procedures were iterated until full convergence was obtained. In order to analyze possible starting-point dependencies of the self-consistent geometry optimization/ω-tuning procedure, we employed both the self-consistent HF and B3LYP geometries of the neutral and radical-cation states as geometric starting points. As was shown earlier, the characteristic length of the IP-tuned range separation, 1/ω, grows with the degree of conjugation in the system.[32] For the MV systems studied in this work, it is therefore expected that the optimal

ω value is determined inherently by the electronic coupling between the redox centers. However, it has been demonstrated recently[51] that the dependence of the IP-tuned ω value on system size introduces problems with size-consistency such as the comparison of energies derived from different tuned functionals (*i.e.*, with a different ω value).

For the sake of comparison with previous studies, the broken-symmetry and symmetric (top of the tunneling barrier) geometries of compound $\mathbf{1}^+$ were obtained by imposing C_{2v} and D_{2d} symmetry constraints, respectively. No symmetry constraints were employed for the amine complexes $\mathbf{2}^+$ and $\mathbf{3}^+$. Frequency analyses were performed for all optimized geometries to ensure that a minimum had been reached.

The determination of the fractional particle curves for the evaluation of the MSIE were carried out with a local developers' version of PSI4.[52] Fractional particle curves were carried out using the self-consistent geometries obtained from the methods studied here: ωB97, B3LYP, and HF. The cc-pVDZ basis set was employed for all fractional-electron calculations. For the fractional particle curves of $\mathbf{3}^+$**,** the methoxy groups were substituted by hydrogen atoms.

In order to benchmark the LRC-DFT calculations for $\mathbf{1}^+$ and $\mathbf{2}^+$, we have employed the single-reference equation-of-motion coupled-cluster (EOM-CC) approach, which is among the most accurate methods in calculating excitation energies with typical errors of about 0.1 – 0.3 eV.[53-55] For ionized systems, the EOM-IP-CC is capable of describing accurately both the charge-localized and charge-delocalized systems, yielding accurate charge distributions and energies. In

EOM-IP-CC calculations, a suitable starting reference point is obtained from the neutral HF wave function, which does not suffer from the instability problem. The target ionic wave functions are derived by removing an electron from the reference within a coupled-cluster framework.[56-60] The EOM-IP-CCSD calculations were performed using the QChem *ab initio* package.[61]

4.3. Results and Discussion

4.3.1. Comparison of Results from IP-Tuned DFT with Standard DFT and HF for Class-II Mixed-Valence System

For compound $\mathbf{1}^+$, previous high-level post-HF methods such as charge-renormalization equation-of-motion coupled cluster methods with triple corrections (CR-EOM-CCSD(T)),[22] multireference methods (*e.g.*, complete active space SCF with single and double excitations),[21] and multireference methods combined with a perturbative description[19] have pointed out that the lower potential energy surface corresponds to a double well. Figure 4.2 displays the singly occupied molecular orbital (SOMO) of $\mathbf{1}^+$ as obtained from self-consistent HF and B3LYP geometry optimizations. B3LYP results in the positive charge being symmetrically delocalized over both redox centers (in our experience, the same picture is obtained when using other common semilocal or global hybrid functionals incorporating less than roughly 50% HF exchange, as discussed below). In contrast, HF leads to a localized charge and, thus, to an electronic structure and geometry that, from a qualitative standpoint, are consistent with the results of highly correlated post-HF methods. Importantly, however, for the reasons mentioned in the introduction, neither the B3LYP nor the HF geometries are reliable.

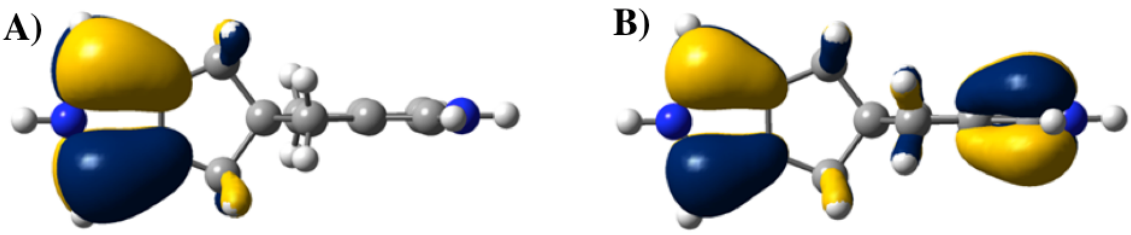

Figure 4.2. Singly occupied molecular orbital (SOMO) plots for the HF (A) and B3LYP (B) cation geometries of $\mathbf{1}^+$ that were subsequently further optimized with IP-tuned ωB97.

The localization/delocalization errors of HF and B3LYP can be quantified based on the total energy curves as a function of fractional particle numbers when going from **1** to $\mathbf{1}^+$. This is illustrated in Figure 4.3, where δ denotes the deviation in fractional number of electrons from the neutral molecule. As the nonlinearity of the approximate fractional particle curves can be hard to gauge with the naked eye, the deviation from linearity of the total energy ΔE(δ) is shown in the inset of Figure 4.3. The integral $e_{MESIE} = \int_{-1}^{0} \Delta E(\delta) d\delta$ quantifies the MESIE upon ionization of the molecule (appearance of a hole in the HOMO). When e_{MESIE} is positive, the MESIE is referred to as a *localization* error, as situations with integer particle numbers are spuriously favored over situations with fractional particle numbers; conversely, a negative e_{MESIE} corresponds to a *delocalization* error.

For $\mathbf{1}^+$, we find a localization error of +0.233 eV for HF and a delocalization error of −0.263 eV for B3LYP. This is consistent with the localized and delocalized nature of the charge displayed in Figure 4.2 for the HF (Figure 4.2.A) and B3LYP (Figure 4.2.B) geometries, respectively. What we learn from these results is that the minimization of the MESIE related to the single ionization of the neutral molecule, hereafter referred to as the HOMO-MESIE, comes as a

necessary condition for functional approximations to allow a reliable prediction of the electronic structure of organic MV systems. To the best of our knowledge, no study to date has discussed MV systems using functionals that are free from HOMO-MESIE.

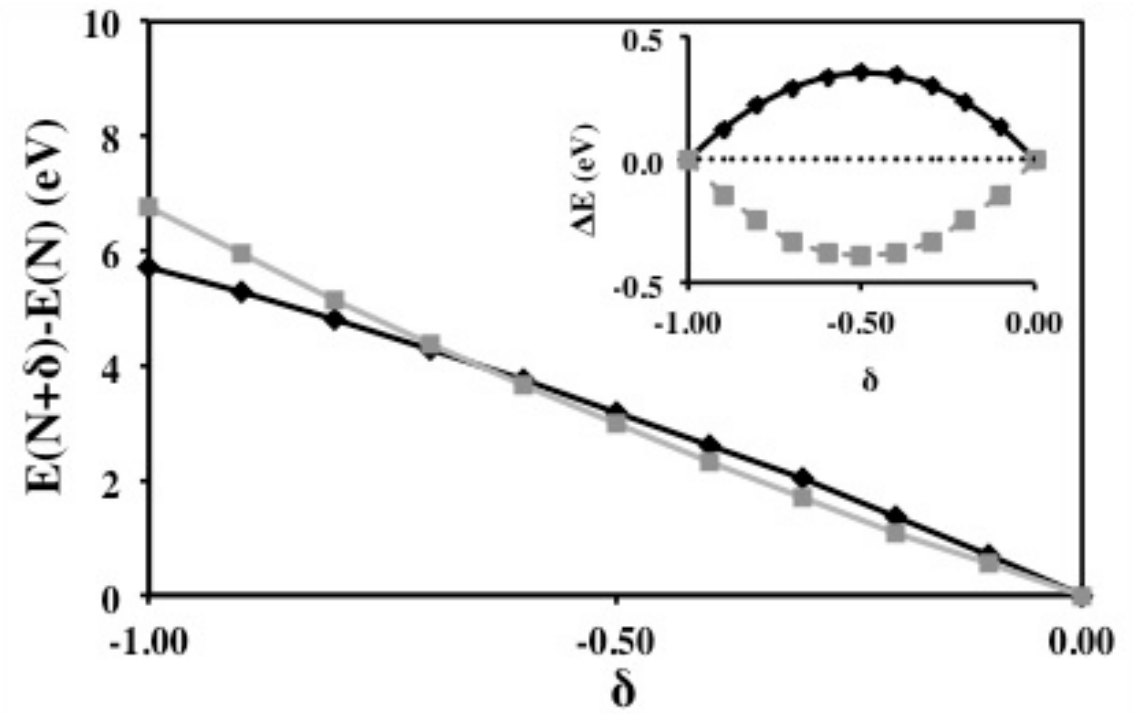

Figure 4.3. Change in relative total energy of $\mathbf{1}^{+}$ as a function of fractional occupation number of the HOMO when going from the neutral molecule ($\delta = 0$) to the cation ($\delta = -1$) for the HF (black) and B3LYP (grey) geometries; the inset shows the deviation ΔE with respect to the straight line connecting the $\delta = 0$ and $\delta = -1$ total-energy values.

As has been demonstrated in several recent publications,[33,34,62] the HOMO-MESIE can be reduced by several orders of magnitude by tuning the range-separation parameter in long-range corrected hybrid functionals on the basis of the nonempirical IP-tuning procedure introduced in Eq. (2.11).This is consistent with the fact that the IP-tuning can be interpreted as a minimization of the MESIE at the HOMO level:[50] As the HOMO eigenvalue equals the slope of the total energy *vs*. occupation number, the IP-tuning guarantees that the initial slope of the total energy

curve at $\delta = 0$, when going from the neutral state to the cation, equals the vertical ionization potential, *i.e.*, the total energy difference between the neutral and cation states.

In this work, we tune the range-separation parameter ω in the long-range corrected hybrid functional ωB97; it is useful to note that, as was found as well in several earlier works that employed various tuned range-separated hybrid functionals,[32,34,63,64] the results are not influenced qualitatively by the specifics of the semilocal approximations for exchange and correlation underlying the functional. Starting from the (broken-symmetry) HF and (symmetrical) B3LYP geometries, we find IP-tuned ω values of 0.139 and 0.161 $Å^{-1}$, respectively, after the iterative procedure (see below). Using these self-consistent geometries and tuned range-separation parameters ω, we obtain the fractional particle curves plotted in Figure 4.4. As expected, the IP-tuning procedure very substantially reduces the HOMO-MESIE, down to $+7.38 \times 10^{-4}$ and $+4.86 \times 10^{-3}$ eV, *i.e.*, several orders of magnitude smaller than what is obtained from B3LYP and HF. These results underline that IP-tuned long-range corrected hybrid functionals can provide a practically HOMO-MESIE-free description of organic MV systems. We now proceed to show that these functionals have the potential to correctly assess the class to which organic MV systems belong.

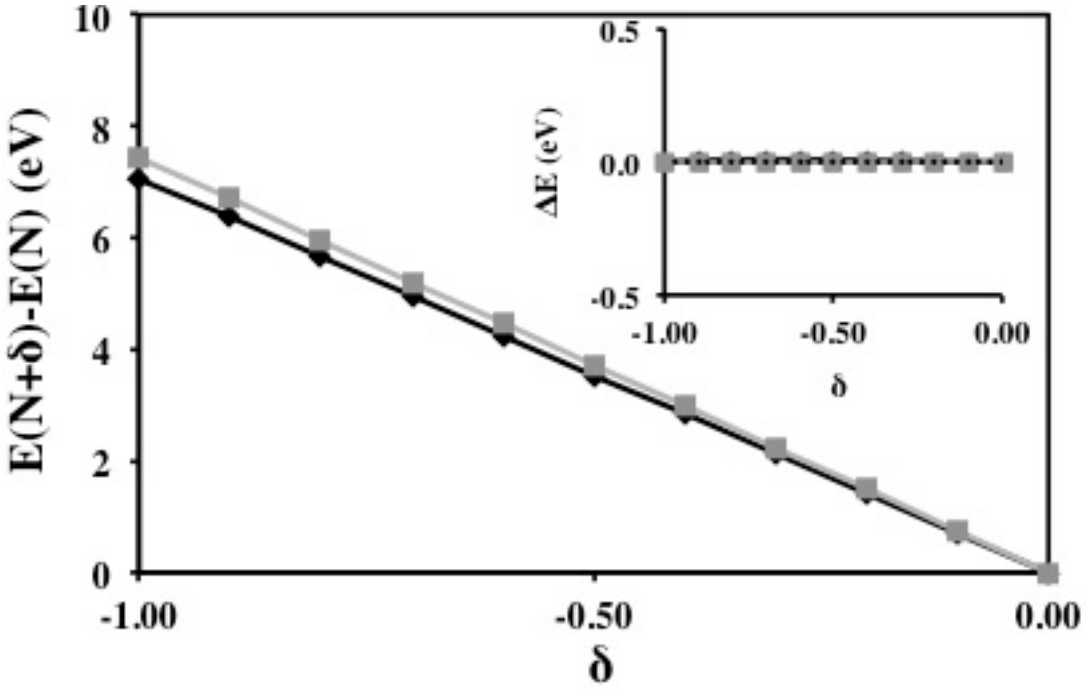

Figure 4.4. Change in relative total energy of $\mathbf{1}^{+}$ as a function of fractional occupation number of the HOMO when going from the neutral molecule ($\delta = 0$) to the cation ($\delta = -1$) using IP-tuned ωB97, and deviation of relative total energy from a straight line (inset). The cation geometries were iteratively optimized with IP-tuned ωB97 starting from the HF (black) and B3LYP (grey) cation geometries.

4.3.2. Many-Electron Self-Interaction Error-Free Tuned Long-Range Corrected Hybrid Functionals

Although the ω-tuning procedure leads to HOMO-MESIE-free results for a given system, a drawback is that, by tuning the ω value, the effective Hamiltonian is changed, which removes the ability to directly compare relative energies that are obtained with different ω values. Also, the IP-tuned ω value itself is system-dependent and evolves during a geometry optimization. Specifically for $\mathbf{1}^+$, the initial tuning procedure leads to ω = 0.140 $Å^{-1}$ for the HF (*i.e.*, broken-symmetry) geometry and ω = 0.162 $Å^{-1}$ for the B3LYP (*i.e.*, symmetric) geometry. This first round of ω-tuning is then followed by an iterative process of alternating geometry optimization and ω-tuning until self-consistency between geometries and ω-values is reached; generally, a single full iteration step is sufficient to obtain this self-consistency. For $\mathbf{1}^+$, this procedure leads to self-consistent ω values of 0.139 $Å^{-1}$ and 0.161 $Å^{-1}$ for the broken-symmetry and symmetric geometries, respectively.

It is interesting to note that the wave function initially found at the symmetric geometry is unstable. Forcing the stability of the wave function (by using the keyword "stable = opt" in Gaussian 09) leads to a symmetry-broken solution (Figure 4.5). In that case, even though the geometry remains symmetric (all C=C double-like bond lengths are identical and equal to 1.409 Å in both pyrrole rings of $\mathbf{1}^+$), the spin density of the unpaired electron is distributed ~ 0.99 over one of the two halves of $\mathbf{1}^+$ (Table 4.2).

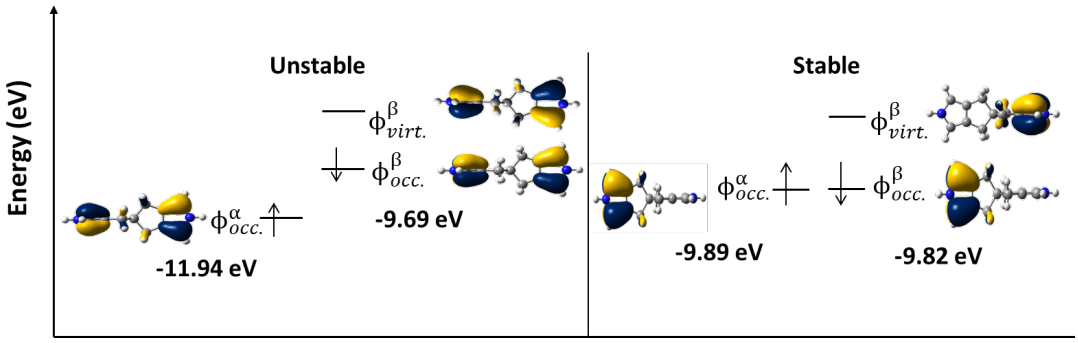

Figure 4.5. Orbital plots for unstable wave function (left) and stable=opt wave function (right) for $\mathbf{1}^{+}$ taken at X= 0.0 along the nuclear coordinate computed for $\omega = 0.139$ Å^{-1}.

Table 4.2. Spin density for segments A and B representing half of the spiro molecule **1**$^{+}$ with corresponding C-C double bond lengths of each geometry.

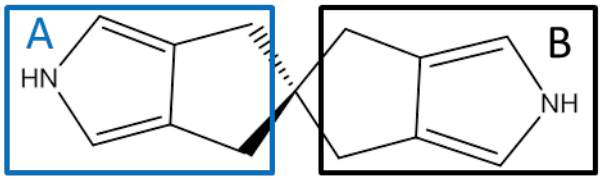

X	Unstable		Stable = opt		Bond length C=C (Å)	
$C_{2v} \rightarrow C_{2v}$ Geom.	Spin density A	Spin density B	Spin density A	Spin density B	A	B
-1	0.01	0.99	0.00	0.99	1.385	1.434
-0.9	0.01	0.99	0.00	0.99	1.387	1.432
-0.8	0.01	0.99	0.00	0.99	1.389	1.429
-0.7	0.01	0.99	0.00	0.99	1.392	1.427
-0.6	0.01	0.99	0.00	0.99	1.394	1.424
-0.5	0.01	0.99	0.00	0.99	1.397	1.422
-0.4	0.01	0.99	0.00	0.99	1.399	1.419
-0.3	0.60	0.40	0.00	0.99	1.402	1.417
-0.2	0.55	0.45	0.00	0.99	1.404	1.414
-0.1	0.50	0.50	0.00	0.98	1.407	1.412
0.0	0.45	0.55	0.98	0.98	1.409	1.409
0.1	0.40	0.60	0.98	0.00	1.412	1.407
0.2	0.99	0.01	0.98	0.00	1.414	1.404
0.3	0.99	0.01	0.99	0.00	1.417	1.402
0.4	0.99	0.01	0.99	0.00	1.419	1.399
0.5	0.99	0.01	0.99	0.00	1.422	1.397
0.6	0.99	0.01	0.99	0.00	1.424	1.394
0.7	0.99	0.01	0.99	0.00	1.427	1.392
0.8	0.99	0.01	0.99	0.00	1.429	1.389
0.9	0.99	0.01	0.99	0.00	1.432	1.387
1	0.99	0.01	0.99	0.00	1.434	1.385
D_{2d}					1.409	1.409

To facilitate a direct comparison to previous studies,[21,22,65] the transition from localized to delocalized geometry was examined for compound $\mathbf{1}^+$ by mapping out the double-well potential energy surface. This is done by mixing the two symmetry-broken geometries according to the equation:

$$Q = 1/2\big((1-X)Q_A + (1+X)Q_B\big), \qquad \textbf{(4.1)}$$

where Q_A and Q_B represent the internal coordinates for the symmetry-broken geometries found to be the degenerate minima (-1.0 and 1.0 on the nuclear coordinate X, respectively), and represent asymmetric distortions from the symmetric geometry at the transition state (0.0 on the nuclear coordinate). The transition between the two localized structures was mapped out in steps of $\Delta X = 0.1$. Note that a relaxed symmetry tolerance is needed to recover the C_{2v} (symmetry-broken) and D_{2d} (symmetric) geometries at all points on the potential energy surface. The results are displayed in Figure 4.6.

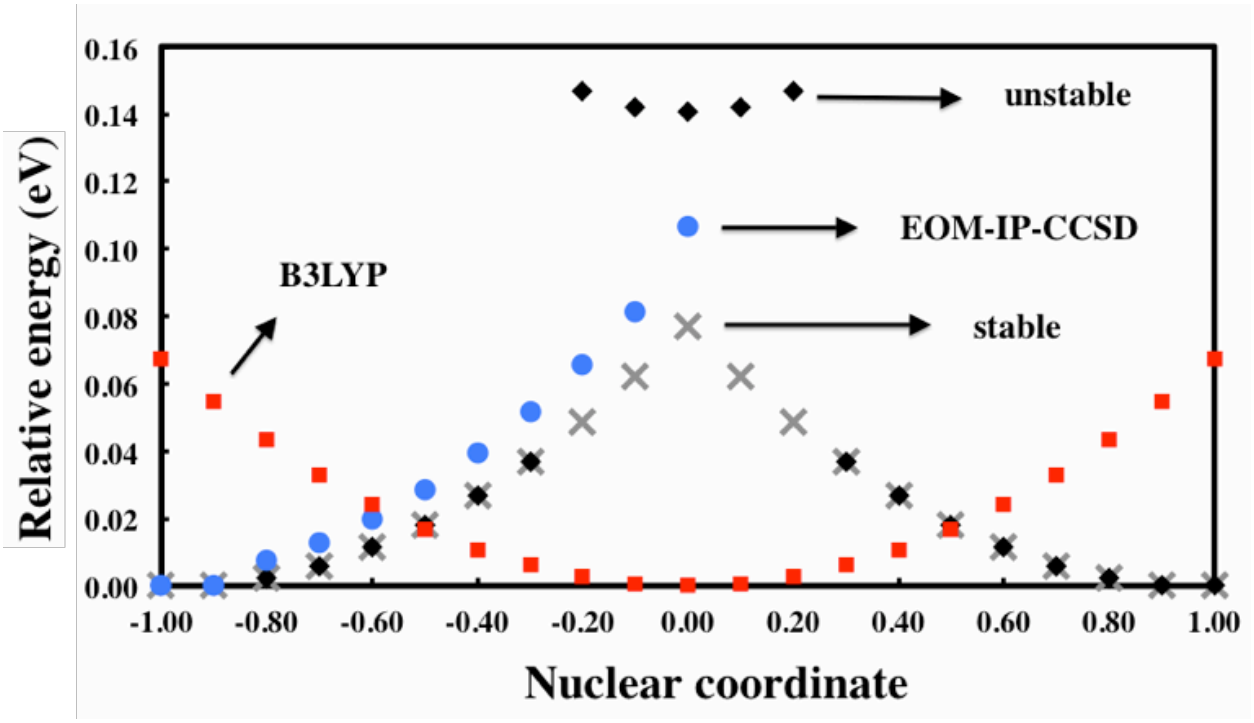

Figure 4.6. Potential energy surface as a function of the nuclear coordinate X representing the linear combination of the symmetry-broken (X = -1.0, 1.0) configurations, as calculated with IP-tuned ωB97 (ω = 0.139 Å^{-1}). Results are given both without inclusion (♦) and with inclusion (×) of the "stable = opt" keyword ensuring stability of the wave function (see text). EOM-IP-CCSD (●) and B3LYP (■) results are also given for comparison.

Interestingly, the issue of wave-function stability arises not only for the top of the barrier but also, as seen from Figure 4.6, for a range of nearby points; as a result, the corresponding potential energy surface displays an unphysical discontinuity. Note also that the stability is not an issue for ω values that are too low, thus resulting in a delocalized picture (similar to what is plotted for B3LYP). For example starting from ω = 0.079 Å^{-1}, $\mathbf{1}^{+}$ is predicted to be a class-III system. If a larger amount of HF exchange is incorporated in the Hamiltonian (about ω = 0.132 Å^{-1}), then the potential energy surface corresponds to a double-well class-II system, with each minimum corresponding to a localized charge on each pyrrole center.

The choice of the ω value (and therefore the amount of HF exchange incorporated) also changes the point along the nuclear coordinate where the spurious step in the potential energy surface occurs. The magnitude of the barrier (*i.e.*, the energy difference between the symmetry-broken minimum and the symmetric maximum) is consequently altered. For a very low ω value, *i.e.*, ω = 0.079 $Å^{-1}$, the symmetric geometry is lower by 0.06 eV, thereby giving a qualitatively similar description to B3LYP. The single-well symmetric potential energy surface (*i.e.*, class-III) changes to a double well (*i.e.*, class-II) at ω = 0.132 $Å^{-1}$, resulting in a symmetric geometry that is now 0.16 eV higher than the symmetry-broken minimum.

In addition to tuning the ω value in ωB97, we also considered a general hybrid GGA functional (B_αLYP) of the form:

$$\alpha E_X^{HF} + (1-\alpha)E_X^{B3} + E_C^{LYP}, \qquad \textbf{(4.2)}$$

with variable amounts of HF exchange (E_X^{HF}) and where the DFT semilocal exchange and correlation functionals E_X^{B3} and E_C^{LYP} are defined here to retrieve the standard B3LYP functional for α = 0.20. Eq. (4.2) is considered to highlight the impact of the amount of HF for a direct comparison with previous publications that have recommended about 35% HF exchange (with implicit consideration of the solvent) in order to improve the description of the MV systems.[20] We note that by tuning the percentage of HF exchange, we can characterize the point when the system changes from class-III to class-II for $\mathbf{1}^+$; this critical point was reached at α = 0.50. This value is larger than the value recommended in previous reports by the authors of Ref. 20, which is likely related to the lack of consideration of solvent in our study; however, it is interesting to note that most standard functionals have been parameterized to have far less HF exchange than needed to give the correct picture even for such a straightforward class-II MV molecule. Importantly, what is seen is that, by varying the amount of HF exchange in a global hybrid, one can obtain either the localized or delocalized picture depending on the amount of HF exchange used. Hence, such a methodology only allows to reproduce a Robin-Day classification that is known *a priori*, but not to predict it from first principles. In contrast, the range-separation parameter in our approach is tuned *non-empirically*, thus, allowing the *prediction* of the Robin-Day classification.

With an understanding of the potential energy surface of $\mathbf{1}^+$ and the effect that the percentage of HF exchange has on the shape of the surface, we can now discuss how the IP-tuned ωB97

functional performs when compared to high-level methods. For IP-tuned ωB97, the estimated energy of the thermal barrier to electron transfer is 0.077 eV, which is obtained as the difference in energy between the (X = -1.0) symmetry-broken and (X = 0.0) symmetric configurations. The EOM-IP-CCSD-calculated ground-state energies follow almost exactly the IP-tuned ωB97 result and leads to a calculated electron transfer barrier of 0.107 eV, thereby giving validation to the reliability of our approach both qualitatively and quantitatively. The LRC-DFT result also compares well with the range of values previously given in the literature: 0.12 – 0.17 eV[22] from multireference perturbation theory and 0.14 eV from ESR data on a similar spiro molecule.[66] The authors or Ref. [22] also reported an electronic coupling between the redox centers of 0.11 eV with the CR-EOM-CCSD(T)/cc-pVTZ method. Although this method is a quantitatively accurate approach with a triple zeta basis set,[67] the authors of Ref. 22 noted that the potential energy surface demonstrated a cusp at X = 0.0 on the nuclear coordinate that could only be remedied by multireference approaches, which show a delocalized charge. In fact, a multireference perturbative (to third order) approach resulted in a better description of the potential energy surface leading to a smooth barrier and gave a coupling of 0.14 eV but a significantly smaller thermal barrier of 0.039 eV.[19] In contrast, several perturbative and multireference methods with single and double excitations provide a coupling value around 0.052 eV[21] and a thermal barrier of 0.069[21] and 0.086 eV.[19]

Here, we calculate the electronic coupling as half the transition energy between the ground state and the first excited state of $\mathbf{1}^+$ at the barrier on the potential energy surface. Our estimate of 0.22 eV, determined with TD-DFT (at the IP-tuned ωB97 level) is in reasonable agreement with the high-level estimates, see Table 4.3. While the B3LYP-calculated electronic coupling (0.23 eV)

also compares similarly with the high-level calculations, B3LYP geometry optimization results in a class-III system for $\mathbf{1}^+$, which highlights the unreliability of this method.

Table 4.3. Time-Dependent DFT, charge renormalization (CR)-CCSD(T), EOM-IP-CCSD, ωB97 ΔSCF, and Koopmans' theorem lowest vertical excitation energies (ΔE) and electronic couplings (t) for compound $\mathbf{1}^+$. All energy values are in eV.

Method	ΔE	Electronic Coupling (t = ΔE/2)
TD-DFT (B3LYP)	0.46	0.23
TD-DFT (IP-tuned ωB97[a])	0.45	0.22
CR-EOM-CCSD(T)/cc-pVTZ[b]	0.22	0.11
EOM-IP-CCSD	0.10	0.05
ΔSCF (IP-tuned ωB97[a])	0.14	0.07
KT (IP-tuned ωB97[a])	0.12	0.06

a) ω = 0.139 $Å^{-1}$
b) Ref. 22

Further analysis for t from Koopmans' theorem using IP-tuned ωB97 (KT, *i.e.*, the HOMO and HOMO-1 energy difference at the ground-state neutral geometry) gives a value of 0.062 eV. Additionally, a third method used to calculate electronic coupling is based on the energy difference of the ground and first excited states of $\mathbf{1}^+$ at the symmetric configuration (ΔSCF approach), which results in an energy separation of $2t$ = 0.136 eV. Therefore, it can be seen that the electronic couplings based on KT and ΔSCF have a much lower value than the electronic coupling based on TD-DFT at the $\mathbf{1}^+$ symmetric geometry.

We now turn to a discussion of the reorganization energy (λ). To estimate λ, we perform TD-DFT at the symmetry-broken structure (X = 0.0, Eq.(4.1), which results in a value of 0.79 eV. Therefore, the criterion of having λ (0.79 eV) > 2*t* (0.44 eV) for a RD class-II system is satisfied for $\mathbf{1}^+$. It should be noted that although HF gives the qualitatively correct picture for $\mathbf{1}^+$, the excitation energy (computed through configuration interaction singles [CIS]) results in a much overestimated value of 2.48 eV when compared to the IP-tuned ωB97 result, which is indicative of too localized an electronic structure for the symmetry-broken configuration. To conclude for $\mathbf{1}^+$, the classification and the microscopic parameters discussed here are consistent with previous studies on this molecule,[19,21,22,65,68] indicating that it belongs to class-II.

4.3.3. Comparison of Results for IP-Tuned DFT with Standard DFT and HF for a Class-III Mixed-Valence System

We now consider compound $\mathbf{2}^+$ that represents a prototypical class-III MV system. As in the case of $\mathbf{1}^+$, $\mathbf{2}^+$ is initially optimized with HF and B3LYP. Both optimizations yield symmetric geometries with the charge delocalized over the entire molecule, see Figure 4.7.A and Figure 4.7.B. The self-consistent geometry-optimization and ω-tuning procedures with ωB97, when starting from the HF and B3LYP geometries, give optimal ω values of 0.129 and 0.128 $Å^{-1}$, respectively. The IP-tuned-ωB97 results also lead to a completely delocalized SOMO (Figure 4.7.C), with an adiabatic energy surface for the cation state consistent with previous studies.[12]

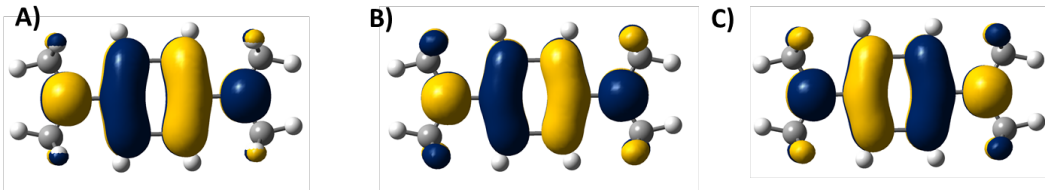

Figure 4.7. SOMO wave functions for the HF (A), B3LYP (B), and IP-tuned ωB97 (C) optimized geometries of $\mathbf{2}^{+}$.

Thus, taking $\mathbf{2}^{+}$ to be class-III, the electronic coupling between redox centers is determined as half the excitation energy at the minimum of the potential energy surface, using time-dependent (TD) DFT or CIS, see Table 4.4. The calculated electronic couplings compare well with experiment for IP-tuned-ωB97 (ω = 0.129 $Å^{-1}$) and B3LYP, and are slightly lower than that obtained with CIS. Both the gas-phase UPS and the solution-based UV-Vis experiments confirm the class-III classification of $\mathbf{2}^{+}$, demonstrating the large electronic coupling between the two redox sites.

Table 4.4. TD-DFT, configuration-interaction singles (CIS), and EOM-IP-CCSD vertical excitation energies (ΔE) for $\mathbf{2}^{+}$. The electronic couplings (t) are evaluated as half the transition energies and compared to experimental UV-Vis and UPS results. All energy values are in eV.

Method	ΔE	Electronic Coupling (t = ΔE/2)
TD-DFT (B3LYP)	2.33	1.16
CIS (HF)	2.87	1.43
TD-DFT (IP-tuned ω B97[a])	2.37	1.18
EOM-IP-CCSD	2.56	1.28
Exp. UV-Vis	2.00	1.00[b]
Exp. UPS	---	0.79[c]

a) $\omega = 0.129$ Å^{-1}
b) Calculated assuming the cation to be a class-III system using $t = E_{opt}/2$ for data acquired in CH_2Cl_2 from Ref. 12
c) From Ref. 12

4.3.4. Comparison of IP-tuned DFT with Standard DFT and HF for a Borderline Class-II/Class-III Mixed-Valence System

With the demonstration that the approach developed here works well for clear-cut class-II and class-III examples, we now turn to compound $\mathbf{3}^+$ that represents a borderline class-II/class-III MV system in the gas phase. For $\mathbf{3}^+$, HF yields a broken-symmetry ground-state geometry with the excess charge localized on one of the triarylamine redox centers, whereas B3LYP gives a delocalized picture (Figure 4.8.A and Figure 4.8.B). This trend is also reflected in the optimized ω value at the ωB97 level when constraining the system to the HF geometry (0.087 $Å^{-1}$), which is surprisingly close to what is obtained for the B3LYP geometry (0.086 $Å^{-1}$). The fully IP-tuned ωB97 result starting from either the HF or B3LYP geometry gives a completely delocalized SOMO (Figure 4.8.C), thereby converting the valence-localized HF geometry to a delocalized geometry with an optimal ω value of 0.085 $Å^{-1}$ while minimizing the MESIE of the HF and B3LYP results (Figure 4.9). This evolution is also seen in the bond-length difference between the C-N bonds along the backbone, which presents a difference of 0.016 Å for the HF geometry but goes to zero in the IP-optimized ωB97 and B3LYP geometries.

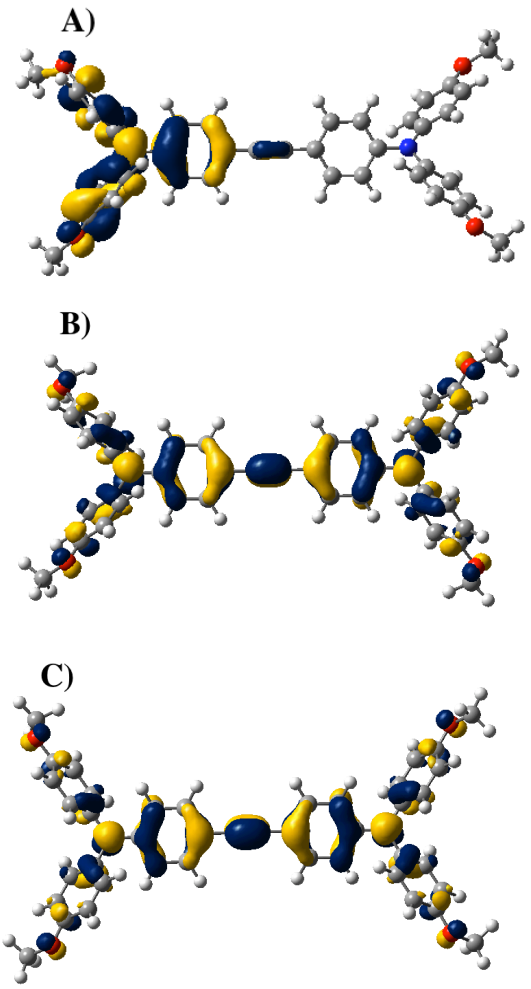

Figure 4.8. SOMO wave functions for the HF (A), B3LYP (B), and IP-tuned ωB97 (C) optimized cation geometries of $\mathbf{3}^{+}$.

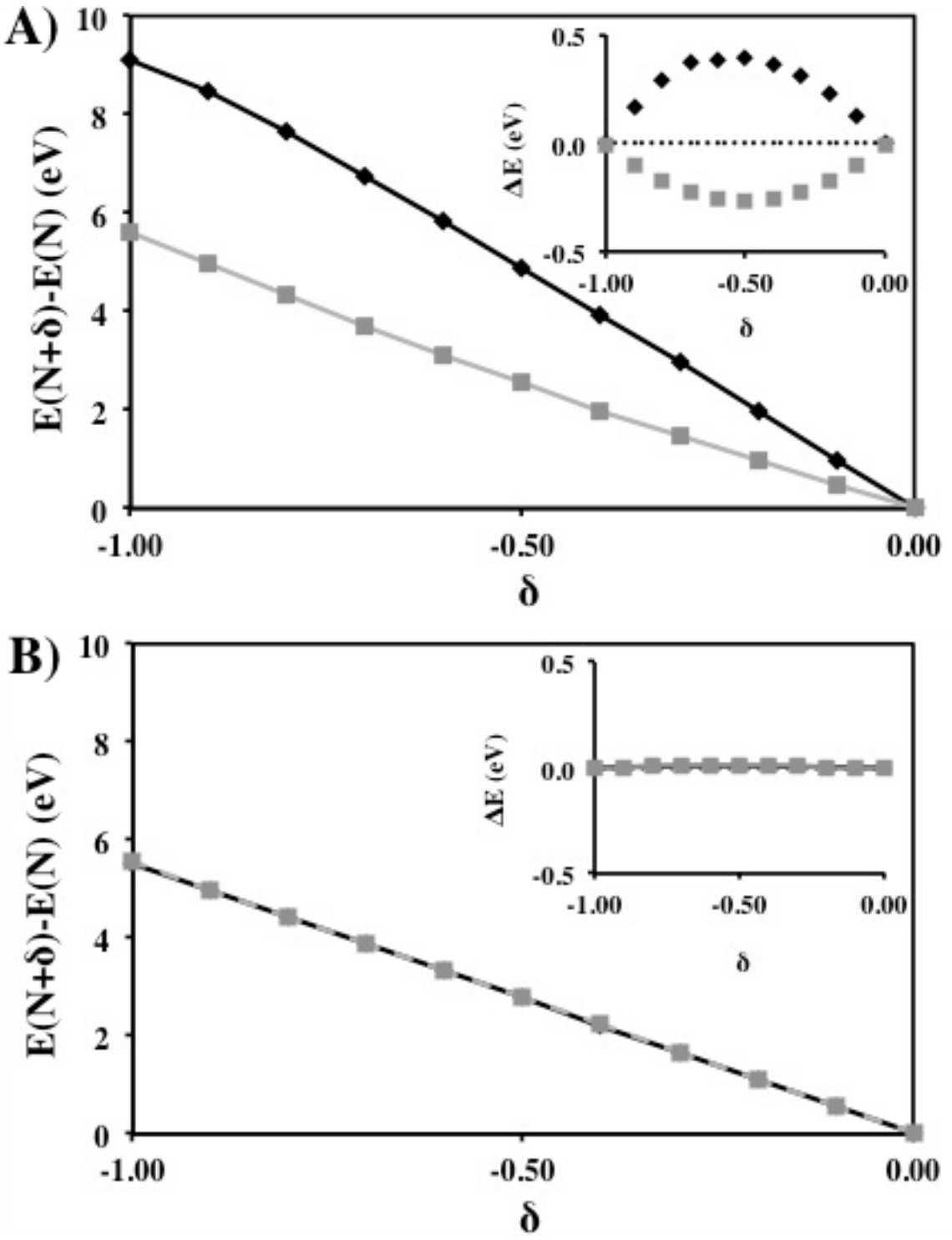

Figure 4.9. Change in relative energy as a function of fractional occupation number of the HOMO when going from the cation (δ = -1) to the neutral molecule (δ = 0) for the HF (black) and B3LYP (grey) cation geometries of $\mathbf{3}^{+}$ (A); these geometries were subsequently further optimized with IP-tuned ωB97 (B). Deviation of relative energy from straight line (insets).

In analogy to the fact that the HF results provide at first sight a qualitatively correct description of the symmetry-broken compound $\mathbf{1}^+$, B3LYP would appear to give an appropriate qualitative picture for the symmetric compound $\mathbf{3}^+$; however, B3LYP still displays a significant HOMO-MESIE of −0.178 eV while the HF error is +0.264 eV (Figure 4.9.A). The IP-tuning procedure reduces the HOMO-MESIE to about $+5.2 \times 10^{-3}$ eV for both geometries (Figure 4.9.B). These results underline that the methodology followed in the present work should provide a reliable assessment of charge (de)localization in organic MV systems, even in instances where the experimental data are not unambiguous.

As highlighted by the fact that conflicting experimental reports exist for a number of systems, the characterization of the degree of charge (de)localization is a complex problem. For example, previous experimental UV-Vis results for $\mathbf{3}^+$ show an asymmetric band in the near-IR region,[3] which would be indicative of a class-III system exhibiting strong coupling of the electron-transfer process to symmetrical vibrations.[6] On the other hand, $\mathbf{3}^+$ displays a significant solvatochromism as well as the presence of an alkyne stretch in the IR spectrum, indicative of a broken symmetry.[11,35]

To better understand the nature of the electronic coupling between the redox centers, we performed TD-DFT calculations on $\mathbf{3}^+$. For the optimized isolated cation, the first transition energy is calculated to be 0.77 eV, which is fully consistent with the absorption peak energies in the UV-Vis spectrum (0.77 eV), see Table 4.5. To compare directly with experimental

conditions, we performed TD-DFT calculations on $\mathbf{3}^+$ with the inclusion of a solvent model. In fact, disparate results were obtained depending on the solvent model chosen; a detailed discussion of these results clearly goes beyond the scope of this article. However, these results demonstrate that even small details in the characteristics of the solvation model can become decisive for borderline class-II/class-III MV systems. Therefore, it is important to distinguish clearly between the effects of the solvation model and the effects of the underlying electronic-structure methods. Only by using an electronic-structure method that is free from localization/delocalization errors and, as a result, that is capable of distinguishing between class-II and class-III MV systems in the gas phase, can we avoid a possible fortuitous cancellation (or amplification) of errors. This is clearly necessary if we want to analyze the performance of different solvation models for MV systems.

Table 4.5. TD-DFT or CIS vertical excitation energies (ΔE) and electronic couplings (t) for compound $\mathbf{3}^+$ obtained from various methods. All values in eV.

Method	ΔE	Electronic Coupling (t = ΔE/2)
TD-DFT (B3LYP)	0.81	0.40
CIS (HF)	3.3	---[b]
TD-DFT (IP-tuned ωB97[a])	0.77	0.38
Exp. UV-Vis	0.77	0.38[c]

a) $\omega = 0.085$ Å^{-1}
b) Broken-symmetry-structure
c) Calculated assuming the cation to be class-III systems using $t = E_{opt}/2$ for data acquired in CH_2Cl_2 from Ref. [3]

4.4. Conclusions

We have developed a reliable methodology for describing the charge localization / delocalization character of organic mixed-valence systems by employing an IP-tuned long-range corrected functional. Our findings demonstrate that such IP-tuned long-range corrected functionals provide a MESIE-free approach that, in contrast to standard DFT functionals and HF, can reliably describe both localized and delocalized organic MV systems based on intrinsic factors that determine the nature of coupling between redox centers in MV systems.

Importantly, by having in hand a robust method capable of handling static charge-delocalized and localized MV compounds, the electronic structure can be predicted in instances where the experimental data are ambiguous. We thus believe that the work presented here can have a broad applicability in the field of organic MV systems. As a next step, it will be important to address the reliability of adding solvation models, since in a number of instances the nature of the solvent determines whether a borderline system falls into either class-II or class-III.

4.5. References

1. Robin, M. B.; Day, P. *Advances in Inorganic Chemistry and Radiochemistry*; Academic Press: Waltham, U.S.A, 1967.
2. Nelsen, S. F.; Ismagilov, R. F.; Powell, D. R. Charge Localization in a Dihydrazine Analogue of Tetramethyl-p-phenylenediamine Radical Cation. *Journal of the American Chemical Society.* **1996**, *118*, 6313-6314.
3. Lambert, C.; Nöll, G. The Class II/III Transition in Triarylamine Redox Systems. *Journal of the American Chemical Society.* **1999**, *121*, 8434-8442.
4. Nelsen, S. F. "Almost Delocalized" Intervalence Compounds. *Chem. Eur. J.* **2000**, *6*, 581-588.
5. Coropceanu, V.; Malagoli, M.; André, J. M.; Brédas, J. L. Intervalence Transition in Triarylamine Mixed-Valence Systems: A Time-Dependent Density Functional Theory Study. *The Journal of Chemical Physics* **2001**, *115*, 10409-10416.
6. Coropceanu, V.; Malagoli, M.; André, J. M.; Bredas, J. L. Charge-Transfer Transitions in Triarylamine Mixed-Valence Systems: A Joint Density Functional Theory and Vibronic Coupling Study. *Journal of the American Chemical Society.* **2002**, *124*, 10519-10530.
7. Coropceanu, V.; Lambert, C.; Nöll, G.; Bredas, J. L. Charge-Transfer Transitions in Triarylamine Mixed-Valence Systems: the Effect of Temperature. *Chemical Physics Letters* **2003**, *373*, 153-160.
8. Coropceanu, V.; Gruhn, N. E.; Barlow, S.; Lambert, C.; Durivage, J. C.; Bill, T. G.; Nöll, G.; Marder, S. R.; Bredas, J. L. Electronic Couplings in Organic Mixed-Valence Compounds: The Contribution of Photoelectron Spectroscopy. *Journal of the American Chemical Society.* **2004**, *126*, 2727-2731.
9. Szeghalmi, A. V.; Erdmann, M.; Engel, V.; Schmitt, M.; Amthor, S.; Kriegisch, V.; Nöll, G.; Stahl, R.; Lambert, C.; Leusser, D.; Stalke, D.; Zabel, M.; Popp, J. How Delocalized Is N,N,N‘,N‘-Tetraphenylphenylenediamine Radical Cation? An Experimental and Theoretical Study on the Electronic and Molecular Structure. *Journal of the American Chemical Society.* **2004**, *126*, 7834-7845.
10. Lambert, C.; Amthor, S.; Schelter, J. From Valence Trapped to Valence Delocalized by Bridge State Modification in Bis(triarylamine) Radical Cations: Evaluation of Coupling Matrix Elements in a Three-Level System. *Journal of Physical Chemistry A* **2004**, *108*, 6474-6486.
11. Barlow, S.; Risko, C.; Chung, S.-J.; Tucker, N. M.; Coropceanu, V.; Jones, S. C.; Levi, Z.; Bredas, J. L.; Marder, S. R. Intervalence Transitions in the Mixed-Valence Monocations of Bis(triarylamines) Linked with Vinylene and Phenylene−Vinylene Bridges. *Journal of the American Chemical Society.* **2005**, *127*, 16900-16911.
12. Risko, C.; Coropceanu, V.; Barlow, S.; Geskin, V.; Schmidt, K.; Gruhn, N. E.; Marder, S. R.; Bredas, J. L. Trends in Electron-Vibration and Electronic Interactions in Bis(dimethylamino) Mixed-Valence Systems: A Joint Experimental and Theoretical Investigation. *Journal of Physical Chemistry C* **2008**, *112*, 7959-7967.
13. Nelsen, S. F.; Schultz, K. P. Electron Transfer within Charge-Localized Arylhydrazine-Centered Mixed Valence Radical Cations Having Larger Bridges. *Journal of Physical Chemistry A* **2009**, *113*, 5577-5584.
14. Lancaster, K.; Odom, S. A.; Jones, S. C.; Thayumanavan, S.; Marder, S. R.; Bredas, J. L.; Coropceanu, V.; Barlow, S. Intramolecular Electron-Transfer Rates in Mixed-Valence

Triarylamines: Measurement by Variable-Temperature ESR Spectroscopy and Comparison with Optical Data. *Journal of the American Chemical Society.* **2009**, *131*, 1717-1723.
15. Creutz, C. *Progress in Inorganic* Chemistry, John Wiley & Sons, Inc: Hoboken, U.S.A., 1983.
16. Crutchley, R. J. *Advances in Inorganic Chemistry*; Academic Press: Waltham, U.S.A., 1994.
17. Hush, N. S. Homogeneous and Heterogeneous Optical and Thermal Electron Transfer. *Electrochim. Acta* **1968**, *13*, 1005-1023.
18. Hoekstra, R. M.; Telo, J. P.; Wu, Q.; Stephenson, R. M.; Nelsen, S. F.; Zink, J. I. Solvent Effects on the Coexistence of Localized and Delocalized 4,4′-Dinitrotolane Radical Anion by Resonance Raman Spectroscopy. *Journal of the American Chemical Society.* **2010**, *132*, 8825-8827.
19. Pastore, M.; Helal, W.; Evangelisti, S.; Leininger, T.; Malrieu, J. P.; Maynau, D.; Angeli, C.; Cimiraglia, R. Can the Second Order Multireference Perturbation Theory be Considered a Reliable Tool to Study Mixed-Valence Compounds? *The Journal of Chemical Physics* **2008**, *128*, 174102-174109.
20. Renz, M.; Theilacker, K.; Lambert, C.; Kaupp, M. A Reliable Quantum-Chemical Protocol for the Characterization of Organic Mixed-Valence Compounds. *Journal of the American Chemical Society.* **2009**, *131*, 16292-16302.
21. Helal, W.; Evangelisti, S.; Leininger, T.; Maynau, D. Ab-Initio Multireference Study of an Organic Mixed-Valence Spiro Molecular System. *J. Comput. Chem.* **2009**, *30*, 83-92.
22. Glaesemann, K. R.; Govind, N.; Krishnamoorthy, S.; Kowalski, K. EOMCC, MRPT, and TDDFT Studies of Charge Transfer Processes in Mixed-Valence Compounds: Application to the Spiro Molecule. *Journal of Physical Chemistry A* **2010**, *114*, 8764-8771.
23. Kaupp, M.; Renz, M.; Parthey, M.; Stolte, M.; Wurthner, F.; Lambert, C. Computational and Spectroscopic Studies of Organic Mixed-Valence Compounds: Where is the Charge? *Physcial Chemistry Chemical Physics* **2011**, *13*, 16973-16986.
24. Renz, M.; Kaupp, M. Predicting the Localized/Delocalized Character of Mixed-Valence Diquinone Radical Anions. Toward the Right Answer for the Right Reason. *Journal of Physical Chemistry A* **2012**, *116*, 10629-10637.
25. Perdew, J. P.; Zunger, A. Self-Interaction Correction to Density-Functional Approximations for Many-Electron Systems. *Physical Review B* **1981**, *23*, 5048-5079.
26. Cohen, A. J.; Mori-Sánchez, P.; Yang, W. Challenges for Density Functional Theory. *Chemical Reviews***2011**, *112*, 289-320.
27. Mori-Sánchez, P.; Cohen, A. J.; Yang, W. Localization and Delocalization Errors in Density Functional Theory and Implications for Band-Gap Prediction. *Physical Review Letters* **2008**, *100*, 146401-1–146401-4.
28. Cohen, A. J.; Mori-Sánchez, P.; Yang, W. Insights into Current Limitations of Density Functional Theory. *Science* **2008**, *321*, 792-794.
29. Ruzsinszky, A.; Perdew, J. P.; Csonka, G. I.; Vydrov, O. A.; Scuseria, G. E. Spurious Fractional Charge on Dissociated Atoms: Pervasive and Resilient Self-Interaction Error of Common Density Functionals. *The Journal of Chemical Physics* **2006**, *125*, 194112-194118.
30. Mori-Sánchez, P.; Cohen, A. J.; Yang, W. Many-Electron Self-Interaction Error in Approximate Density Functionals. *The Journal of Chemical Physics* **2006**, *125*, 201102-201104.

31. Perdew, J. P.; Parr, R. G.; Levy, M.; Balduz, J. L., Jr. Density-Functional Theory for Fractional Particle Number: Derivative Discontinuities of the Energy. *Physical Review Letters* **1982**, *49*, 1691-1694.
32. Körzdörfer, T.; Sears, J. S.; Sutton, C.; Bredas, J. L. Long-Range Corrected Hybrid Functionals for Pi-Conjugated Systems: Dependence of the Range-Separation Parameter on Conjugation Length. *The Journal of Chemical Physics* **2011**, *135*, 204107-204106.
33. Körzdörfer, T.; Parrish, R. M.; Sears, J. S.; Sherrill, C. D.; Bredas, J. L. On the Relationship Between Bond-Length Alternation and Many-Electron Self-Interaction Error. *The Journal of Chemical Physics* **2012**, *137*, 124305-124308.
34. Körzdörfer, T.; Parrish, R. M.; Marom, N.; Sears, J. S.; Sherrill, C. D.; Bredas, J. L. Assessment of the Performance of Tuned Range-Separated Hybrid Density Functionals in Predicting Accurate Quasiparticle Spectra. *Physical Review B* **2012**, *86*, 205110-1–205110-9.
35. Barlow, S.; Risko, C.; Coropceanu, V.; Tucker, N. M.; Jones, S. C.; Levi, Z.; Khrustalev, V. N.; Antipin, M. Y.; Kinnibrugh, T. L.; Timofeeva, T.; et al. A Mixed-Valence Bis(diarylamino)stilbene: Crystal Structure and Comparison of Electronic Coupling with Biphenyl and Tolane Analogues. *Chem. Commun.* **2005**, 764-766.
36. Nelsen, S. F. *Advances in Physical Organic Chemistry*; Academic Press: Waltham, U.S.A., 2006.
37. Nelsen, S. F.; Chang, H.; Wolff, J. J.; Adamus, J. Polycyclic Bis(hydrazine) and Bis(hydrazyl) Radical Cations: High and Low Inner-Sphere Reorganization Energy Organic Intervalence Compounds. *Journal of the American Chemical Society.* **1993**, *115*, 12276-12289.
38. Nelsen, S. F.; Tran, H. Q.; Nagy, M. A. Comparison of V Values for Some Nitrogen- and Metal-Centered π-Bridged Mixed-Valence Compounds. *Journal of the American Chemical Society.* **1998**, *120*, 298-304.
39. Nöll, G.; Avola, M. Optically Induced Electron Transfer in an N,N,N′,N′-tetraanisyl-o-phenylenediamine Radical Cation. *J. Phys. Org. Chem.* **2006**, *19*, 238-241.
40. Low, P. J.; Paterson, M. A. J.; Goeta, A. E.; Yufit, D. S.; Howard, J. A. K.; Cherryman, J. C.; Tackley, D. R.; Brown, B. The Molecular Structures and Electrochemical Response of "Twisted" Tetra(aryl)benzidenes. *Journal of Materials Chemistry* **2004**, *14*, 2516-2523.
41. Low, P. J.; Paterson, M. A. J.; Yufit, D. S.; Howard, J. A. K.; Cherryman, J. C.; Tackley, D. R.; Brook, R.; Brown, B. Towards an Understanding of Structure-Property Relationships in Hole-Transport Materials: The Influence of Molecular Conformation on Oxidation Potential in Poly(aryl)amines. *Journal of Materials Chemistry* **2005**, *15*, 2304-2315.
42. Chiu, K. Y.; Su, T.H.; Huang, C. W.; Liou, G.-S.; Cheng, S.H. Substituent Effects on the Electrochemical and Spectral Characteristics of N,N,N′,N′-tetraaryl-p-phenylenediamine Derivatives. *J. Electroanal. Chem.* **2005**, *578*, 283-287.
43. Frisch, M. J.; Trucks, G. W.; Schlegel, H. B.; Scuseria, G. E.; Robb, M. A.; Cheeseman, J. R.; Scalmani, G.; Barone, V.; Mennucci, B.; Petersson, G. A.; et al.: Gaussian 09, Revision B.01. Gaussian, Inc.: Wallingford CT, 2009.
44. Lee, C.; Yang, W.; Parr, R. G. Development of the Colle-Salvetti Correlation-Energy Formula into a Functional of the Electron Density. *Physical Review B* **1988**, *37*, 785-789.
45. Becke, A. D. Density-Functional Thermochemistry. III. The Role of Exact Exchange. *The Journal of Chemical Physics* **1993**, *98*, 5648-5652.

46. Stephens, P. J.; Devlin, F. J.; Chabalowski, C. F.; Frisch, M. J. Ab Initio Calculation of Vibrational Absorption and Circular Dichroism Spectra Using Density Functional Force Fields. *Journal of Physical Chemistry* **1994**, *98*, 11623-11627.
47. Chai, J. D.; Head-Gordon, M. Systematic Optimization of Long-Range Corrected Hybrid Density Functionals. *The Journal of Chemical Physics* **2008**, *128*, 084106-1–084106-15.
48. Kendall, R. A; Dunning Jr., T. H.; Harrison, R. J. Electron Affinities of the First-Row Atoms Revisited. Systematic Basis Sets and Wave Functions. *The Journal of Chemical Physics* **1992**, *96*, 6796-6806.
49. Stein, T.; Kronik, L.; Baer, R. Reliable Prediction of Charge Transfer Excitations in Molecular Complexes Using Time-Dependent Density Functional Theory. *Journal of the American Chemical Society.* **2009**, *131*, 2818-2820.
50. Baer, R.; Livshits, E.; Salzner, U. Tuned Range-Separated Hybrids in Density Functional Theory. *Annu. Rev. Phys. Chem.* **2010**, *61*, 85-109.
51. Karolewski, A.; Kronik, L.; Kummel, S. Using Optimally Tuned Range Separated Hybrid Functionals in Ground-state Calculations: Consequences and Caveats. *The Journal of Chemical Physics* **2013**, *138*, 204115-1–204115-11.
52. Turney, J. M.; Simmonett, A. C.; Parrish, R. M.; Hohenstein, E. G.; Evangelista, F. A.; Fermann, J. T.; Mintz, B. J.; Burns, L. A.; Wilke, J. J.; Abrams, M. L.; et al. *WIREs Comput. Mol. Sci. 2* **2012**, *4*, 556-565.
53. Purvis III, G. D.; Bartlett, R. J. A Full Coupled-Cluster Singles and Doubles Model: The Inclusion of Disconnected Triples. *The Journal of Chemical Physics* **1982**, *76*, 1910-1918.
54. Kallay, M.; Gauss, J. Calculation of Excited-State Properties using General Coupled-cluster and Configuration-Interaction Models. *The Journal of Chemical Physics* **2004**, *121*, 9257-9269.
55. Schreiber, M.; Silva-Junior, M. R.; Sauer, S. P. A.; Thiel, W. Benchmarks for Electronically Excited States: CASPT2, CC2, CCSD, and CC3. *The Journal of Chemical Physics* **2008**, *128*, 134110-1–134110-25.
56. Sinha, D.; Mukhopadhyay, S.; Mukherjee, D. A Note on the Direct Calculation of Excitation Energies by Quasi-Degenerate MBPT and Coupled-Cluster Theory. *Chemical Physics Letters* **1986**, *129*, 369-374.
57. Pal, S.; Rittby, M.; Bartlett, R. J.; Sinha, D.; Mukherjee, D. Multireference Coupled-cluster Methods using an Incomplete Model Space: Application to Ionization Potentials and Excitation Energies of Formaldehyde. *Chemical Physics Letters* **1987**, *137*, 273-278.
58. Sinha, D.; Mukhopadhyay, S. K.; Chaudhuri, R.; Mukherjee, D. The Eigenvalue-Independent Partitioning Technique in Fock Space: An Alternative Route to Open-Shell Coupled-Cluster Theory for Incomplete Model Spaces. *Chemical Physics Letters* **1989**, *154*, 544-549.
59. Stanton, J. F.; Gauss, J. Analytic Energy Derivatives for Ionized States Described by the Equation-of-Motion Coupled Cluster Method. *The Journal of Chemical Physics* **1994**, *101*, 8938-8944.
60. Stanton, J. F.; Gauss, J. A Simple Scheme for the Direct Calculation of Ionization Potentials with Coupled-Cluster Theory that Exploits Established Excitation Energy Methods. *The Journal of Chemical Physics* **1999**, *111*, 8785-8788.
61. Shao, Y.; Molnar, L. F.; Jung, Y.; Kussmann, J.; Ochsenfeld, C.; Brown, S. T.; Gilbert, A. T. B.; Slipchenko, L. V.; Levchenko, S. V.; O'Neill, D. P.; et al. Advances in Methods and Algorithms in a Modern Quantum Chemistry Program Package. *Physcial Chemistry Chemical Physics* **2006**, *8*, 3172-3191.

62. Srebro, M.; Autschbach, J. Does a Molecule-Specific Density Functional Give an Accurate Electron Density? The Challenging Case of the CuCl Electric Field Gradient. *Journal of Physical Chemistry Lett.* **2012**, *3*, 576-581.
63. Sears, J. S.; Körzdörfer, T.; Zhang, C. R.; Bredas, J. L. Communication: Orbital Instabilities and Triplet States from Time-Dependent Density Functional Theory and Long-Range Corrected Functionals. *The Journal of Chemical Physics* **2011**, *135*, 151103-151104.
64. Pandey, L.; Doiron, C.; Sears, J. S.; Bredas, J. L. Lowest Excited States and Optical Absorption Spectra of Donor-Acceptor Copolymers for Organic Photovoltaics: a New Picture Emerging from Tuned Long-Range Corrected Density Functionals. *Physcial Chemistry Chemical Physics* **2012**, *14*, 14243-14248.
65. Farazdel, A.; Dupuis, M.; Clementi, E.; Aviram, A. Electric-Field Induced Intramolecular Electron-Transfer in Spiro π-Electron System and Their Suitability as Molecular Electronic Devices-A Theoretical-Study. *Journal of the American Chemical Society.* **1990**, *112*, 4206-4214.
66. Hirao, Y.; Urabe, M.; Ito, A.; Tanaka, K. Intramolecular Spin Transfer in a Spiro-Fused Bis(triarylamine). *Angewandte Chemie International Edition* **2007**, *46*, 3300-3303.
67. Lopata, K.; Reslan, R.; Kowalska, M.; Neuhauser, D.; Govind, N.; Kowalski, K. Excited-State Studies of Polyacenes: A Comparative Picture Using EOMCCSD, CR-EOMCCSD(T), Range-Separated (LR/RT)-TDDFT, TD-PM3, and TD-ZINDO. *Journal of Chemical Theory and Computation* **2011**, *7*, 3686-3693.
68. Dehareng, D.; Dive, G.; Moradpour, A. Ab Initio Study of Organic Mixed Valency. *International Journal of Quantum Chemistry* **2000**, *76*, 552-573.

Chapter 5 Rigorously Modeling Charge Delocalization in Finite Clusters

5.1. Introduction

Although the actual charge-transport mechanism in organic semiconductors is still under debate, for the majority of π-materials a limited delocalization of the electronic wavefunction is expected because the intermolecular forces are relatively weak van der Waals interactions, with the wavefunction localized to a finite number of molecules (or even a single molecule) instead of extending over the entire volume of the organic solid (*i.e.*, a band model in the case of inorganic solids). An investigation of molecular clusters, however, allows for new insight into microscopic study charge (de)localization phenomena with the evolution of the physical properties from finite cluster to the bulk crystal to elucidate the delocalized or localized nature of the charge carrier as a function of system size.[1]

The goal of this work is to investigate the nature of charge-carrier (de)localization and the *inter*-molecular contribution to the overall reorganization energy. We note that the reorganization energy (λ) comprises both intra-molecular and inter-molecular components. The inter-molecular contribution to the reorganization energy results from the polarization of the surrounding medium, in other words, from the way the presence of a charge on a given molecule leads adjacent molecules to electronically polarize and geometry relax. Previously, a vast amount of work has been performed in order to characterize and understand the impact that the molecular packing has on the polarization energy and transport properties.[2-6,13,14] Recent work from our

group has focused on using a combined quantum-mechanics/molecular mechanics (QM/MM) approach at the DFT level to quantify the effect of polarization on the energies of hole (electron) charge carriers, with deviations of ~ 0.2 – 0.4 eV (~ 0.3 – 0.9 eV)[13] when compared to experiment. Accounting for the charge-quadrupole interactions,[7] with a higher-term multipole expansion that acts as a correction to the polarization energy for holes (electrons) improves the comparison to within ~ 0.6 eV (~ 0.0 – 0.4 eV) of experiment.[14] However, these previous calculations were carried out only under the assumption that the charge carriers are in all instances localized completely on a single molecule. In contrast, recent experimental data collected from ultra-violet photoelectron spectroscopy (UPS) with the goal of understanding the role of polarization and relaxation in anionic clusters of oligoacenes demonstrated evidence for a charged state that is potentially delocalized over several molecules,[10-12] which has not been accounted for in theoretical treatments to date. Similar experiments carried out for anthracene propose an anionic charge that is shared over two or three molecules and also detailed two isomers in the UPS spectra. [11,13,14]

We start with a discussion of the charge distribution for a model five-molecule cluster of the herringbone configuration seen for the oligoacene series (**Figure 5.1**). Once a rigorous understanding of the model system with CASSCF is obtained, a comparison can then be made to the performance of DFT in describing the (de)localization. With a proven method in hand, we can then determine information about the delocalization in the crystal structure electronic states and compare with the VDE measured from UPS.[10-12] To make a direct comparison with experiment, we then employ a self-consistent quantum-mechanical/embedded-charge (QM/EC)

approach to investigate the interplay between the charge localization/delocalization and the electronic/molecular reorganization resulting from polarization.

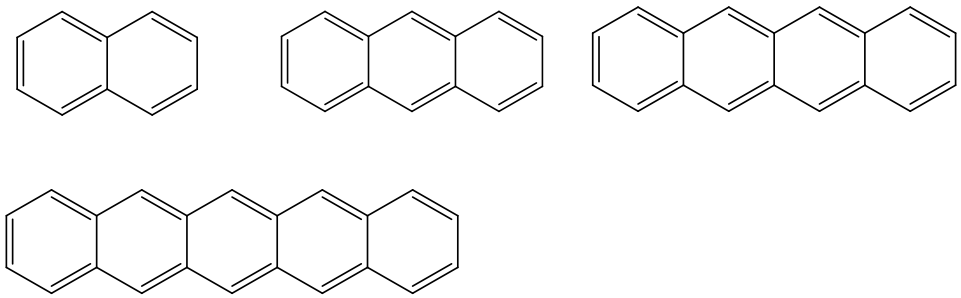

Figure 5.1. Molecular structure of linear oligoacenes naphthalene, anthracene, tetracene, and pentacene.

5.2. Methodology

The QM/EC calculations were performed with Gaussian 09 (Rev. D)[15] using the 6-31+G(d,p)[16] basis set and the DFT functional B3LYP[17-19] with the empirical dispersion term (-D) and ωB97X-D.[20] CASSCF/6-31G(d) [6-31+G(d)] calculations were performed in Gaussian 09 for the isolated five-molecule cluster and QM/EC calculations.

To compare accurately with experiment, a robust method capable of describing (de)localization that is free of the many-electron self-interaction error (MESIE) free is needed.[21,22] Exchange-correlation functionals, which are approximate, are the main contributors of the MESIE in DFT, and can result in spurious delocalization,[23] which has been shown for crystalline oligoacenes.[24] The authors of Ref. [24] found that the hole can localize or delocalize based on the amount of Hartree-Fock (HF) exchange used in a functional, and in fact showed that 70% HF exchange to

give a localized hole in a perfect molecular crystal, which most standard DFT functionals (*e.g.*, B3LYP has 20% HF exchange) would fail to describe properly. Therefore, we employ a system-dependent, non-empirically tuned functional that has been shown to dramatically reduce the MESIE present in the standard DFT methods. [25-27] For the long-range corrected functional ωB97X-D[28] employed here, the range-separation parameter ω partitions the Coulomb operator into short-range and long-range components as given in Eq. (2.10). The tuned-ω value was chosen such that the difference between the HOMO eigenvalue of the ground state and ionization potential (IP) (*i.e.*, the difference between the energy of the neutral and cation, $E_{sp}(\omega,N) - E_{sp}(\omega,N-1)$ is minimized, thus the method is referred to as IP-tuning[29-32] [Eq. (2.11)].

In previous work, we found that tuning the IP-tuning of ω is strongly dependent on the length-scales for electron conjugation of the system.[25] The IP-tuning procedure is anticipated to significantly reduce the MESIE in the highest occupied molecular orbital (HOMO), thereby removing spurious delocalization.[25-27] Here, the single-point ω-optimization calculations were performed with the 6-31G(d) basis set.

In order to evaluate the localization of these charge carriers, we employ a self-consistent quantum-mechanical/embedded-charge (QM/EC) approach where the charges in the QM region are derived from both non-empirically tuned DFT and complete-active space self-consistent field (CASSCF), which allows for a rigorous multi-determinate understanding of the charged-state in order to accurately model charge (de)localization and polarization arising from the presence of a charge. The QM/EC calculations were calculated where the DFT-computed atomic charges are frozen and an active QM region is then optimized in the presence of the charge field. We ignore

the multipole expansions to account for the charge–quadrupole correction under the assumption that this correction will be smaller in finite clusters and will depend on the size and the shape of the cluster. Geometries of molecules and lattice parameters were taken form crystallographic data. The atomic charges of the surrounding molecules in the frozen region were determined by iteratively optimizations of the individual molecular electron densities. Each iteration consisted of parallel single point embedded charge calculations for each molecule in the cluster charges set for the central anion derived by DFT calculations. Once the surrounding molecules are optimized, the resulting fitted charges were used for the subsequent iteration. This self-consistent procedure is continued until the change in total energy is less than 0.0001 Hartree.[8] For this study, CM5 was chosen for determine atomic charges.[33] An electron-density based charge assignments has been shown to accurately describe atomic charges more than an orbital-based description.[33]

In order to compare with experiment, we note that while there are several methods for measuring the polarization energy, we will limit our discussion to just a few of these experiments. The effect of the polarization energy of a charge carrier can be seen with the difference between the energy gap of single molecule and that for the crystal. The polarization energy is discussed in Chapter 1; however, we remind the reader that the polarization energy for a negative charge carrier (as that will be the focus of this chapter) is expressed by:

$$P^{-} = EA_B - EA_G, \qquad \textbf{(5.1)}$$

where EA_G and EA_B are electron affinities of the single molecule in the gas-phase and crystalline bulk, respectively. For an excess electron, the increase in polarization energy with increasing system size leads to a $EA_G < EA_B$.

The EA can be computed as a vertical or adiabatic process depending on the geometry of the final state. For example, the vertical (adiabatic) electron affinity defined as the energy difference between the neutral species at its optimized geometry and the anion species at the neutral (optimized) geometry:

$$vEA = E^{o}_{neutral} - E^{-}_{neutral}, \quad \textbf{(5.2)}$$

$$aEA = E^{o}_{neutral} - E^{-}_{anion}, \quad \textbf{(5.3)}$$

where $E^{o}_{neutral}$ is the optimized neutral geometry, $E^{-}_{neutral}$ is radical anion energy at the optimized neutral geometry, E^{-}_{anion} is the optimized radical anion energy.

Although, the EA can be measured through a variety of experiments such as inverse photoelectron spectroscopy (IPES) or UPS performed for anionic clusters, we will focus only on the latter. This experiment is carried out such that a system is first ionized with an excess electron that is then subsequently removed vertically (i.e., without geometry relaxation in the final state) with a photon of energy. The energy required to remove an electron from this bound state is due to both the electron affinity and the reorganization energy. Therefore, we define this process to consistent with what is understood in the literature as the vertical detachment energy (VDE) for an electron, given by:

$$VDE = E^{o}_{anion} - E^{-}_{anion}, \quad \textbf{(5.3)}$$

that is computed as the difference between the optimized radical anion energy (E^{-}_{anion}) and the closed-shell neutral configuration at the optimized anion geometry (E^{o}_{anion}). We note that this

definition for uses an optimized anion state under the assumption that the electron fills a state that allows for a geometry relaxation but is removed vertically and therefore has no associated geometry relaxation upon ionization.

Single-molecule naphthalene has been experimentally measured to have a negative aEA of -0.19 eV, indicating that an excess electron is not stable.[34] On the other hand, the anthracene, tetracene, and pentacene have a stable anion form, with an experimentally determined positive VDE of the single-molecule of +0.53 – 0.54 eV,[11,13,14,35] +1.04 – 1.06 eV,[12,36] and +1.35 eV,[36] respectively.

Before we begin a discussion of our results, we first will define the important experimental observations that we aim to reproduce. According to Ando *et al.*,[10] the UPS spectra of small naphthalene clusters exhibited two trends in regards to the VDE that was attributed to two structural isomers of same-sized cluster. One isomer was found to have a VDE of 2.12 eV when extrapolated to an infinite system size (*i.e.*, for the bulk); while, the second isomer was found to have two separate values of 0.86 and 1.1 eV when extrapolated; however, it should be noted that the magnitude of the VDE for these structurally distinct clusters did not change in the extrapolation as these energies were largely unaffected by the size of the cluster beyond a certain point. The structure for these distinct isomers is not known. Therefore, we investigate whether the differences in the measured VDE for these two isomers result from the nature of the charge carrier.

5.3. Results and Discussion

5.3.1. Multireference Calculation of Charge Distributions

To understand the potential delocalization of a hole or electron, we will first start with CASSCF-computed charge distribution that allows for an understanding of the potentially multi-reference nature of the wavefunction (**Figure 5.2**). However, the cost of CASSCF calculations limits the size of the clusters that could be treated; therefore, we start with a discussion of the calculations performed on a five-molecule herringbone-model system for naphthalene – pentacene and then compare to the IP-tuned ωB97X-D charges. This will allow for an understanding of the ability for MESIE-free long range corrected (LRC)-functionals to give an accurate charge delocalization. To understand the nature of charged states and to determine the degree of charge delocalization, CM5 atomic charges are reported for the five-molecule model system cutout from the crystal structure. A summary of the computed charges for naphthalene – pentacene anion are shown compared with DFT-computed charge distributions (Tables 5.1-5.2).

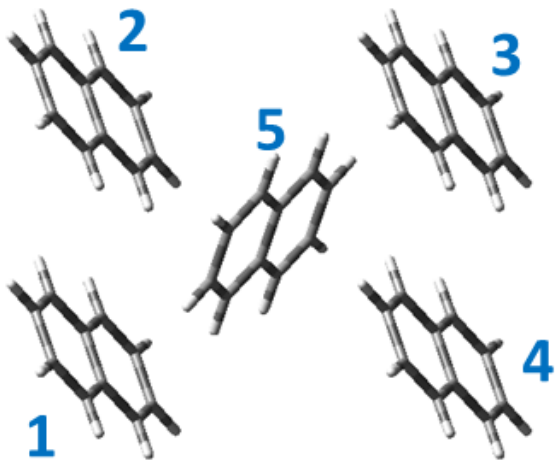

Figure 5.2. Model structure of naphthalene with each molecule labeled corresponding to Tables 5.1 and 5.2. The same configuration was used to model anthracene, tetracene, and pentacene.

The active-space for the anion is defined as eleven valence electrons in a total of ten HOMO/LUMO orbitals. The calculated CM5 atomic charges show there is a degree of delocalization over the five-molecule system for the anion; we compute that ~ 0.7e of the charge is localized for anthracene and pentacene, compared with a more delocalized electron of 0.4e for tetracene (Table 5.1). This result could be a consequence of the calculation being performed in the gas-phase, whereby a charge placed on molecule 1-4 is destabilized with respect to a charge on molecule 5 due to difference in environments.

Table 5.1. CASSCF(11,10)/6-31G(d) calculated CM5 charge distribution for the lowest energy anion state in the five-molecule herringbone configuration.

Molecule	Naphthalene	Anthracene	Tetracene	Pentacene
1	-0.068	-0.075	-0.09	-0.06
2	-0.072	-0.10	-0.20	-0.10
3	-0.068	-0.075	-0.09	-0.06
4	-0.072	-0.10	-0.20	-0.10
5	-0.72	-0.65	-0.42	-0.67
Total	-1.00	-1.00	-1.00	-1.00

5.3.2. DFT Calculation of Charge Distributions

With the CASSCF charges in hand, we can now compare how the IP-tuned ωB97X-D functional to determine accurately the charge delocalization. Qualitative agreement between the charge (de)localization is seen between the CASSCF and IP-tuned ωB97X-D functionals used here for naphthalene, anthracene, and pentacene (Table 5.2). However, CASSCF gives a different degree of localization for tetracene: ~0.4e (CASSCF) compared with ~0.7e (IP-tuned ωB97X-D). In general, IP-tuned ωB97X-D –computed charges indicate a delocalized charge for naphthalene - pentacene in the five-molecule herringbone structure with the molecules along the diagonal electronically polarized irrespective of the electronic coupling in the system.

Table 5.2. IP-tuned ωB97X-D/6-31G(d,p) calculated CM5 charges for lowest anion state in the five-molecule herringbone configuration.

	Naphthalene	Anthracene	Tetracene	Pentacene
1	-0.09	-0.075	-0.07	-0.06
2	-0.11	-0.10	-0.06	-0.10
3	-0.09	-0.075	-0.07	-0.06
4	-0.11	-0.10	-0.06	-0.10
5	-0.61	-0.65	-0.73	-0.67
Total	-1.00	-1.00	-1.00	-1.00

5.3.3. DFT Calculation of Vertical Detachment and Polarization Energies

We now compare the IP-tuned ωB97X-D results to the experiment quantitatively to further understand the fate of an excess electron in naphthalene, anthracene, tetracene, and pentacene clusters. The computed VDE using IP-tuned ωB97X-D/6-31+G(d,p) for single-molecule naphthalene (-0.20 eV), anthracene (+0.53 eV), tetracene (+1.07 eV), and pentacene (1.41 eV) are all in very good agreement with experiment: -0.19,[34] +0.53 – 0.54,[11,13,14,35] +1.04 – 1.06,[12,36] and +1.35,[36] respectively. In order to account for polarization effects of the environment (in this case, the surrounding naphthalene molecules in the crystal structure), the surrounding point charges are iteratively optimized around the single-molecule system to allow the surrounding system to electronically adjust to the excess charge. That is, the iterative charge optimization can simulate the instantaneous polarization effects to give a more accurate description of the bulk polarization energy.

For the optimized point-charge field of the neutral calculation, a 3-D cluster of n = 47 gives a vEA (-0.66 eV) similar to that of the isolate single molecule at the crystal geometry (-0.57 eV); the difference is due to the small increase in electronic polarization present even in the neutral crystal. However, the presence of these surrounding molecules do provide a suitable environment to stabilize the excess charge (*i.e.*, the vEA is still negative). Iteratively optimizing atomic charges in the presence of the monomeric anion results in stabilization of +0.45 eV (5 Å cluster), +0.77 eV (10 Å), and +0.59 eV (12 Å), resulting in an aEA of +0.09, -0.07, and +0.07, respectively (Table 5.3). The peculiar change in between 10 Å and 12 Å is a result of the difference in packing between these two clusters, where the central charge is completely encased for only the 12 Å cluster. Interestingly, when accounting for the anionic relaxation of 0.3 eV computed for the single molecule the VDE for the 12 Å cluster (+0.65 eV), is in good agreement (~0.15 eV smaller than) the experimentally determined VDE of ~ +0.8 eV for the same number of molecules. It is important to note that our results also match the dramatic appearance of a peak at a cluster size of n = 40 - 45 by Ando *et al.,*[10] which is understood through our results as only occurring at the point when the charged molecules is completely encased. This in turn leads to a large polarization energy of the surrounding molecules (P^- = -0.57 - 0.14 = -0.71 eV, computed for a cluster of n = 47) and accounts for ~ 65 % of the expected bulk value for naphthalene that was experimentally determined to be -1.10 eV for the naphthalene single crystal.[37]

The VDE is computed to remain the same going from a cluster with a radius of 12 Å (47 molecules) to 19.5 Å (71 molecules). However, experimentally determined VDEs measure a shift of 0.2 eV over this range; we note that although no change was computed over that range, a change of $P^- \approx 0.2$ eV was computed in going from a 10 Å (25 molecules) to 19.5 Å cluster,

which matches previously reported computational results for naphthalene for clusters with radii of 10-20 Å.[9] Therefore, we attribute the change in the experiment to an indication of that the polarization in these systems occurs in a step-wise fashion.

For an amorphous cluster of a similar number of molecules (n = 69), the VDE is computed to be 0.71 eV, which is 0.32 eV larger than what was computed for the crystalline cluster of the same size. This is consistent with an increased molecular rearrangement (*i.e.*, reorganization) that leads to larger polarization energy. This difference in the VDEs translates to the computed P^-: 1.06 eV for an amorphous cluster vs. 0.70 eV, *i.e.*, the amorphous cluster is 0.36 eV larger than what is computed for a crystalline cluster at approximately the same size. It is interesting to note that the difference in the polarization energy we capture from QM/EC calculations is ~0.3 eV, in close agreement with the experiment (~0.4 eV, estimated from the spectrum provided in Ref. 10).

To further understand the size of impact that the shape of these clusters can have in the computed VDE, we have also examined a 2-D disc-like cluster configuration (Table 5.3). Interestingly, the 2-D disc-like cluster gives a similar VDE (+0.19 eV) as was computed for the single molecule, indicating that the anion is not stabilized sufficiently by only the in-plane herringbone configuration. This conclusion is consistent with the third value computed for a 2-D disc-like configuration, however, with an (stack of 3 layers with an anionic naphthalene in the center of the central layer) extra layers that fully encase the anionic naphthalene molecule and now gives a positive VDE of +0.70 eV.

Table 5.3. Series of QM/EC calculations where the central single molecule represents the QM region and the radius of the 3-D cluster removed from the crystal structure.

Radius (Number of molecules)	Optimized point charge field		
	vEA (eV)	aEA (eV)	VDE (eV)
0 Å (1)	---	---	-0.20[a] (-0.57[b])
5 Å (13)	-0.52	+0.07	+0.24
10 Å (25)	-0.60	+0.04	+0.25
12 Å (47)	-0.58	+0.14	+0.39
19.5 Å (71)	-0.62	+0.13	+0.39
22.5 Å (116)	-0.61	+0.20	+0.49
Amorphous 15 Å (69)	-0.29	+0.46	+0.71
2-D 10 Å (13)	-0.68	-0.28	-0.19
2-D 22 Å (63)	-0.79	-0.33	-0.19
2-D/3-D 33 Å (195)	-0.38	+0.35	+0.70

a) Computed at the DFT-optimized anionic geometry
b) Computed at the crystalline geometry

With an understanding of naphthalene in hand, we now extend our study to anthracene, tetracene, and pentacene. We find a good agreement using the QM/EC method for anthracene and tetracene, and even smaller deviation than naphthalene, when compared with experimentally-derived VDEs (Table 5.4). We therefore can quantitatively reproduce the available experiments using the crystalline geometry and obtain a P^- that is 39 %, 62%, 43% of the bulk experimentally measured value.

Importantly, one additional consideration is the impact that charge delocalization has on the

computed VDE and polarization energy. Taking the 12 Å cluster and now computing the VDE for a five-molecule QM region to allow for a delocalization of the charge results in a value that changes by 0.03 eV due to the slight delocalization computed at the IP-tuned ωB97X-D level. Although a small change is computed in the VDE for a delocalized anion, there is a large stabilization in of 0.16 (0.39) eV in the aEA (vEA) indicating that the delocalization of the charge is a significantly stabilizing affect. This in turn leads to a 0.16 eV difference in the polarization energy for the electron P^{-} = -0.57 - 0.30 = -0.87 eV.

Table 5.4. Series of QM/EC calculations for similarly sized clusters (ranging from 19.5 to 21 Å) of naphthalene, anthracene, tetracene, and pentacene, where the single molecule is the QM region and the radius of the 3-D cluster removed from the crystal structure. The corrected value has the difference between VDE at the crystal structure geometry and optimized anion geometry included.

Molecule (Number of molecules)	IP-tuned ωB97X-D				Exp.	
	vEA	aEA	VDE (corrected)	P^-	VDE (n = ~70)	P^- *(bulk)*[d]
Naphthalene (71)	-0.62	+0.13	+0.39 (+0.76)	-0.71	+1.0 / 1.4[a]	-1.10
Anthracene (69)	+0.03	+0.78	+1.03 (+1.21)	-0.43	+1.3 / 1.5[b]	-1.09
Tetracene (71)	+0.60	+1.31	+1.53 (+1.77)	-0.57	+1.8 / 2.0[c]	-0.92
Pentacene (59)	+0.98	+1.62	+1.86 (+2.09)	-0.50	---	-1.17
Delocalized Naphthalene (47)	-0.19	+0.30	+0.42 (+0.79)	-0.87	+0.8 (n = 45)[a]	-1.10

a) Ref. 10
b) Ref. 11
c) Ref. 12
d) Ref. 37

5.4. Conclusions

We investigated the nature of an excess electron in the oligoacene crystal structures and allow for a comparison with experimental results. The experimental VDE can be reproduced quantitatively with IP-tuned ωB97X-D from the experimental UPS spectrum. Interestingly, we found that the peak attributed to crystalline-like structure in experiment is due to a 3-D cluster that only appears when a localized charge is encased completely, which occurs at ~ 42 molecules. Our results show that an excess electron is delocalized slightly over two/three molecules. Our results were compared with UPS measurements of finite oligoacene clusters to

detail the size-dependency of charge delocalization and polarization energy in finite clusters. The charge delocalization present in the herringbone crystal configuration was seen with CASSCF and these delocalized charges were then compared to a localized charge to quantify the effect of charge distribution has on the electronic reorganization energy, which we computed a difference of ~ 0.2 eV in the polarization energy for an electron. Therefore, we present a bottom-up study of the polarization energy for naphthalene and demonstrate that the electronic polarization energy is captured within the first three layers.

5.5. References

1. Coropceanu, V.; Cornil, J.; da Silva Filho, D. A.; Olivier, Y.; Silbey, R.; Bredas, J. L. Charge Transport in Organic Semiconductors. *Chemical Reviews* **2007**, *107*, 926-952.
2. Castet, F.; Aurel, P.; Fritsch, A.; Ducasse, L.; Liotard, D.; Linares, M.; Cornil, J.; Beljonne, D., Electronic polarization effects on charge carriers in anthracene: A valence bond study. *Physical Review B* **2008**, *77*, 115210.
3. Soos, Z. G.; Tsiper, E. V.; Pascal Jr, R. A., Charge redistribution and electronic polarization in organic molecular crystals. *Chemical Physics Letters* **2001**, *342*, 652-658.
4. Tsiper, E. V.; Soos, Z. G., Charge redistribution and polarization energy of organic molecular crystals. *Physical Review B* **2001**, *64*, 195124.
5. Topham, B. J.; Kumar, M.; Soos, Z. G., Ionization potentials of crystalline organic thin films: Position dependence due to molecular shape and charge redistribution. *Chemical Physics Letters* **2010**, *493*, 251-254.
6. Eisenstein, I.; Munn, R. W., Polarization energy of a localized charge in a molecular crystal. VI. Effect of excitons. *Chemical Physics* **1983**, *79*, 189-195.
7. Eisenstein, I.; Munn, R. W., Polarization energy of a localized charge in a molecular crystal. V. Effect of vacancies. *Chemical Physics* **1983**, *77*, 47-61.
8. Norton, J. E.; Bredas, J. L., Polarization Energies in Oligoacene Semiconductor Crystals. *Journal of the American Chemical Society* **2008**, *130*, 12377.
9. Ryno, S. M.; Lee, S. R.; Sears, J. S.; Risko, C.; Bredas, J. L., Electronic Polarization Effects upon Charge Injection in Oligoacene Molecular Crystals: Description via a Polarizable Force Field. *The Journal of Physical Chemistry C* **2013**, *117*, 13853-13860.
10. Ando, N.; Mitsui, M.; Nakajima, A., Photoelectron spectroscopy of cluster anions of naphthalene and related aromatic hydrocarbons. *The Journal of Chemical Physics* **2008**, *128*, 154318.
11. Ando, N.; Mitsui, M.; Nakajima, A., Comprehensive photoelectron spectroscopic study of anionic clusters of anthracene and its alkyl derivatives: Electronic structures bridging molecules to bulk. *The Journal of Chemical Physics* **2007**, *127*, 234305-13.
12. Mitsui, M.; Ando, N.; Nakajima, A., Mass Spectrometry and Photoelectron Spectroscopy of Tetracene Cluster Anions, (Tetracene) (n = 1−100): Evidence for the Highly Localized Nature of Polarization in a Cluster Analogue of Oligoacene Crystals. *The Journal of Physical Chemistry A* **2007**, *111*, 9644-9648.
13. Song, J. K.; Lee, N. K.; Kim, J. H.; Han, S. Y.; Kim, S. K., Anion clusters of anthracene, Ann−(n=1−16). *The Journal of Chemical Physics* **2003**, *119*, 3071-3077.
14. Song, J. K.; Lee, N. K.; Kim, S. K., Multiple Ion Cores in Anthracene Anion Clusters. *Angewandte Chemie International Edition* **2003**, *42*, 213-216.
15. M. J. Frisch, G. W. T., H. B. Schlegel, G. E. Scuseria, M. A. Robb, J. R. Cheeseman, G. Scalmani, V. Barone, B. Mennucci, G. A. Petersson, H. Nakatsuji, M. Caricato, X. Li, H. P. Hratchian, A. F. Izmaylov, J. Bloino, G. Zheng, J. L. Sonnenberg, M. Hada, M. Ehara, K. Toyota, R. Fukuda, J. Hasegawa, M. Ishida, T. Nakajima, Y. Honda, O. Kitao, H. Nakai, T. Vreven, J. A. Montgomery, Jr., J. E. Peralta, F. Ogliaro, M. Bearpark, J. J. Heyd, E. Brothers, K. N. Kudin, V. N. Staroverov, R. Kobayashi, J. Normand, K. Raghavachari, A. Rendell, J. C. Burant, S. S. Iyengar, J. Tomasi, M. Cossi, N. Rega, J. M. Millam, M. Klene, J. E. Knox, J. B. Cross, V. Bakken, C. Adamo, J. Jaramillo, R. Gomperts, R. E. Stratmann, O. Yazyev, A. J. Austin, R. Cammi, C. Pomelli, J. W. Ochterski, R. L. Martin, K. Morokuma, V. G.

Zakrzewski, G. A. Voth, P. Salvador, J. J. Dannenberg, S. Dapprich, A. D. Daniels, Ö. Farkas, J. B. Foresman, J. V. Ortiz, J. Cioslowski, and D. J. Fox *Gaussian 09, Revision A.1*, Gaussian, Inc.: Wallingford CT, 2009.
16. Hehre, W. J.; Ditchfield, R.; Pople, J. A., Self---Consistent Molecular Orbital Methods. XII. Further Extensions of Gaussian---Type Basis Sets for Use in Molecular Orbital Studies of Organic Molecules. *The Journal of Chemical Physics* **1972**, *56*, 2257-2261.
17. Becke, A. D., A new mixing of Hartree--Fock and local density-functional theories. *The Journal of Chemical Physics* **1993**, *98*, 1372-1377.
18. Lee, C.; Yang, W.; Parr, R. G., Development of the Colle-Salvetti correlation-energy formula into a functional of the electron density. *Physical Review B* **1988**, *37*, 785-789.
19. Stephens, P. J.; Devlin, F. J.; Chabalowski, C. F.; Frisch, M. J., Ab Initio Calculation of Vibrational Absorption and Circular Dichroism Spectra Using Density Functional Force Fields. *The Journal of Physical Chemistry* **1994**, *98*, 11623-11627.
20. Chai, J.-D.; Head-Gordon, M., Systematic optimization of long-range corrected hybrid density functionals. *The Journal of Chemical Physics* **2008**, *128*, 084106.
21. Ruzsinszky, A.; Perdew, J. P.; Csonka, G. I.; Vydrov, O. A.; Scuseria, G. E., Spurious fractional charge on dissociated atoms: Pervasive and resilient self-interaction error of common density functionals. *The Journal of Chemical Physics* **2006**, *125*, 194112-8.
22. Mori-Sánchez, P.; Cohen, A. J.; Yang, W., Many-electron self-interaction error in approximate density functionals. *The Journal of Chemical Physics* **2006**, *125*, 201102-4.
23. Cohen, A. J.; Mori-Sánchez, P.; Yang, W., Challenges for Density Functional Theory. *Chemical Reviews* **2011**, *112*, 289-320.
24. Sai, N.; Barbara, P. F.; Leung, K., Hole Localization in Molecular Crystals from Hybrid Density Functional Theory. *Physical Review Letters* **2011**, *106*, 226403.
25. Körzdörfer, T.; Sears, J. S.; Sutton, C.; Bredas, J. L., Long-range corrected hybrid functionals for pi-conjugated systems: Dependence of the range-separation parameter on conjugation length. *The Journal of Chemical Physics* **2011**, *135*, 204107-6.
26. Körzdörfer, T.; Parrish, R. M.; Sears, J. S.; Sherrill, C. D.; Bredas, J. L., On the relationship between bond-length alternation and many-electron self-interaction error. *The Journal of Chemical Physics* **2012**, *137*, 124305-8.
27. Körzdörfer, T.; Parrish, R. M.; Marom, N.; Sears, J. S.; Sherrill, C. D.; Bredas, J. L., Assessment of the performance of tuned range-separated hybrid density functionals in predicting accurate quasiparticle spectra. *Physical Review B* **2012**, *86*, 205110.
28. Chai, J.-D.; Head-Gordon, M., Long-range corrected hybrid density functionals with damped atom-atom dispersion corrections. *Physical Chemistry Chemical Physics* **2008**, *10*, 6615-6620.
29. Baer, R.; Livshits, E.; Salzner, U., Tuned Range-Separated Hybrids in Density Functional Theory. *Annual Review of Physical Chemistry* **2010**, *61*, 85-109.
30. Yanai, T.; Tew, D. P.; Handy, N. C., A new hybrid exchange–correlation functional using the Coulomb-attenuating method (CAM-B3LYP). *Chemical Physics Letters* **2004**, *393*, 51-57.
31. Baer, R.; Neuhauser, D., Density Functional Theory with Correct Long-Range Asymptotic Behavior. *Physical Review Letters* **2005**, *94*, 043002.
32. Vydrov, O. A.; Heyd, J.; Krukau, A. V.; Scuseria, G. E., Importance of short-range versus long-range Hartree-Fock exchange for the performance of hybrid density functionals. *The Journal of Chemical Physics* **2006**, *125*, 074106-9.

33. Marenich, A. V.; Jerome, S. V.; Cramer, C. J.; Truhlar, D. G., Charge Model 5: An Extension of Hirshfeld Population Analysis for the Accurate Description of Molecular Interactions in Gaseous and Condensed Phases. *Journal of Chemical Theory and Computation* **2012**, *8*, 527-541.
34. Jordan, K. D.; Burrow, P. D., Temporary anion states of polyatomic hydrocarbons. *Chemical Reviews* **1987**, *87*, 557-588.
35. Schiedt, J.; Weinkauf, R., Photodetachment photoelectron spectroscopy of mass selected anions: anthracene and the anthracene-H2O cluster. *Chemical Physics Letters* **1997**, *266*, 201-205.
36. Crocker, L.; Wang, T.; Kebarle, P., Electron affinities of some polycyclic aromatic hydrocarbons, obtained from electron-transfer equilibria. *Journal of the American Chemical Society* **1993**, *115*, 7818-7822.
37. Sato, N.; Inokuchi, H.; Silinsh, E. A., Reevaluation of Electronic Polarization Energies in Organic Molecular Crystals. *Chemical Physics* **1987**, *115*, 269−277.

Chapter 6 Understanding the Density Functional Dependence of DFT-Calculated Electronic Couplings in Organic Semiconductors

6.1. Introduction

The electronic coupling (transfer integral) is a key microscopic parameter that plays a critical role in the description of the charge transport properties in organic semiconductors; strong electronic interactions between π-conjugated molecules (*i.e.*, large inter-molecular wave-function overlaps) are necessary to lead to large transfer integrals and large charge-carrier mobilities.[1] Macroscopic properties such as the observed anisotropy of charge transport can also be explained via the directional dependence of the transfer integrals. The electronic couplings can be evaluated through quantum-mechanical calculations, for instance, at the density functional theory (DFT) level; direct comparisons can then be made between experimental data and the results of QM calculations of the charge-transport parameters.[2-8] However, it has been found that the computed transfer integrals are sensitive to the choice of the DFT functional.[9] Therefore, it is useful to try and understand the origin of the performance of different DFT functionals in calculating the electronic couplings for prototypical π-conjugated systems.

The impact of HF exchange on some of the important microscopic properties for charge transport, such as the reorganization energy, has been discussed previously.[10-12] Variations in the calculated transfer integral values were seen for several methods, including HF and DFT;[9] in fact, the authors of Ref. 9 noted that HF yields the largest electronic couplings for a model system, while smaller couplings were obtained when using global hybrid methods. Electronic

couplings calculated using HF have been shown to be some 20% larger than those from B3LYP.[13]

Here, we demonstrate that these variations in the transfer integral values are expected to vary in an almost linear fashion with the fraction of incorporated HF exchange in a global hybrid functional. To that end, we examine the sensitivity of the computed transfer integrals to the amount of fractional HF exchange for two prototypical π-conjugated molecular semiconductors, pentacene and rubrene (see Figure 6.1). Both exhibit large single-crystal hole mobilities[14-16] as a result of intrinsically large electronic couplings, which have been calculated previously with DFT methods.[2,17,18] We report the computed transfer integrals in these two systems when employing a broad range of standard hybrid and nonhybrid functionals. We then extend our understanding from the dimer calculations to those calculated in the solid state.

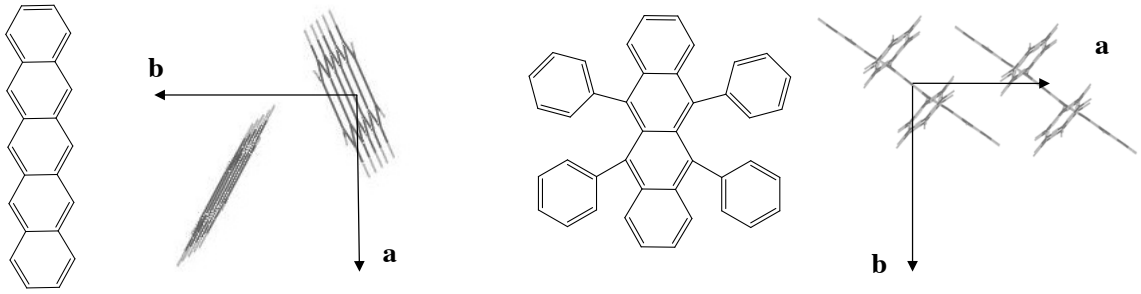

Figure 6.1. Chemical structures for the single molecule and dimer geometries taken from the *a*-*b* plane and along the *a* axis of the crystal unit cell for pentacene[19] (left) and rubrene[20] (right).

6.2. Methodology

The effective transfer integrals, $t_{AB} = \langle \varphi_A | H | \varphi_B \rangle$, ($\varphi_i$ is the monomer-localized HOMO [LUMO] orbital for hole [electron] transport) were evaluated by using a fragment orbital approach in combination with a basis set orthogonalization procedure.[21,22] All calculations were performed with the Gaussian 09 Rev. B.01 suite of programs.[23] The Pople 6-31G* basis set was employed in all cases;[24-27] previous studies have demonstrated the reliability of this basis for intermolecular transfer integral computations, which provides accuracy with low computational cost.[28] While larger basis sets may impact the absolute magnitudes of the computed couplings and proper exponential decay of t_{AB},[22,29] this is not anticipated to affect the analysis presented in this work.

The geometries of the dimers were obtained from published crystal structures for rubrene[20] and pentacene.[19] For rubrene, the electronic couplings were calculated for the π-stacked pair in the a crystallographic direction of the unit cell (see Figure 6.1); for pentacene, the coupling was calculated for the pair of molecules in the diagonal direction of the herringbone-type structure, which was previously calculated to be the direction of strongest coupling.[2] The transfer integrals for both holes (t_{AB}^{H}) and electrons (t_{AB}^{L}) were considered. In all cases, the absolute magnitude of the electronic coupling is shown.

In order to test the dependence of the calculated electronic coupling with HF exchange, different pure (semi)local and hybrid exchange-correlation functionals were considered: as LDA, the SVWN functional;[30-33] as pure GGA functionals, the 1996 functional of Perdew, Burke and

Ernzerhof (PBE[34,35]) as well as the Becke exchange functional[36] in combination with the correlation functional of Lee, Yang, and Parr[37] (BLYP) and with the 1986 correlation functional from Perdew[38] (BP86); as pure meta-GGA, the Truhlar M06-L[39] functional. Hybrid GGA functionals were selected to be analogous to the pure GGA functional indicated above: Adamo and Baron's hybrid variant of the PBE functional (PBE0[40]) as well as combinations of the three-parameter hybrid exchange functional from Becke with the LYP (B3LYP[38,41,42]) and P86[39] (B3P86) correlation functionals. To include a hybrid-GGA with larger amounts of HF exchange, we also tested the BHandHLYP combination that includes 50% Becke exchange and 50% HF exchange combined with the LYP correlation functional. Hybrid meta-GGAs include the family of functionals from Truhlar: M06,[43] M06-2X,[43] and M06-HF,[44,45] which include 27%, 54%, and 100% exact HF exchange, respectively, as well as the approximation from Boese and Martin (BMK[46]), which includes 42% HF exchange.

In order to remove the possible dependence on the choice of the exchange-correlation functional, we also considered a general hybrid GGA functional (referred to as B_αLYP) from Eq. (4.2), with variable amounts of HF exchange (E_X^{HF}) and where the DFT nonlocal exchange and correlation corrections are defined to retrieve the B3LYP functional when α is 0.20. The transfer integral values evaluated from HF were also included for comparison. In addition, the LRC functional ωB97[47] was considered to highlight the impact of ω for this important class of functionals as well as to conveniently tune the length scale of the transition from DFT exchange to HF exchange.

In order to understand the dependence of the transfer integral on the fraction of HF exchange, it is useful to consider the decay of the generalized Kohn-Sham matrix elements with intermolecular separation between orbitals on the two monomers for each of the terms in Eq. (2.26) (*i.e.*, $\langle\varphi_A|H|\varphi_B\rangle$). The two-center kinetic energy integrals and the two- and three-center nuclear attraction integrals arising in the off-diagonal contributions can be expanded as sums of two-center overlap integrals; these terms can thus be expected to decay exponentially with the separation between molecular sites. The off-diagonal contribution of the electron-electron interaction decays as 1/r. The remaining contributions to t_{AB} will be determined by the specific form of the exchange-correlation potential and the coupling (α) of the noninteracting and interacting systems. However, it can be expected that the choice of semilocal functional will provide only a small contribution to the transfer integral for large intermolecular distances (*vide infra*) because of the short-range nature of the Kohn-Sham exchange-correlation potential that is exponentially decaying.[48] Consequently, larger electronic couplings are calculated when the amount of nonlocal HF exchange (decaying as 1/r) is increased (α) and therefore, the amount of semilocal exchange is decreased proportionally. This will be demonstrated in the results below showing that the transfer integral is largely independent of the specific choice of the underlying semilocal functional and is linearly proportional to α.

6.3. Results and Discussion

6.3.1. Evolution of *t* with %HF Exchange in Standard DFT Functionals

The results for the functionals described above are illustrated in Figure 6.2. For (semi)local exchange-correlation without HF exchange, the t_{AB}^{H} values for holes in rubrene are obtained with SVWN, PBE, BP86, BLYP, and M06-L to be 87, 84, 85, 85, and 85 meV, respectively. The

inclusion of HF exchange results in a linear increase in magnitude of the electronic coupling; t_{AB}^{H} increases by over 60% when the HF exchange is increased from 0% to 100%. Nearly identical linear trends are observed for t_{AB}^{L} that increases by ~100% in going from the pure functionals (~43 meV) to the HF and M06-HF (~85 meV) values. For pentacene, a similar behavior is observed: both t_{AB}^{H} and t_{AB}^{L} increase by about 60% with full incorporation of nonlocal HF exchange. The linear dependence of t_{AB} as a function of HF exchange is better demonstrated in Figure 6.3 where we plot the $B_{\alpha}LYP$ results with varying amounts of HF exchange; a perfectly linear evolution is then seen. This demonstrates that the minor deviations from the linear dependence observed on Figure 6.2 are due to the differences in the semilocal exchange-correlation term.

To further test the influence of HF exchange on the transfer integral, we considered the rubrene dimer with the ωB97 long-range corrected functional and varied the range-separation parameter ω (we note that the characteristic length 1⁄ω approximately corresponds to the distance at which the exchange transitions from mostly the short-range treatment, *i.e.*, in this case DFT, to mostly the long-range treatment, *i.e.*, HF). In Figure 6.4, the magnitudes of t_{AB}^{H} and t_{AB}^{L} are observed to decrease with increasing characteristic length (decreasing ω), which is indicative of the impact of

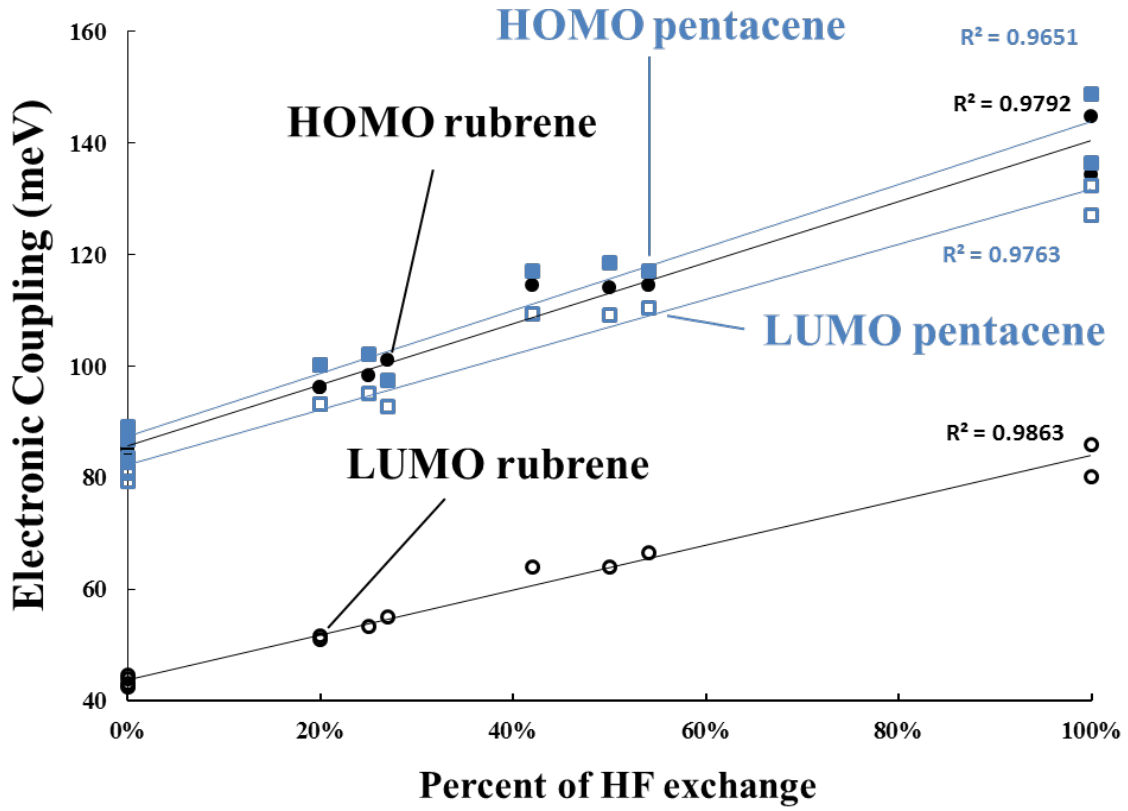

Figure 6.2. Effective electronic coupling for HOMO-HOMO (t_{AB}^{H}) (filled symbols) and LUMO-LUMO (t_{AB}^{L}) (empty symbols) of rubrene (black circles) and pentacene (blue squares) with the following functionals from left to right (with percentage of HF exchange): SVWN (0%), PBE (0%), BP86 (0%), M06-L (0%), B3P86 (20%), B3LYP (20%), PBE0 (25%), M06 (27%), BMK (42%), BHandHLYP (50%), M06-2X (54%), M06-HF (100%) and HF.

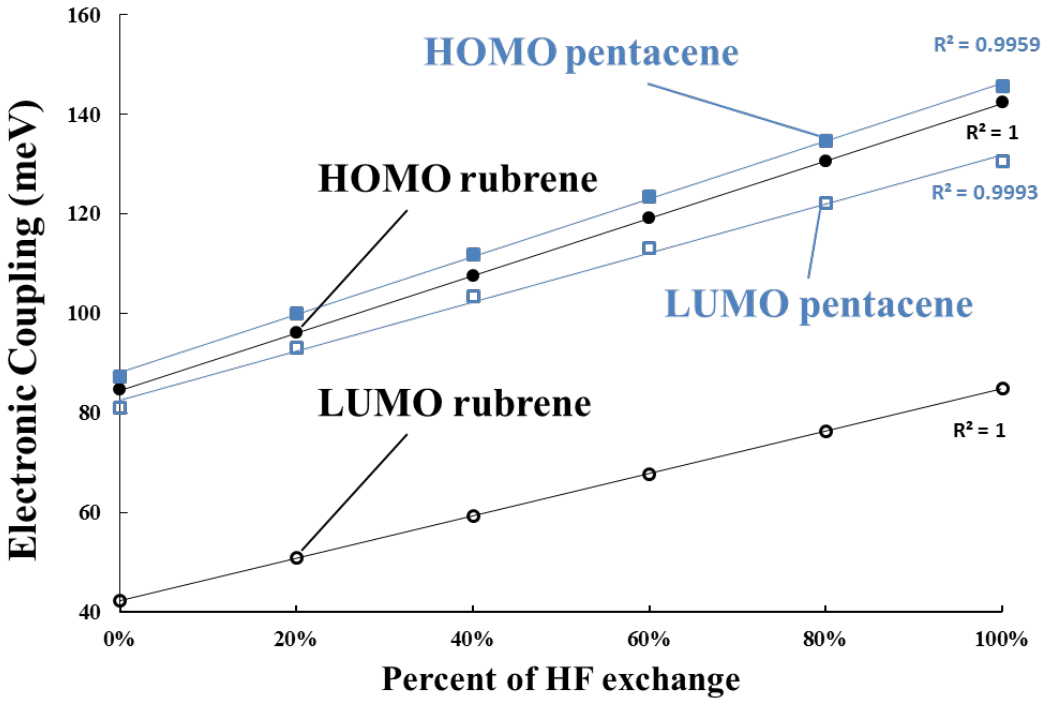

Figure 6.3. Evolution of the t_{AB}^{H} (filled symbols) and t_{AB}^{L} (open symbols) values generated from Eq. **(4.2)** for rubrene (black) and pentacene (blue) with $B_{\alpha}LYP$ as a function of varying amount of HF exchange.

6.3.2. Evolution of *t* with %HF Exchange in Long-range Corrected DFT Functionals

HF exchange on the magnitude of the transfer integral. At small 1⁄ω values, when the HF exchange is being incorporated at a shorter distance relative to the intermolecular separation, the HF exchange term increases the magnitude of the transfer integral; for 1⁄ω = 1.06 Å (ω = 0.500 $bohr^{-1}$), t_{AB}^{H} and t_{AB}^{L} amount to 133 and 79 meV, respectively, *i.e.*, values very close (ca. 93%) to those calculated with $B_{\alpha}LYP$ using 100% HF exchange. However, at larger 1⁄ω values, t_{AB}^{H} and t_{AB}^{L} decrease to values that eventually become very close to the t_{AB}^{H} and t_{AB}^{L} values calculated with $B_{\alpha}LYP$ using 0% HF exchange; this is due to HF exchange being essentially incorporated beyond the intermolecular separation, thereby having the dimer effectively treated with only semilocal exchange. It is worth pointing out that the ω value can be optimized non-empirically,

namely by using Janak's theorem,[49] where the difference between the HOMO eigenvalue of the ground state and the vertical ionization potential is minimized.[50] This procedure was performed on a single rubrene molecule, using the crystal structure geometry, and resulted in an ω value of 0.221 bohr^{-1} (1⁄ω = 2.40 Å) as compared to the default ω value of 0.400 bohr^{-1} for this functional. The calculations based on the IP-optimized-ωB97 functional then yield t_{AB}^{H} and t_{AB}^{L} values of 111 and 63 meV, respectively. The IP-tuning procedure is system dependent and, therefore, will change the effective amount of HF exchange, leading to a different magnitude for t_{AB}. To demonstrate this point, the range-separated functionals CAM-B3LYP,[51] HSE,[52,53] and LC-ωPBE[54-56] were used to calculate t_{AB} for rubrene using the default range-separation parameters. The computed t_{AB}^{H} (t_{AB}^{L}) values were calculated to be 111 (62) meV for CAM-B3LYP, 96 (51) meV for HSE, and 118 (68) meV for LC-ωPBE. Employing the IP-tuning procedure to optimized the ω for LC-BLYP (ω = 0.163 bohr^{-1}) and LC-ωPBE (ω = 0.161 bohr^{-1}), the electronic couplings of 105 (58) and 97 (54) are obtained, respectively. The deviation of ca. 10% between the two IP-tuned functionals is greater than the difference seen for different semilocal approximations with identical amounts of HF exchange; however, this is anticipated to be a consequence of different methods for incorporating the amount of HF exchange.

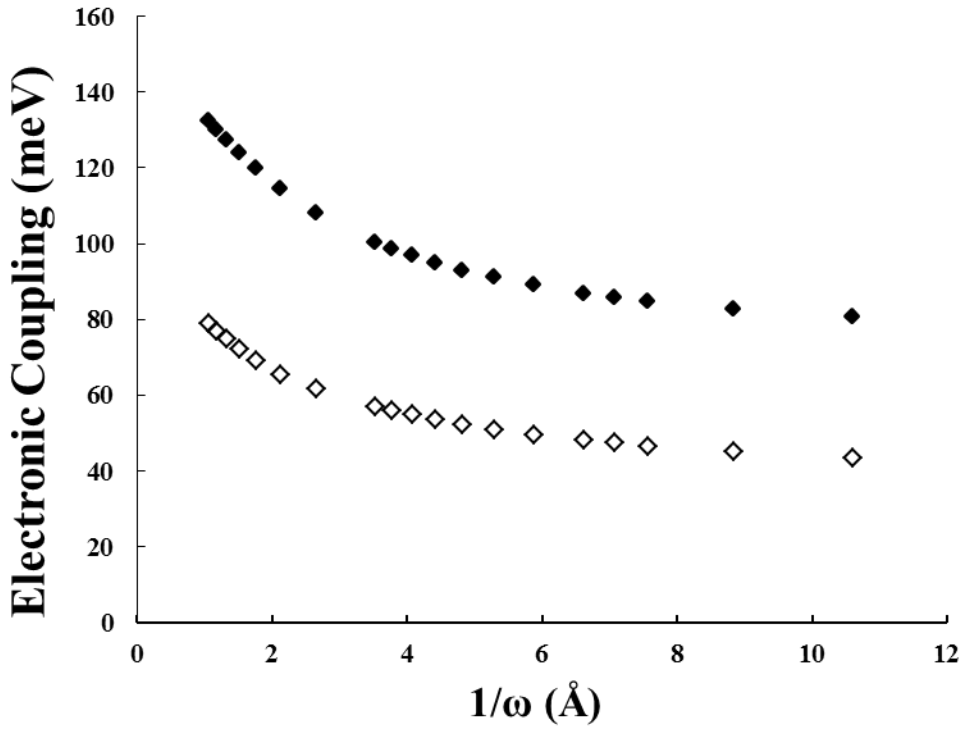

Figure 6.4. Evolution of the t_{AB}^{H} (filled symbols) and t_{AB}^{L} (empty symbols) values for rubrene calculated with ωB97, as a function of 1/ω for ω between 0.500 – 0.050 bohr^{-1}. The distance between the molecular planes of the two molecules is 3.70 Å, *i.e.*, 6.98 bohr.

6.3.3. Evolution of Bandwidth, Band Gap, and Effective Masses with %HF Exchange

In order to understand the impact that the percent of the HF exchange in a given functional (Note that in this sections, the semilocal exchange-correlation functional PBE was used as opposed to BLYP, which we will refer to as αPBE) has on the band structure and effective masses, we have investigated the bandstructure computed for pentacene going from 0 to 50% HF exchange. The valence [conduction] bandwidth were computed to increase by 0.21 [0.28] eV, *i.e.* by about 40% Figure 6.5. This result is consistent with the increase in *t* discussed above. The effective masses for holes [electrons] were calculated at the (0.375, 0.5, 0.075) [(0.39, 0.5, 0.5)] point in reciprocal space; the smallest effective mass directions both for holes and electrons are

approximately along the herringbone direction. The effective masses for holes [electrons] decrease almost linearly (R^2 = 0.977 [0.97]) from 2.01 to 1.41 [1.95 to 1.36] m_0 with an increase in %HF exchange. The computed effective masses at 25% HF exchange (*i.e.*, the PBE0 functional) are in good agreement with previous reported values for pentacene.[57] The band gap also shows a linear increase (R^2 = 0.999) with a factor of 3 from 0.83 to 3.08 eV (Figure 6.5). These results show that the DFT-computed band gaps, bandwidths and effective masses are quite arbitrary and span in a large range depending on the % HF exchange used in a given functional.

Because such a large spread of values is seen for these two important charge-transport parameters, the need arises to tune the amount of %HF exchange to experimentally determined bandwidths and bandgaps. However, in this case, we tune the of %HF exchange to match the results obtained with the *GW* approximation,[58,59] which have been shown to accurately reproduce experimental fundamental gaps and valence [conduction] bandwidths for both inorganic and organic semiconductors.[58,60] In particular interest to this study, a fundamental gap of 1.9 eV and valence [conduction] bandwidth of 0.54 [0.67] eV were reported for pentacene using G_0W_0.[61] Therefore we examine the optimal value of the %HF exchange in αPBE compared to G_0W_0 for crystalline pentacene. Tuning the %HF exchange to the G_0W_0 fundamental gap (at *E* point in the Brillouin zone) gives an optimal value of 32% HF in αPBE. Using this tuned functional to then compute the bandstructure results in an excellent agreement for the bandwidths at several *k*-points (**Table 6.1**).

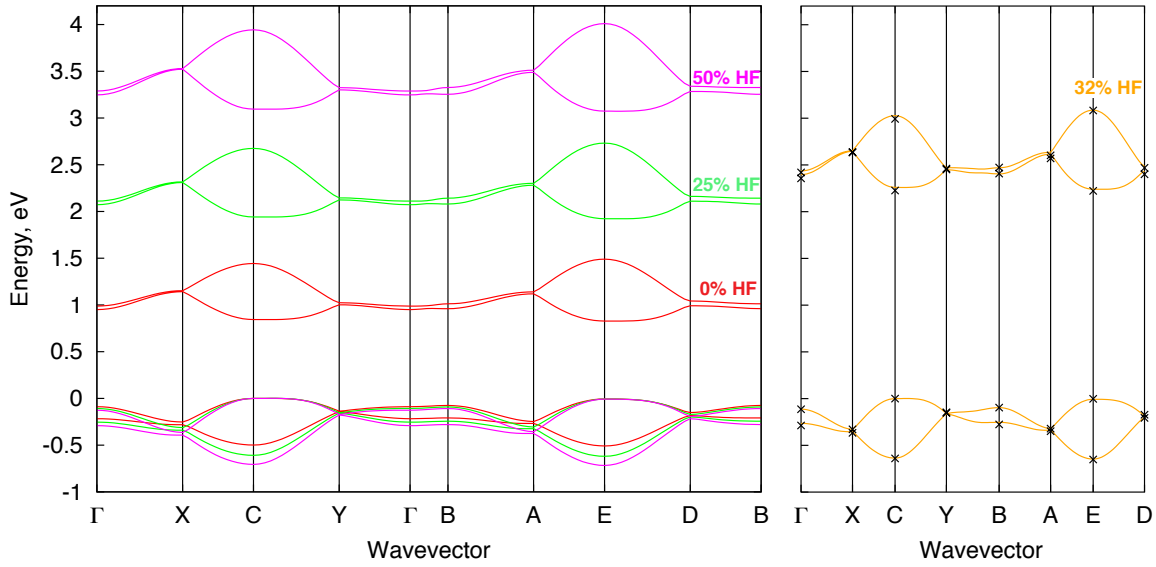

Figure 6.5. Valence and conduction bands of pentacene obtained using αPBE functional with different %HF (left). Comparison of αPBE and G_0W_0 (crosses) is shown on the right panel. The points of high symmetry in the first Brillouin zone are labeled as follows: Γ = (0,0,0), X = (0.5,0,0), Y = (0,0.5,0), B = (0,0,0.5), C = (0.5,0.5,0), A = (0.5,0,0.5), E = (0.5,0.5,0.5) and D = (0, 0.5, 0.5), all in crystallographic coordinates. The zero of energy is given at the top of the valence band, at C point.

Table 6.1. The fundamental gap (E_g) at the *E* high-symmetry point, the smallest hole and electron effective mass (m^H_{eff} and m^e_{eff} in mass of the electron at rest, m_0), valence (VBW) and conduction (CBW) bandwidths at *E* point. All energies units in eV.

%HF	E_g	m^H_{eff}	m^e_{eff}	VBW	CBW
0	0.83	2.01	1.95	0.50	0.66
25	1.93	1.64	1.58	0.61	0.81
32	2.25	1.56	1.51	0.64	0.85
50	3.08	1.41	1.36	0.71	0.94
G_0W_0	2.22	-	-	0.65	0.86

6.3.4. Comparison of *t* with Exchange-Repulsion

In addition to understanding the impact of the choice of functional in describing the electronic coupling in molecular and periodic systems, we now explore the connection between the electronic and non-covalent interactions that arise due to the overlap of π-orbitals on neighboring molecules, which lead to the intermolecular electronic couplings (or band dispersions) that are key parameters of charge-carrier transport. The important result that arises from these calculations is that there is a correspondence between the degrees of intermolecular electronic coupling and exchange-repulsion. In terms of non-covalent interactions, the exchange-repulsion is a destabilizing force that arises as a consequence of the Pauli exclusion principle (*i.e.,* no two electrons [fermions] can occupy the same quantum state).[62,63] As the molecules are brought closer together, the electrons in the molecular orbitals (*e.g.,* the highest-occupied molecular orbitals [HOMOs]) on the separate pentacene molecules begin to occupy the same space, and a repulsive interaction arises that physically limits the proximity of the two molecules so that the electrons coming from the respective molecules avoid possessing the same quantum state. This effect is prominent in stacked materials with large intermolecular electronic couplings, as there is necessarily a large molecular orbital overlap that results in a large repulsion due to electron exchange.

This connection is demonstrated for a model pentacene dimer at an intermolecular separation of 3.50 Å; starting from a perfectly co-facial configuration (recall that perfect co-facial stacking interactions lead to large orbital overlap and large electronic couplings) one monomer is then

displaced by increments of 0.50 Å along the long axis to determine the structure-property relationships (Figure 6.6). For the pentacene dimer, the exchange-repulsion (defined below, red line in Figure 6.6, determined using symmetry-adapted perturbation theory [SAPT0][64] with the jun-cc-pVDZ basis set) is maximum (35 kcal mol^{-1}) for the perfectly co-facial configuration and decreases to 27 kcal mol^{-1} for the long-axis monomer displacement of 1.5 Å. This trend is matched by the (absolute value) intermolecular electronic coupling between the respective HOMOs on the two pentacene molecules, which is maximal in the perfectly co-facial configuration with a value of 8 kcal mol^{-1} and decreases to 0 kcal mol^{-1} at a displacement of 1.5 Å. Both physical properties show an oscillatory pattern that corresponds with the nodal pattern of the pentacene HOMO. The electronic coupling can go to 0 kcal mol^{-1} with displacement even though there remains considerable spatial overlap of the pentacene backbones. The exchange-repulsion energy in these systems, on the other hand, is determined from the overlap among all occupied orbitals and is dominated by the electrons in the σ framework; therefore, the exchange-repulsion term remains large in magnitude, neither going to zero nor changing sign for the intermolecular separations considered here.

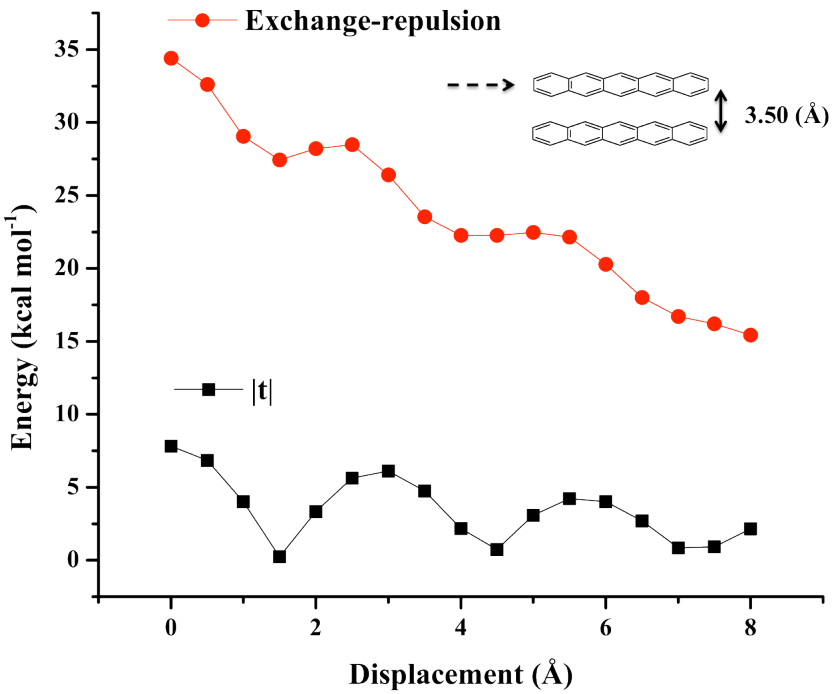

Figure 6.6. Exchange-repulsion energy (red line) as determined at the SAPT0/jun-cc-pVDZ level of theory and intermolecular electronic coupling (*t*, black line) as determined from the absolute value of the HOMO-HOMO overlap at the B3LYP/cc-pVDZ level of theory for two pentacene molecules at an intermolecular separation of 3.50 Å.

6.4. Conclusions

We have demonstrated that the amount of HF exchange substantially affects the intermolecular transfer integral in a linear fashion with respect to the fraction of nonlocal HF exchange incorporated in a standard hybrid functional. In fact, among different DFT functionals, the transfer integrals can vary by nearly a factor of two in the case of pentacene and rubrene. Importantly, these variations need to be taken into account when comparing electronic couplings obtained with different functionals. While the choice of the exchange-correlation functional also affects the computed transfer integrals, this influence is small and much less significant than the impact of the fraction of HF exchange included in the functionals considered here. A clear

relationship can thus be established between the magnitude of the electronic couplings and the amount of HF exchange incorporated into the DFT methods we considered.

Although previous studies have shown the magnitude of the transfer integrals to be affected by the amount of HF exchange, the direct and linear dependence highlighted here is a point that has been largely overlooked. We believe that the present analysis will be useful to better assess the impact of the DFT functionals in the determination of electronic couplings in organic semiconductors, a key parameter for charge transport.

6.5. References

1. Coropceanu, V.; Cornil, J.; da Silva Filho, D. A.; Olivier, Y.; Silbey, R.; Bredas, J. L. Charge Transport in Organic Semiconductors. *Chemical Reviews* **2007**, *107*, 926-952.
2. Cornil, J.; Calbert, J. P.; Bredas, J. L. Electronic Structure of the Pentacene Single Crystal: Relation to Transport Properties. *Journal of the American Chemical Society* **2001**, *123*, 1250-1251.
3. Cornil, J.; Beljonne, D.; Calbert, J. P.; Bredas, J. L. Interchain Interactions in Organic π-Conjugated Materials: Impact on Electronic Structure, Optical Response, and Charge Transport. *Advanced Materials* **2001**, *13*, 1053-1067.
4. Bredas, J. L.; Calbert, J. P.; da Silva Filho, D. A.; Cornil, J. Organic Semiconductors: A Theoretical Characterization of the Basic Parameters Governing Charge Transport. *Proccedings of the National Academy of Sciiences* **2002**, *99*, 5804-5809.
5. Deng, W.-Q.; Goddard, W. A. Predictions of Hole Mobilities in Oligoacene Organic Semiconductors from Quantum Mechanical Calculations. *Journal of Physical Chemistry B* **2004**, *108*, 8614-8621.
6. Wen, S.-H.; Li, A.; Song, J.; Deng, W.-Q.; Han, K.-L.; Goddard, W. A. First-Principles Investigation of Anistropic Hole Mobilities in Organic Semiconductors. *Journal of Physical Chemistry B* **2009**, *113*, 8813-8819.
7. Wen, S.-H.; Deng, W.-Q.; Han, K.-L. Revealing Quantitative Structure-Activity Relationships of Transport Properties in Acene and Acene Derivative Organic Materials. *Physcial Chemistry Chemical Physics* **2010**, *12*, 9267-9275.
8. Stehr, V.; Pfister, J.; Fink, R. F.; Engels, B.; Deibel, C. First-Principles Calculations of Anisotropic Charge-Carrier Mobilities in Organic Semiconductor Crystals. *Physical Review B* **2011**, *83*, 155208-155222.
9. Huang, J.; Kertesz, M. Validation of Intermolecular Transfer Integral and Bandwidth Calculations for Organic Molecular Materials. *The Journal of Chemical Physics* **2005**, *122*, 234708-234717.
10. Dierksen, M.;Grimme, S. The Vibronic Structure of Electronic Absorption Spectra of Large Molecules: A Time-Dependent Density Functional Study on the Influence of "Exact" Hartree−Fock Exchange. *Journal of Physical Chemistry A* **2004**, *108*, 10225-10237.
11. Sánchez-Carrera, R. S.; Coropceanu, V.; da Silva Filho, D. A.; Friedlein, R.; Osikowicz, W.; Murdey, R.; Suess, C.; Salaneck, W. R.; Bredas, J. L. Vibronic Coupling in the Ground and Excited States of Oligoacene Cations. *Journal of Physical Chemistry B* **2006**, *110*, 18904-18911.
12. Sancho-García, J. C. Assessment of Density-Functional Models for Organic Molecular Semiconductors: The Role of Hartree–Fock Exchange in Charge-Transfer Processes. *Chemical Physics* **2007**, *331*, 321-331.
13. Troisi, A.; Orlandi, G. The Hole Transfer in DNA: Calculation of Electron Coupling Between Close Bases. *Chemical Physics Letters* **2001**, *344*, 509-518.
14. Jurchescu, O. D.; Baas, J.; Palstra, T. T. M. Effect of Impurities on the Mobility of Single Crystal Pentacene. *Applied Physical Letters* **2004**, *84*, 3061-3063.
15. Yamagishi, M.; Takeya, J.; Tominari, Y.; Nakazawa, Y.; Kuroda, T.; Ikehata, S.; Uno, M.; Nishikawa, T.; Kawase, T. High-Mobility Double-Gate Organic Single-Crystal Transistors with Organic Crystal Gate Insulators. *Applied Physical Letters* **2007**, *90*, 182117-182120.

16. Zhang, K. K.; Tan, K.; Zou, C.; Wikberg, M.; McNeil, L. E.; Mhaisalkar, S. G.; Kloc, C. Control of Charge Mobility in Single-Crystal Rubrene Through Surface Chemistry. *Organic Electronics* **2010**, *11*, 1928-1934.
17. de Wijs, G. A.; Mattheus, C. C.; de Groot, R. A.; Palstra, T. T. M. Anisotropy of the Mobility of Pentacene from Frustration. *Synthetic Metals* **2003**, *139*, 109-114.
18. da Silva Filho, D. A.; Kim, E. G.; Bredas, J. L. Transport Properties in the Rubrene Crystal: Electronic Coupling and Vibrational Reorganization Energy. *Advanced Materials* **2005**, *17*, 1072-1076.
19. T.Siegrist; C.Besnard; S.Haas; M.Schiltz; P.Pattison; D.Chernyshov; B.Batlogg; C.Kloc, A Polymorph Lost and Found: The High-Temperature Crystal Structure of Pentacene. *Advanced Materials* **2007**, *19*, 2079-2082.
20. Bulgarovskaya, I.; Vozzhennikov, V.; Aleksandrov, S.;Belsky, V. *PSR Zinat. Akad. Vestis, Khim. Ser* **1983**, *53*.
21. Senthilkumar, K.; Grozema, F. C.; Bickelhaupt, F. M.; Siebbeles, L. D. A. Charge Transport in Columnar Stacked Triphenylenes: Effects of Conformational Fluctuations on Charge Transfer Integrals and Site Energies. *The Journal of Chemical Physics* **2003**, *119*, 9809-9817.
22. Valeev, E. F.; Coropceanu, V.; da Silva Filho, D. A.; Salman, S.; Brédas, J. L. Effect of Electronic Polarization on Charge-Transport Parameters in Molecular Organic Semiconductors. *Journal of the American Chemical Society* **2006**, *128*, 9882-9886.
23. M. J. Frisch, G. W. T., H. B. Schlegel, G. E. Scuseria, M. A. Robb, J. R. Cheeseman, G. Scalmani, V. Barone, B. Mennucci, G. A. Petersson, H. Nakatsuji, *et al. Gaussian 09, Revision A.1*, Gaussian, Inc.: Wallingford CT, **2009**.
24. Hehre, W. J.; Ditchfield, R.; Pople, J. A. Self---Consistent Molecular Orbital Methods. XII. Further Extensions of Gaussian---Type Basis Sets for Use in Molecular Orbital Studies of Organic Molecules. *The Journal of Chemical Physics* **1972**, *56*, 2257-2261.
25. Hariharan, P. C.; Pople, J. A. The Influence of Polarization Functions on Molecular Orbital Hydrogenation Energies. *Theoretical Chemistry Accounts* **1973**, *28*, 213-222.
26. Francl, M. M.; Pietro, W. J.; Hehre, W. J.; Binkley, J. S.; Gordon, M. S.; DeFrees, D. J.; Pople, J. A. Self-Consistent Molecular Orbital Methods. XXIII. A Polarization-Type Basis Set for Second-Row Elements. *The Journal of Chemical Physics* **1982**, *77*, 3654-3665.
27. Rassolov, V. A.; Pople, J. A.; Ratner, M. A.; Windus, T. L. 6-31G* Basis Set for Atoms K Through Zn. *The Journal of Chemical Physics* **1998**, *109*, 1223-1229.
28. Huang, J.; Kertesz, M. Intermolecular Transfer Integrals for Organic Molecular Materials: Can Basis Set Convergence be Achieved? *Chemical Physics Letters* **2004**, *390*, 110-115.
29. Reslan, R.; Lopata, K.; Arntsen, C.; Govind, N.; Neuhauser, D. Electron Transfer Beyond the Static Picture: A TDDFT/TD-ZINDO Study of a Pentacene Dimer. *The Journal of Chemical Physics* **2012**, *137*, 22A502-22A506.
30. Hohenberg, P.; Kohn, W. Inhomogeneous Electron Gas. *Physical Review* **1964**, *136*, B864-B871.
31. Kohn, W.; Sham, L. J., Self-Consistent Equations Including Exchange and Correlation Effects. *Physical Review* **1965,** *140*, A1133-A1138.
32. Slater, J. C., In *The Self-Consistent Field for Molecular and Solids, Quantum Theory of Molecular and Solids*, McGraw-Hill: New York, 1974; Vol. 4.
33. Vosko, S. H.; Wilk, L.; Nusair, M. Accurate Spin-Dependent Electron Liquid Correlation Energies for Local spin Density Calculations: a Critical Analysis. *Candian Journal of Physics* **1980**, *58*, 1200-1211.

34. Perdew, J. P.; Burke, K.; Ernzerhof, M. Generalized Gradient Approximation Made Simple. *Physical Review Letters* **1996**, *77*, 3865-3868.
35. Perdew, J. P.; Burke, K.; Ernzerhof, M., Errata: Generalized Gradient Approximation Made Simple. *Physical Review Letters* **1997**, *78*, 1396.
36. Becke, A. D. Density-Functional Exchange-Energy Approximation with Correct Asymptotic Behavior. *Physical Review A* **1988**, *38*, 3098-3100.
37. Lee, C.; Yang, W.; Parr, R. G. Development of the Colle-Salvetti Correlation-Energy Formula Into a Functional of the Electron Density. *Physical Review B* **1988**, *37*, 785-789.
38. Perdew, J. P., Density-Functional Approximation for the Correlation Energy of the Inhomogeneous Electron Gas. *Physical Review B* **1986**, *33*, 8822-8824.
39. Zhao, Y.; Truhlar, D. G. A New Local Density Functional for Main-Group Thermochemistry, Transition Metal Bonding, Thermochemical Kinetics, and Noncovalent Interactions. *The Journal of Chemical Physics* **2006**, *125*, 194101-1941018.
40. Adamo, C.; Barone, V. Toward Reliable Density Functional Methods Without Adjustable Parameters: The PBE0 Model. *The Journal of Chemical Physics* **1999**, *110*, 6158-6170.
41. Becke, A. D. Density-Functional Thermochemistry. III. The Role of Exact Exchange. *The Journal of Chemical Physics* **1993**, *98*, 5648-5652.
42. Stephens, P. J.; Devlin, F. J.; Chabalowski, C. F.; Frisch, M. J. Ab Initio Calculation of Vibrational Absorption and Circular Dichroism Spectra Using Density Functional Force Fields. *Journal of Physical Chemistry* **1994**, *98*, 11623-11627.
43. Zhao, Y.; Truhlar, D. G. The M06 Suite of Density Functionals for Main Group Thermochemistry, Thermochemical Kinetics, Noncovalent Interactions, Excited States, and Transition Elements: Two New Functionals and Systematic Testing of Four M06-Class Functionals and 12 Other Functionals. *Theoretical Chemistry Accounts* **2008**, *120*, 215-241.
44. Zhao, Y.; Truhlar, D. G. Comparative DFT Study of van der Waals Complexes: Rare-Gas Dimers, Alkaline-Earth Dimers, Zinc Dimer, and Zinc-Rare-Gas Dimers. *Journal of Physical Chemistry A* **2006**, *110*, 5121-5129.
45. Zhao, Y.; Truhlar, D. G. Density Functional for Spectroscopy: No Long-Range Self-Interaction Error, Good Performance for Rydberg and Charge-Transfer States, and Better Performance on Average than B3LYP for Ground States. *Journal of Physical Chemistry A* **2006**, *110*, 13126-13130.
46. Boese, A. D.; Martin, J. M. L. Development of Density Functionals for Thermochemical Kinetics. *The Journal of Chemical Physics* **2004**, *121*, 3405-3416.
47. Chai, J. D.; Head-Gordon, M., Systematic Optimization of Long-Range Corrected Hybrid Density Functionals. *The Journal of Chemical Physics* **2008**, *128*, 084106-084121.
48. van Leeuwen, R.; Baerends, E. J. Exchange-Correlation Potential with Correct Asymptotic Behavior. *Physical Review A* **1994**, *49*, 2421-2431.
49. Janak, J. F. Proof that $\partial E/\partial ni = \varepsilon$ in Density-Functional Theory. *Physical Review B* **1978**, *18*, 7165-7168.
50. Baer, R.; Neuhauser, D. Density Functional Theory with Correct Long-Range Asymptotic Behavior. *Physical Review Letters* **2005**, *94*, 043002-043006.
51. Yanai, T.; Tew, D. P.; Handy, N. C. A New Hybrid Exchange–Correlation Functional Using the Coulomb-Attenuating Method (CAM-B3LYP). *Chemical Physics Letters* **2004,** *393*, 51-57.
52. Heyd, J.; Scuseria, G. E. Assessment and Validation of a Screened Coulomb Hybrid Density Functional. *The Journal of Chemical Physics* **2004**, *120*, 7274-7280.

53. Heyd, J.;Scuseria, G. E. Efficient Hybrid Density Functional Calculations in Solids: Assessment of the Heyd--Scuseria--Ernzerhof Screened Coulomb Hybrid Functional. *The Journal of Chemical Physics* **2004**, *121*, 1187-1192.
54. Vydrov, O. A.; Heyd, J.; Krukau, A. V.; Scuseria, G. E. Importance of Short-Range Versus Long-Range Hartree-Fock Exchange for the Performance of Hybrid Density Functionals. *The Journal of Chemical Physics* **2006**, *125*, 074106-074109.
55. Vydrov, O. A.;Scuseria, G. E. Assessment of a Long-Range Corrected Hybrid Functional. *The Journal of Chemical Physics* **2006**, *125*, 234109-234118.
56. Vydrov, O. A.; Scuseria, G. E.; Perdew, J. P. Tests of Functionals for Systems with Fractional Electron Number. *The Journal of Chemical Physics* **2007**, *126*, 154109-154118.
57. Li, Y.; Coropceanu, V.; Bredas, J.L. Thermal Narrowing of the Electronic Bandwidths in Organic Molecular Semiconductors: Impact of the Crystal Thermal Expansion. *Journal of Physical Chemistry Letters* **2012**, *3*, 3325.
58. Hybertsen, M. S.; Louie, S. G. Electron Correlation in Semiconductors and Insulators: Band Gaps and Quasiparticle Energies. *Physical Review B* **1986**, *34*, 5390.
59. Hedin, L. New Method for Calculating the One-Particle Green's Function with Application to the Electron-Gas Problem. *Physical Review* **1965**, *139*, A796.
60. Sharifzadeh, S.; Biller, A.; Kronik, L.; Neaton, J. B. Quasiparticle and Optical Spectroscopy of Organic Semiconductors Pentacene and PTCDA from First Principles. *Physical Review B* **2012**, *85*, 125307.
61. Tiago, M. L.; Northrup, J. E.; Louie, S. G. Ab Initio Calculation of the Electronic and Optical Properties of Solid Pentacene. *Physical Review B* **2003**, 67, 115212.
62. Pauli, W. The Connection Between Spin and Statistics. *Physical Review* **1940**, 58, 716.
63. Pauli, W. Über den Zusammenhang des Abschlusses der Elektronengruppen im Atom mit der Komplexstruktur der Spektren. *Zeitschrift für Physik* **1925**, 31, 765.
64. Jeziorski, B.; Moszynski, R.; Szalewicz, K. Perturbation Theory Approach to Intermolecular Potential Energy Surfaces of van der Waals Complexes. *Chemical Reviews* **1994**, 94, 1887.

Chapter 7 Conclusions

7.1. Synopsis

First, we began with developing an understanding of the limitations in density functional theory (DFT, currently one of our main tools) and improvements that can be achieved through non-empirically tuning a given DFT method for the system of study. We investigated the torsion potentials, indicative of the length of wave function delocalization, in two prototypical π-conjugated polymers, polyacetylene and polydiacetylene, as a function of chain length using different flavors of DFT. Our study provided a quantitative analysis of the delocalization error in standard semilocal and hybrid density functionals and demonstrated how it can influence structural and thermodynamic properties. The delocalization error is quantified by evaluating the many-electron self-interaction error (MESIE) for fractional electron numbers, which allowed us to establish a direct connection between the MESIE and the error in the torsion barriers: a large torsion barrier was computed for methods with a large MESIE because of over-delocalization of the wave function. The use of non-empirically tuned long-range corrected hybrid functionals resulted in a very significant reduction of the MESIE and leads to an improved description for the magnitude of the torsion barrier. In addition, we demonstrated how our analysis allows for the determination of the effective conjugation length in polyacetylene and polydiacetylene chains.

With a demonstration of the effect that the self-interaction corrections employed through range-separated hybrid functionals can have in describing thermodynamic and electronic properties for

large, organic π-conjugated systems. We then investigated charge transport in single-molecule and finite molecular systems. In particular, we modeled the symmetry breaking and charge (de)localization in intramolecular charge-transfer complexes (organic mixed-valence systems) through nonempirically tuned range-separated DFT and compared the performance of this approach with higher-level approaches such as equation-of-motion coupled-cluster methods. Many computational studies have focused on describing the extent of electronic coupling between redox sites in mixed-valence systems. However, in general, the standard computational approaches suffer from intrinsic errors that lead to either an over-localized or an over-delocalized electronic structure, thereby preventing accurate depiction of the degree of charge (de)localization in the system. We found a robust approach based on a non-empirically tuned long-range corrected density functional methodology to characterize organic mixed-valence systems and demonstrated the performance of this approach via a study of representative Robin-Day class-II (localized) and class-III (delocalized) complexes. We then examined a borderline class-II/class-III system, which had proven difficult to describe accurately with standard DFT and HF methods. Our IP-tuned DFT approach proved capable of describing both charge localized and delocalized cases with computed values that compared well with both experiment and high-level *ab initio* methods. This was the first demonstration of a DFT method capable of describing both charge-localized and charge-delocalized mixed-valence systems because of the significantly reduced self-interaction error in this approach. This method opens up the possibility of future investigations to understand the extent of charge (de)localization in a given system, which has the implications for describing the distance that charges have to transfer between diabatic (charge localized) states. Typically, this value is estimated as the distance between redox

centers, which is known to be inaccurate. Therefore, a further understanding of this value can lead to improved description of intramolecular charge transfer processes.

With an understanding of single-molecule intramolecular charge-transfer systems, we were then able to examine intermolecular charge transfer; we examined the nature of electron delocalization and the associated electronic relaxation (polarization) energy in finite ordered (crystalline) and disordered (amorphous) molecular clusters of naphthalene, anthracene, tetracene, and pentacene ranging in size from n = 1 - 195. In order to quantify the polarization energy in finite clusters in the presence of an excess charge, we employed a combined multi-layer quantum-mechanical/embedded charge method to interpret experimental photoelectron spectroscopy spectra in order to elucidate the localized nature of a charge-carrier in prototypical organic semiconductors. Using the nonempirically-tuned DFT (IP-tuned DFT) approach, we computed vertical detachment energies that are in great quantitative agreement with experiment. The polarization energy for these clusters was found to evolve in a step-wise fashion with increasing systems size corresponding to the large inter-layer polarization present in oligoacene systems, which was the first time that such an important effect was detailed to the best of our knowledge.

We this understanding in hand, we then set out to understand the nature of charge (de)localization in these systems. In order to reliably characterize charge localization, a high-level complete-active space self-consistent field (CASSCF) method was used first and then compared to more computationally efficient density functional theory (DFT) methods. While

traditional DFT methods (such as B3LYP) did not recover the quantitative description of the charge localization found with CASSCF due to significant many-electron self-interaction error in the method, IP-tuned DFT was found to properly describe the charge delocalization when compared to CASSCF; these results show approximately 70% of an excess electron in these systems is localized, which is the first time that an estimate has been obtained with these reliable methods. The effect of this delocalized charge (as opposed to a charge localized entirely on a single molecule) on the polarization energy was computed to decrease significantly for the larger polaron. Therefore, this study represents a unique bottom-up approach to understanding charge (de)localization and the resulting polarization with increasing system size.

In addition to understanding the charge (de)localization in intermolecular and intramolecular charge-transfer systems with non-empirically tuned DFT, we also investigated DFT-calculated intermolecular electronic couplings (transfer integrals) in organic semiconductors to give insight into the impact that the choice of functional has on the value of this parameter, which is particularly important in the context of charge transport. We identified the major factor determining the magnitude of the calculated transfer integrals is the amount of nonlocal Hartree−Fock (HF) exchange within a given functional, with the transfer integrals increasing by up to a factor of 2 when going from 0 to 100% HF exchange for a series of conventional functionals. We detailed that the computed transfer integrals evolving linearly with the amount of HF exchange. We also used a long-range corrected functional to tune the contributions of (semi)local and nonlocal HF exchanges and highlight their respective roles as a function of intermolecular separation. This study was extended to understand the impact of the amount of HF exchange on the microscopic parameters (*i.e.*, band gaps, bandwidths, and effective masses)

describing charge transport in high-mobility organic crystals. We found that the band gap decreases and the effective masses increase linearly with an increase in the amount of HF exchange. Therefore choosing the "right" amount of HF exchange becomes an important consideration. To this end, we benchmarked the DFT results with those obtained with G_0W_0 as a way of benchmarking the optimal amount of HF exchange needed in a given functional to compute reliable hole (and electron) effective masses and bandgaps for periodic organic semiconductors. We then demonstrated that there is a direct link between intermolecular electronic coupling (required to be large for efficient charge-carrier transport) and the repulsive exchange-repulsion energy that hinders the formation of stacked conjugated materials.

In general, this thesis focused on achieving an electronic structure method capable of describing charge transport parameters in organic systems. DFT is typically chosen because it allows for a good compromise between computational efficiency and accuracy; however, standard DFT approaches fail in describing charge-transport parameters (*e.g.*, the delocalization of a charge in an ordered or disordered system) or can vary by nearly 100% in calculating important properties (*e.g.*, electronic coupling). Non-empirically tuning DFT reduced the error in standard DFT approaches that then allowed for the study of both localized and delocalized intramolecular/intermolecular charge-transfer systems; this resulted in a deeper understanding of the charge delocalization in mixed valence systems as a function of the inherent coupling between redox centers and an estimation of the amount charge delocalization in ordered oligoacene systems.